VAULT REFERENCE COPY

UCRL-52322

# THE ELECTRICAL CONDUCTIVITY OF IRON-SILICON ALLOYS AT HIGH PRESSURES AND THE EARTH'S CORE

George Matassov

(Ph.D. Thesis)

August 1977

Prepared for U.S. Energy Research & Development Administration under contract No. W-7405-Eng-48

LAWRENCE LIVERMORE LABORATORY
University of California/Livermore

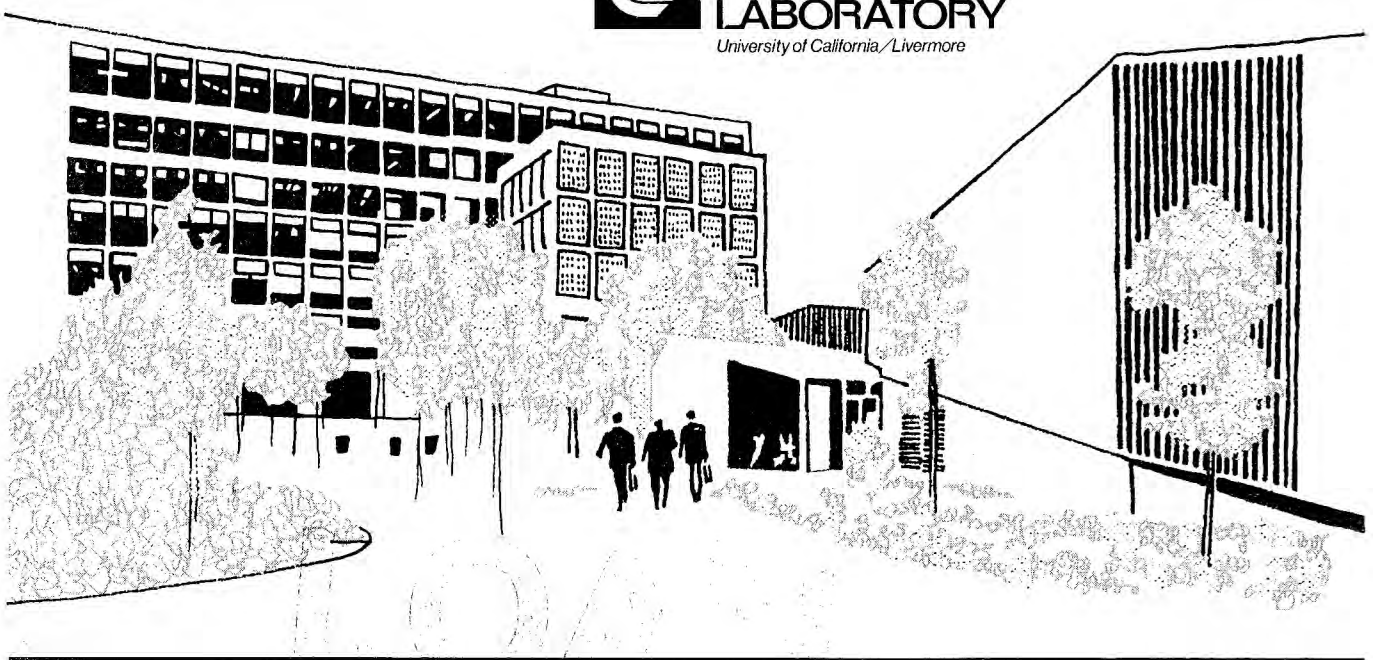

NOTICE

This report was prepared as an account of work sponsored by the United States Government. Neither the United States nor the United States Energy Research & Development Administration, nor any of their employees, nor any of their contractors, subcontractors, or their employees, makes any warranty, express or implied, or assumes any legal liability or responsibility for the accuracy, completeness or usefulness of any information, apparatus, product or process disclosed, or represents that its use would not infringe privately-owned rights.

NOTICE

Reference to a company or product name does not imply approval or recommendation of the product by the University of California or the U.S. Energy Research & Development Administration to the exclusion of others that may be suitable.

Printed in the United States of America
Available from
National Technical Information Service
U.S. Department of Commerce
5285 Port Royal Road
Springfield, VA 22161
Price: Printed Copy $ ; Microfiche $3.00

| Page Range | Domestic Price | Page Range | Domestic Price |
|---|---|---|---|
| 001–025 | $ 3.50 | 326–350 | 10.00 |
| 026–050 | 4.00 | 351–375 | 10.50 |
| 051–075 | 4.50 | 376–400 | 10.75 |
| 076–100 | 5.00 | 401–425 | 11.00 |
| 101–125 | 5.50 | 426–450 | 11.75 |
| 126–150 | 6.00 | 451–475 | 12.00 |
| 151–175 | 6.75 | 476–500 | 12.50 |
| 176–200 | 7.50 | 501–525 | 12.75 |
| 201–225 | 7.75 | 526–550 | 13.00 |
| 226–250 | 8.00 | 551–575 | 13.50 |
| 251–275 | 9.00 | 576–600 | 13.75 |
| 276–300 | 9.25 | 601–up | * |
| 301–325 | 9.75 | | |

*Add $2.50 for each additional 100 page increment from 601 to 1,000 pages; add $4.50 for each additional 100 page increment over 1,000 pages.

LAWRENCE LIVERMORE LABORATORY
University of California/Livermore, California/94550

UCRL-52322

# THE ELECTRICAL CONDUCTIVITY OF IRON-SILICON ALLOYS AT HIGH PRESSURES AND THE EARTH'S CORE

George Matassov

(Ph. D. Thesis)

August 1977

CONTENTS


| | | |
|---|---|---|
| | LIST OF FIGURES | iv |
| | LIST OF TABLES | vi |
| | ABSTRACT | viii |
| 1.0 | INTRODUCTION | 1 |
| 2.0 | GEOPHYSICS | 4 |
| 3.0 | SHOCK WAVE PHYSICS AND EQUATION OF STATE | 29 |
| 4.0 | IRON SILICON | 55 |
| 5.0 | ELECTRICAL CONDUCTIVITY | 78 |
| 6.0 | EXPERIMENT | 91 |
| 7.0 | EXPERIMENTAL RESULTS AND ANALYSIS | 111 |
| 8.0 | APPLICABILITY TO THE EARTH'S CORE | 139 |
| 9.0 | ACKNOWLEDGEMENTS | 149 |
| 10.0 | SUMMARY OF RESULTS | 150 |
| | APPENDIX A: SAMPLE CALCULATIONS AND ERROR ANALYSIS | 153 |
| | APPENDIX B: FeSi PHASE DIAGRAM | 160 |
| | APPENDIX C: DEMAGNETIZATION PULSE | 165 |
| | REFERENCES | 174 |

LIST OF FIGURES


| FIGURE | TITLE | |
|---|---|---|
| 2.1 | Formation of the Shadow Zone . . . . . | 7 |
| 2.2 | Characteristics of the Earth's Core . . . . | 14 |
| 2.3 | Wave Velocities vs Depth . . . . . | 16 |
| 3.1 | Shock Wave Through Medium . . . . . | 33 |
| 3.2 | Shock Wave, Isentropic and Isothermal Compression | 35 |
| 3.3 | Determination of P, $U_p$ from known Hugoniot . . | 38 |
| 3.4 | Hugoniot in P-V plane . . . . . | 38 |
| 3.5 | Possible Pressure Profiles Across Interface . | 40 |
| 3.6 | Impedance Matching Technique . . . . . | 42 |
| 3.7 | Pressure Profiles for Off-Hugoniot State . . | 45 |
| 3.8 | P vs $U_p$ for Off-Hugoniot State . . . . . | 46 |
| 3.9 | P vs V for Off-Hugoniot State . . . . . | 47 |
| 3.10 | First Order Phase Transition . . . . . | 54 |
| 4.1 | Iron Silicon Phase Diagram . . . . . | 57 |
| 4.2 | $X_{si}$ = 0.077 (Photomicrograph) 20 X . . . | 72 |
| 4.3 | $X_{si}$ = 0.181 (Photomicrograph) 20 X . . . | 72 |
| 4.4 | $X_{si}$ = 0.342 (Photomicrograph) 20 X . . . | 72 |
| 4.5 | $X_{si}$ = 0.342 (Photomicrograph) 200 X, Viewed with Polarized Light . . . . . | 72 |
| 4.6 | $X_{si}$ = 0.342 (Photomicrograph) 20 X, Showing Random Phases . . . . . | 73 |
| 4.7 | $X_{si}$ = 0.077 (Photomicrograph) 2000 X, Detail of Grain Boundaries . . . . . | 73 |
| 4.8 | $X_{si}$ = 0.25 (Photomircrograph), 128 X, Before Homogenization . . . . . | 73 |
| 4.9 | $X_{si}$=.25(Photomicrograph) 64X, after Homogenization | 73 |

| FIGURE | TITLE | |
|---|---|---|
| 4.10 | FeSi Density as a Function of Composition . . | 76 |
| 5.1 | Conductivity Sandwich (Isometric Drawing) . . | 88 |
| 5.2 | Partially Assembled Conductivity Sample . . | 89 |
| 6.1 | Plane Wave Lens . . . . . | 94 |
| 6.2 | Contact and Flying Plate Arrangement . . . | 94 |
| 6.3 | Layout of Sample Holder . . . . . | 97 |
| 6.4 | Sample Holder on Baseplate . . . . . | 98 |
| 6.5 | Partially Assembled Conductivity Experiment . . | 98 |
| 6.6 | Typical Pin Record . . . . . | 102 |
| 6.7 | Partially Assembled Pin Board . . . . | 102 |
| 6.8 | Distance vs Time for a Flying Plate Conductivity Experiment . . . . . | 104 |
| 6.9 | Constant Current Circuit . . . . . | 105 |
| 6.10 | Electrical Schematic of Current Pulser . . . | 106 |
| 6.11 | Leading Edge of Current Pulse, 0.5 microsec/cm . | 107 |
| 6.12 | Long RC Time of Current Pulse, 5 microsec/cm . | 107 |
| 6.13 | Top View of Current Pulser . . . . . | 107 |
| 6.14 | Conductivity Meausrement, 0.2 microsec/cm . . | 109 |
| 6.15 | Conductivity Measurement, 0.1 microsec/cm . . | 109 |
| 6.16 | Demagnetization Pulse, 0.1 microsec/cm . . . | 109 |
| 6.17 | Scope Calibration, Voltage and Time . . . | 109 |
| 6.18 | Typical Oscilloscope Arrangement . . . . | 110 |
| 7.1 | $U_s$ vs $U_p$, FeSi Hugoniot Data . . . . . | 113 |
| 7.2 | P vs V, FeSi Hugoniot Data . . . . . | 114 |
| 7.3 | $X_{si}$ = 0.25 Isentrope and the Earth's Core . . | 117 |

| FIGURE | TITLE | |
|---|---|---|
| 7.4 | Electrical Conductivity of FeSi as a Function of Pressure . . . . . | 126 |
| 7.5 | FeSi Resistivity vs Pressure . . . . . | 128 |
| 7.6 | Reduced Conductivity vs Pressure . . . . . | 129 |
| 7.7 | Reduced Conductivity vs Reduced Volume. . . | 130 |
| 7.8 | Electrical Conductivity Data of Geophysical Interest as a Function of Pressure . . . . . | 132 |
| 7.9 | Melting Point Extrapolations of Fe and Temperature Calculations Along the Fe Hugoniot . . . | 138 |
| B.1 | Phase Diagram for $X_{si} \leq 0.5$ . . . . . | 161 |
| C.1 | First and Second Order Solutions for the Demagnetization Pulse . . . . . | 173 |


LIST OF TABLES


| TABLE | TITLE | |
|---|---|---|
| 2.1 | Earth Model $B_2$, Inner Core Model CAL 1G . . | 15 |
| 4.1 | Electronic Specific Heat . . . . . | 62 |
| 4.2 | Physical Properties of FeSi Alloys . . . | 79 |
| 5.1 | Initial Conductivities at 20°C . . . . . | 90 |
| 5.2 | Initial State Parameters for Conductivity Measurements | 92 |
| 6.1 | High Explosive Shock Wave Generating Systems for Conductivity Experiments . . . . . | 95 |
| 6.2 | Hugoniot Standards for Conductivity Experiments . | 99 |
| 7.1 | Experimental Hugoniots for FeSi Alloys . . . | 115 |
| 7.2 | Least Squares fit to $U_s$, $U_p$ Data . . . . . | 118 |
| 7.3 | Cold Compression Curves (0° Isotherms) . . . | 119 |

| TABLE | TITLE | |
|---|---|---|
| 7.4 | Isentrope of $X_{si}$ = 0.25 for Outer Core . . | 120 |
| 7.5 | Demagnetization Decay Time . . . . | 123 |
| 7.6 | Hugoniot State of Impedance Standard, Conductivity Experiments . . . . . | 124 |
| 7.7 | Electrical Conductivity at High Pressures . . | 125 |
| 8.1 | Electrical and Thermal Conductivity of the Earth's Outer Core . . . . . | 140 |
| 8.2 | Thermal Conduction Gradients in the Core for K = 0.13 cal/sec deg cm . . . . . | 142 |
| 8.3 | Comparison of Adiabatic and Conduction Gradients | 147 |
| A.1 | Two Calculations for Off-Hugoniot Volume . . | 158 |
| B.1 | Crystalline Structure of FeSi Phases for $X_{si} \leq 0.5$ | 164 |

THE ELECTRICAL CONDUCTIVITY OF IRON-SILICON ALLOYS AT HIGH PRESSURES AND THE EARTH'S CORE


## ABSTRACT

The P-V-T behavior and electrical conductivity of Fe-Si alloys was investigated by shock wave techniques. The measured Hugoniot data in the pressure range of 100 to 1500 Kbars was used to calculate the equation of state of these alloys. Extrapolations of seismic velocity, density and pressure for $X_{si} = 0.25$ fall within the narrow range of acceptable values for the outer core.

The electrical conductivity of four Fe-Si alloys ($X_{si} = 0.077$, 0.181, 0.25 and 0.342) was measured in the pressure range of 500 to 1400 Kbars and the associated temperature range of 600°K to 2500°K. The electrical conductivities of the three highest Si concentrations showed only a small dependence upon the combined pressures and temperatures investigated.

Extrapolations of the electrical conductivity of $8.70 \times 10^3$ mho/cm at 1340 Kbars and 2518°K to liquid core temperatures (various estimates of the core temperature vary by 2500°K in the literature) fall well within the limits required by dynamo theories. The associated thermal conductivity of 0.13 cal/cm sec deg is in full agreement with the values used in the literature. It is concluded that the thermal conductivity is compatible only with dynamoes driven by precessional torques of the earth.

## 1.0 INTRODUCTION

Electrical conductivity of the Earth's core is one of the critical parameters in theories of the generation of the Earth's magnetic field and heat transfer from the outer core into the mantle. It has been frequently suggested that the outer core may be composed of an iron silicon mixture of about 15% to 20% silicon by weight (Knopoff and McDonald, 1960; Kormer and Funtikov, 1965; Ringwood, 1966; Balchan and Cowan, 1966; Birch, 1964 and 1972; Al'tshuler; 1965 and 1972, McQueen,et al, 1964). Pure iron or iron and nickel do not reproduce the density, bulk modulus and seismic velocity required of the outer core by geophysical observations (Al'tshuler, 1958, 1960, and 1965; McQueen and Marsh, 1966). The extraterrestrial measurements of the magnetic field of the Moon (Runcorn, 1972; Colman, 1972) and Mercury (Ness, et al, 1974 and 1975) have rekindled interest in theories of planetary dynamos.

Significant progress in geophysical observables in recent years has led to a refinement of proposed models of the interior of the earth (Bolt, 1972; Bullen, 1970 and 1972; Al'tshuler, 1972; Bullen and Haddon, 1973). The class of solutions that fit observables falls into a narrow range of densities, pressures and seismic velocities at the mantle-core interface and outer core (Press, 1970a, 1970b, and 1972). Only two high pressure experiments have been performed that indicate agreement between physical properties of materials and the recent models of the earth (Kormer and Funtikov, 1965; Balchan and Cowan, 1966). The electrical

conductivity of the Earth's core is still being estimated* on the basis of pure iron at low pressures (below 100 to 200 kbars) and/or extrapolated to 1,400 kilobars from alloy data taken at atmospheric pressure (1 bar) (Gardiner and Stacey, 1971; Johnston and Strens, 1973; Evans and Jain, 1972). Extrapolations of this kind must take into account the effects of pressure, composition and temperature. However the effects of composition and temperature have been shown to interact and cannot be treated as multiplication factors (Stacey, 1967; Gardiner and Stacey, 1971, retraction of Stacey 1967 article). This interaction has also been shown to violate Matthiessen's Rule, where the effects are summed linearly (Zinov'ev, et al, 1973). The situation gets untenable when the effects of pressure are included.

The present research was specifically designed to:

. Experimentally measure the Hugoniot of three Fe-Si alloy concentrations in the pressure range of 100 to 1500 kilobars, and to

. Experimentally measure the electrical conductivity of four Fe-Si alloy concentrations at the high temperature and pressure

---

*The only exceptions to this state of affairs are the measurements performed at Lawrence Livermore Laboratory of the electrical conductivity of iron at high pressures by Royce to 1,200 kbars (Royce, 1968), and Keeler and Mitchell to 1400 kbars (Keeler, et al, 1968 and 1969) by separate methods. The preliminary results of the present work on iron-silicon alloys were published in the Proc. 48th International School of Phys. "Enrico Fermi," Varenna, Italy, Academic Press, N.Y. 1971.

reached during the shock wave experiments at pressures between 500 and 1400 kbars.

The Hugoniot data allows the formulation of an Equation of State (EOS) based on the Grüneisen description of solids (Keeler, et al, 1971). The EOS is then used to calculate the off Hugoniot pressure and temperature of the shocked states reached during the measurement of the electrical conductivity in order to fully characterize the measurements. The conductivity measurements will hopefully reduce any required extrapolations to a reasonable interval in temperature only. Apparently the solid inner core is almost pure iron. When the melting point of iron on the Hugoniot is measured, it will enable us to pin the outer core/inner core interface temperature to about 200°C accuracy at a pressure of 3,200 kbars.

It is very difficult to specify the temperature in the Earth's core. Due to a lack of any observations at high pressures, the melting point of pure iron is the subject of heated debate in the literature and current estimates differ by a factor of two (McLachlan and Ehlers, 1971; Kraut and Kennedy, 1966; Higgins and Kennedy, 1971; Birch, 1972; Reynolds, et al, 1973; Leppaluoto, 1972; Gardiner and Stacey, 1971; Liu and Basset, 1975; Strong,et al, 1973; Verhoogen, 1973; Tolland, 1974; Alder, 1966). Carrying the argument one step further and applying it to the Earth's outer core, where the effects of alloying must be taken into account, is highly speculative at best. The results are very strongly dependent upon which theory one believes (and there is a large selection from which to choose).

The electrical conductivity measurements may nevertheless be compared with the calculated range of conductivities which are allowed by geophysical constraints. If the data satisfies this boundary condition, then iron-silicon should be considered as having passed another criteron as a possible core material. The electrical conductivity data may then be used in evaluating various geomagnetic dynamo theories and model dependent heat transfer by conduction out of the outer core.

This work deals with a number of scientific disciplines, each with a different set of accepted symbols and notations. An attempt has been made to keep the prevalent notation intact whenever possible. In those cases where the same symbol has been used for different variables, they are clearly identified. The notation within each section is consistent and the symbols are not duplicative.

## 2.0 GEOPHYSICS

A review of geophysical observables, models of internal structure and geomagnetism is required in order to establish the range of allowable bulk and electrical properties of the outer core.

### 2.1 GEOPHYSICAL OBSERVABLES

The structure of the earth's interior is inferred from seismological, astronomical and vibrational observations. All three techniques have dramatically increased their accuracies in the last two decades. Each technique shall be reviewed from the

point of view of how each has helped refine our understanding of the earth's core.

Some of the more popular methods of inferring the inner structure shall be reviewed in order to bring out the non-uniqueness of any one model of the earth. A summary of the mechanical properties of the earth, as inferred from these models, shall be presented.

### 2.1.1 Seismology

The basic technique of seismology is the measure of wave forms of acoustical waves at various stations generated by earthquakes and man-made explosions, the correlation of these wave forms to establish the time and location of each event, and the reconstruction of the mechanical properties of the medium through which the waves have propagated. Two kinds of waves are observed. Compressional (or longitudinal) waves are designated as P waves and shear (or transverse) waves are designated as S waves. The speed of the waves depends on the density and elastic properties of the material through which they propagate. Classically P and S refer to primary and secondary arrivals since S (shear) waves are slower than P waves. Generally, the time of arrival of a wave is plotted against a "distance". The distance between the seismic event and an observation station is expressed as an angle (designated $\Delta$ ) between radii drawn from the event and the station to the earth's center.

During the first half of this century seismologists meticulously compiled tables and curves of travel times of P and S waves versus angular distance. In 1909 Andrija Mohorovičic discovered the first

evidence of internal structure within the earth. He found a discontinuous slope for P waves on a time-distance plot of Balkan earthquakes. Mohorovičic explained the slope discontinuity by postulating an abrupt change in density below 50 kilometers. This discontinuity, which separates the earth's crust from the mantle, was found to be world wide and is now known as the Moho discontinuity. In 1913 Beno Gutenberg of the University of Göttingen numerically worked out an explanation of the observations that at angular distances from about 100° to 140° the amplitudes of P waves are greatly reduced. At angles above 140° the P waves appear again but they arrive about two minutes later than expected from extrapolation. He supposed that at a radius of about 3470 km the earth's structure changed. This discontinuity is now known to be the boundary between the mantle and the core. Figure 2.1 illustrates the formation of the shadow zone between 100° and 140°. For a least 2,000 km below the core boundary, no shear waves have been observed to propagate. For this reason (and others) the outer 2,000 km of the core is concluded to be molten or liquid. Further detailed analysis indicates the presence of an inner solid core (Bolt, 1972).

The distribution of P and S wave velocities may be derived within the earth from a set of travel time tables or time-angular distance curves. The propagation of these elastic waves is altered as follows. There are three types of changes of homogeneity of the propagating medium that are important in infering the earth's internal structure:

a. A continuous change of density and elastic constants with radius, due to temperature and pressure effects on chemically homogenous media.

b. A discontinuous change in density and elastical constants due to a boundary between distinct chemical or physical

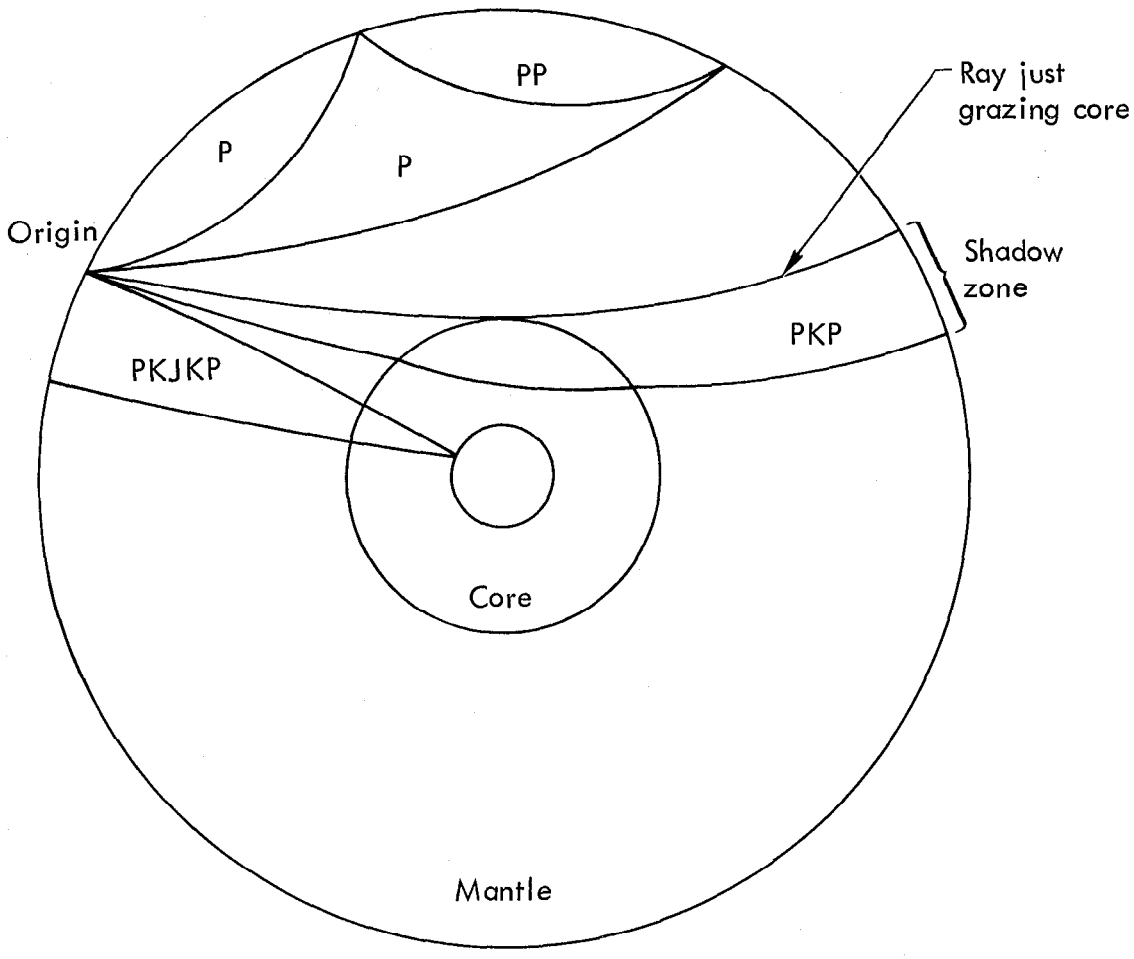


FIGURE 2.1 FORMATION OF THE SHADOW ZONE

media. The discontinuity is sharp with respect to the wavelengths of the seismic wave of interest.

c. A rapid change in density and elastic constants due to a chemical or a phase transition. The characteristic length is longer than the wavelength in question.

The three types of inhomogenisties cause refraction of both P and S waves. Discontinuous or sharp boundaries (as defined in b above) cause also reflections and partial conversion of P waves to S waves and vice versa. Fermat's principle of least time is used to construct seismic rays which show a minimum time between two points than any immediately neighboring paths. In general there may be several alternative rays, but each path requires a minimum of transit time relative to small deviations in the path. The following notation is used in describing some of the more common ray paths in the earth.

Designation P or S means a single path; designation PP or SS means a single reflection at the earth's surface. Various letters and numbers are inserted between the two or more P's or S's to denote the region through which the wave has passed. Waves that pass through the core are labeled K. This is a longitudinal or dilatational type of wave. Thus, P K K K K P or P4KP is a wave that has been reflected four times inside the earth's core before reaching the surface. The designation c denotes a reflection from the core-mantle interface. The derivation of the distribution of velocities is constantly refined when predicted times for various rays can be identified in seismograph records and used to improve the values of the velocities used in the predictions.

A painstaking analysis of the times of earthquake pulses was carried out by Sir Harold Jeffreys and K. E. Bullen resulting in a set of tables in 1940 which were the standard to which studies of earthquakes were referred. The most important source of uncertainties of these tables were the real variations of velocities within the earth and the error due to the spatial (three dimentional) location of the earthquake. The uncertainty due to the ignorance of the location of seismic activity of the source has been greatly reduced with the observation of seismic waves from large nuclear explosions. Not only geographical location but also the lack of depth (on a geophysical scale) has produced the present standard travel time tables (Herrin,1968). New observations since 1968 have significantly augmented them and added a lot of fine-structure.

Seismology took a major step forward in its observational accuracy as a consequence of the effort by several countries to discriminate between underground nuclear explosions and natural earthquakes. The U.S. has supported the establishment of over 100 standardized seismographic stations in many countries equipped with extremely sensitive seismographs. In addition, a number of seismographic arrays were constructed in such a way that random small quivers of the earth could be greatly reduced by noise suppression techniques. As an example, the Large Aperture Seismic Array (LASA) located near Billings, Mont. is comprised of 21 linked clusters with 25 seismometers in each cluster. The seismometers in each cluster are arranged in a hexagonal pattern with four along each radius at 60° intervals and one in the center. They

are radially linked together. The clusters are arranged in the corners of increasing squares with the largest square approximately 140 km on a side. In 1970, LASA announced that they have detected reflected signals from the boundary of the inner core of the earth (designated PKiKP). This was the first unequivocal evidence proving the prediction by Inge Lehman of Denmark in 1936 (Bolt, 1973) that the earth had an inner as well as an outer core. There were two direct conclusions. First, the inner core radius is 1,216 $\pm 2$ km. Second, the inner core had a sharp boundary. A significant result reached, based on a comparison of the relative strength of PcP signals from the outer core and PKiKP signals from inner core, was that the density at the top of the inner core cannot be greater than 14 gm/cc or lower than 13 gm/cc (Bolt,1972) (significantly reducing earlier and more uncertain estimates). The corresponding density of iron at 3.2 Mbar is 13 gm/cc (Altshuler, 1965). The fine structure of the velocity distribution within the thin layer D" is just above the outer core has been identified by the study of PcP waves that are diffracted by this layer into the shadow zone up to 118 degrees (Bolt,1972). The strength of the waves actually observed in the shadow is greater than that predicted by diffraction by a layer of constant velocity. The amplitudes and time of travel of these PcP waves indicate that the velocity within this thin layer of about 100 km is 13.29 $\pm 0.06$ km/sec (Adams,1972) and is less than the velocity within the mantle just above this layer (13.684 km/sec). Horizontally polarized S waves (SH) cannot diffract into the outer core as P waves (see Bullen, 1963 for the partition of energy at

a boundary for different polarizations and angles of incidence). Very large SH waves have been recorded up to 124 degrees (Hales & Roberts,1970). The independently calculated S wave velocity profile exhibits the same behavior as the P wave profile within the D" layer. The velocity distribution within the outermost 250 km of the outer core had been extrapolated until 1970. Observations of the difference in time of arrival of SKS and SKKS waves (Hales & Roberts,1971) has led to a lower velocity distribution near the core mantle boundary.

A controversy over the smoothness of the mantle-core boundary has not been fully resolved. The existence of topographical undulations has been suggested by R. Hide (1969) and others (with significant consequences upon the explanation for the variations of the earth's magnetic field). Undulations of less than 10 km cannot be resolved by the study of PcP waves. The nature of the core-mantle boundary is still being debated in the literature. Buchbinder (1972) has analysed the data collected by the Canadian Standard Seismograph Network for two large, deep focus earthquakes on July 31, 1970 and August 30, 1970. A systematic search has led to the identification of previously unobserved P7KP waves. They were recorded clearly at many stations. The important observation is that repeated reflections within the outer core by P7KP waves have a low standard deviation of the mean of 0.2 sec. This led to the conclusion that the velocity structure of the outer core appears to be laterally very homogeneous. Independently, Bolt (1973) identified K4KP and P7KP waves from the Novaya Zemlya

underground explosion of October 14, 1970. He found the onset of the waves quite abrupt, implying a sharp discontinuity of no more than 2 km. He concluded that the topographical bumps on the mantle-core boundary cannot be higher than 2 km because the travel times of the P7KP waves would show measurable variations. The analysis of frequency dependent reflection and transmission coefficients of various waves led Ibrahim (1973) to the conclusion that the outer core has finite rigidity (i.e., it is not a perfect fluid). He proposed that the mantle-core boundary is made up of four low-velocity, high-density layers between the two regions. The characteristics of his models indicate that the core-mantle boundary has an irregular surface. Buchbinder and Poupinet (1973) analyzed data from two large nuclear explosions, Novaya Zemlya on October 14, 1970 and Amchitka on November 6, 1971. The principal conclusion (in contradiction to Buchbinder's 1972 earlier findings) is that the core-mantle boundary is not well represented by a sharp boundary between a solid and a liquid. The data from a line of seismic stations in the Yukon suggests a transition zone and that the structure of the core-mantle boundary may not be radially symmetric. The consequences of the frequency dependence of the reflection and transmission coefficients of a layered core-mantle boundary would have serious effects upon the deduction of the structure below the outer core. Bullen and Haddon (1973) proposed a simple two layer core model with scattering at the core-mantle that satisfied all available data. This difference of opinion is not settled.

Two other features of the structure of the core need mention at this time. First, clear precursors to PKP waves have been observed since 1940. In 1962, Bolt (1973) suggested the existence of a transition shell, designated F, between the outer and inner core. The observance of numerous PKhKP waves have fully characterized the F layer. Second, Frances Birch has proposed that the inner core might be solid in 1940. The search for a hypothetical wave PKJKP, which is a shear wave in the inner core, has gone on since 1950 when K. E. Bullen predicted the travel time for this wave. The predicted travel time has been lengthened by several minutes by Bolt in 1964. In 1972, LASA has recorded PKJKP waves close to the arrival time predicted by the 1962 Bolt model. The evidence that the inner core is solid has finally been found.

Figure 2.2 illustrates the structure of the earth's core and Table 2.1 lists two sets of acceptable values of the P and S wave velocities at various depths and at the boundaries of the various regions. Figure 2.3 is a composite graph of the behavior of wave velocity as a function of depth.

Implicid in the above deductions of the behavior of the wave velocities is the use of models of the density and elastic properties of the earth. The construction of these models is discussed in another section.

### 2.1.2 The Earth's Moments of Inertia

The size, mass, moments of inertia and the gravitational potential of the earth have been refined from data taken from artificial satellites. The shape of the Earth is most precisely

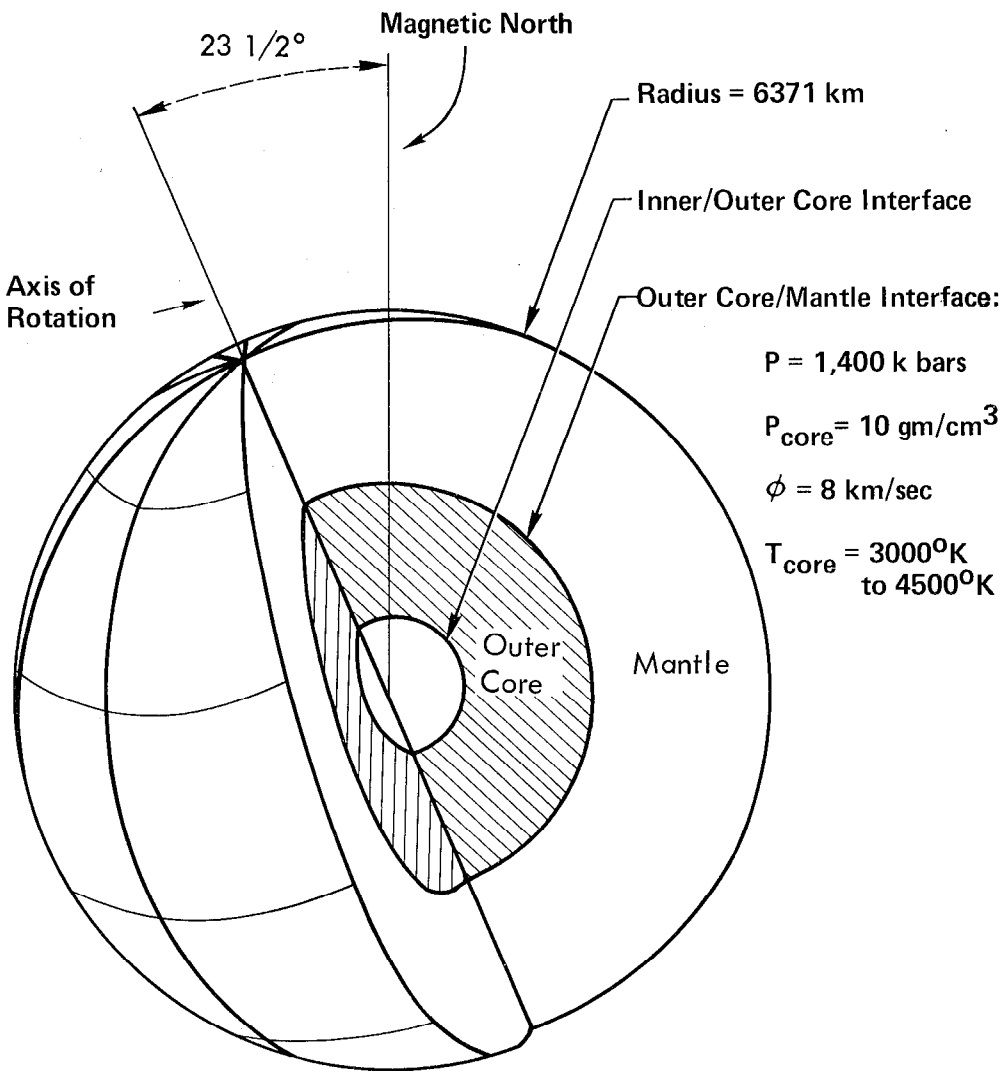


FIGURE 2.2 CHARACTERISTICS OF THE EARTH'S CORE

determined from the external gravitational potential as found from artificial satellites. The earth is very nearly a spherical ellipsoid of revolution and the gravitational potential around it

TABLE 2.1

EARTH MODEL $B_2$ (Bullen and Haddon, 1967)

| Interface | z km | P Kbars | $\rho$ g/cm$^3$ | g cm/sec$^2$ | $V_L$ km/sec | Vs km/sec |
|---|---|---|---|---|---|---|
| | 0 | 0 | 2.840 | 982.2 | 6.300 | 3.550 |
| Crust | 33 | 9 | 2.840 | 984.5 | 6.300 | 3.500 |
| Mantle | 33 | 9 | 3.320 | 984.5 | 7.750 | 4.353 |
| | 2878 | 1344 | 5.687 | 1075.8 | 13.640 | 7.304 |
| Outer Core | 2878 | 1344 | 9.891 | 1075.8 | 8.128 | 0 |
| | 5161 | 3328 | 12.699 | 433.5 | 10.338 | 0 |
| Inner Core | 5161 | 3228 | 12.699 | 433.5 | 11.258 | 3.860 |
| Center | 6371 | 3667 | 13.004 | 0 | 11.258 | 2.919 |

INNER CORE MODEL CAL IG (Bolt, 1972)

| | | | | | | |
|---|---|---|---|---|---|---|
| Outer Core | 5155 | ---- | 12.300 | ------ | 10.20 | 0 |
| Inner Core | 5155 | ---- | 12.70 | ------ | 10.80 | 2.85 |
| Center | 6371 | ---- | 13.00 | ------ | 11.35 | 3.10 |

is very nearly the same as that around a point mass. The general solution of Laplace's equation, $\nabla^2 V = 0$ for the gravitational potential V, may be written, as a series expansion of spherical Bessel function. Of all of the coefficients in the infinite

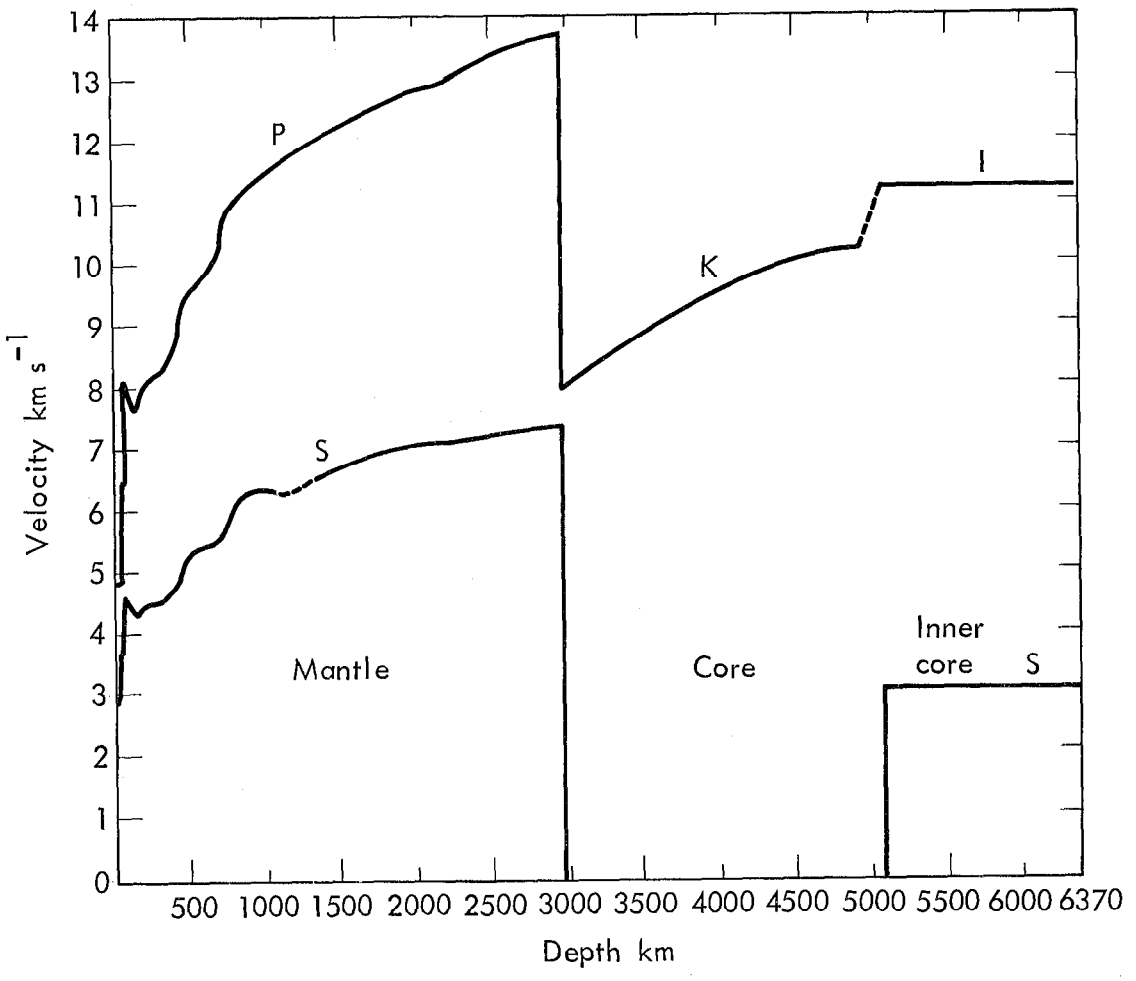


FIGURE 2.3 WAVE VELOCITIES VS DEPTH

series, $J_2$ is the most important for two reasons. It is on the order of $10^{-3}$, with all the others being on the order of $10^{-6}$ or less. $J_2$ is also closely related to the polar flattening and angular velocity of the earth. Since the earth is almost symmetical about the polar axis of rotation, all moments of inertia, A, about axes in the equatorial plane can be assumed to be equal with great precision. The moment of inertia, C, about the polar axis is unique. It can be shown (Cook 1973, Appendix 3) by McCullagh's theorem that $J_2 = (C-A)/Ma^2$ where M is the mass of the earth and a is the equatorial radius. From satellite data, the International Astronomical Union has adopted

$$a = 63.78.160 \text{ km}$$

$$GM = 3.986 \times 10^{14} m^3/s^2$$

$$J_2 = 1.0827 \times 10^{-3}$$

Where G is the universal gravitational constant. The precession of the equinoxes (lunisolar precession) is proportional to the dynamic ellipticity of the earth, defined as H, where $H = (C-A)/C$.

The precession of the equinoxes is due to the gravitational attraction of the sun and moon upon the equatorial bulge which tends to twist the buldge into the planes of the moon and ecliptic orbits. Since the Earth is rotating, the effect of this torque is to cause precession of the axis of rotation. The astronomical measurements of H give a numerical valve of $H = 3.2756 \times 10^{-3}$. Forming the ratio $J_2/H$ leads directly to $J_2/H = C/Ma^2 = 0.3306$ (and therefore $A/Ma^2 = 0.3295$). This is a very important result in the study of the internal structure of the earth. Without observing the precession of the nodes of

artificial satellites, $J_2$ is unknown and the precession of the equinoxes (H) cannot give the separate moments of inertia C and A of the earth. Prior to satellite data, a value of 0.3335 was commonly used for the ratio $C/Ma^2$. A. H. Cook (1963) revised the ratio to 0.3309 in 1963. Since then, a slight change has been made based upon more accurate data to a value of 0.3306. This has changed one of the most basic boundary conditions for any model of the inner structure because the ratio $C/Ma^2$ shows how strongly the mass is concentrated toward the center of the earth. The effect has been to transfer some mass from the mantle to the core (Bullen 1968).

### 2.1.3 Free Oscillations of the Earth

Whenever the earth is given an impulse by a large earthquake, it vibrates for a long time. The idea that the earth could undergo free vibrations extends to the pioneer work of over 100 years ago done on the theory of elasticity by Lord Kelvin, M. Lamb, A. E. M. Love and Lord Rayleigh. Interest in the subject was renewed in the 1950's. From 1950 to 1970, there have been nine earthquakes with Richter magnitude equal to or greater than 7.75. Up until Oct 1969, instruments were not sufficiently sensitive to observe the low frequency elastic gravitational normal modes for earthquakes below 7.75 on the Richter scale. A very large earthquake in Chile in 1960 produced records on strain gagues and gravity meters that gave the first reliable value of a number of free periods of the earth. The normal modes are highly resonant. Typically values of Q are 100 to 400. The lowest

observed frequencies belong to a quinted of modes with a Q of 350, whose period is 53.6 minutes. The fundamental radial mode has a period of 20.46 minutes and by far the largest Q of about 6000. The amplitude of this mode decays by a factor of ten in two months (Gilbert, 1971). Shear is believed to be the dissipation mechanism. The equations of motions cannot be solved analytically for the eigenfrequencies because the properties of the earth vary with depth. The eigenfrequencies are found with the aid of high speed digital computers. The procedure used is reviewed in the following section. Two types of oscillations are possible. Radial oscillations, called spheroidal, involve motion where every point on a radius moves in or out along the radius. They involve changes in density and variations of gravity at the surface. The other modes, called toroidal, involve parts of the earth twisting relative to each other. They show up as changes of horizontal displacement at the surface with no variations of gravity. The modes of oscillation have a fine structure due to the splitting of the modes caused by the rotation of the earth. Two checks are made to correctly identify that the observed motions are due to free oscillations. Gravity meter records do not show periods of toroidal oscillations; strain gauges show periods of both types. Secondly, the splitting of the modes due to the earth's rotation can now be resolved. Since each mode has it's own pattern of nodal surfaces, different stations will record various amplitudes for the same mode. In Oct 1969, the first of a new type of

accelerometer was introduced. This allowed the observation of low frequency modes due to earthquakes equal to 6.5 on the Richter scale (Gilbert, 1971). The significance of lowering the threshold from 7.75 to 6.5 becomes clear when, on the average, there are about 20 earthquakes of magnitude 6.5 or above a year. Theoretically, twice the data could be collected in one twentieth the time. The new body of information has not only supplemented the data of travel times, but also helped resolve difficulties in calculating the density distribution in two inhomogeneous transition zones of the upper mantle.

## 2.2 MODELS OF INTERNAL STRUCTURE

A major goal of geophysics is the derivation of the equation of state (that is the dependence of density upon pressure and temperature) for the materials in the different regions of the earth. The most accurate derivations, based upon the geophysical observables, are for the variation of velocities and elastic properties of the earth with radius. The variation of density with radius is not as accurately determined as the velocities. The calculation of pressure as a function of radius is relatively insensitive to the assumed density distribution (except near the earth's surface, where the effect of strength of materials becomes important). A number of methods of calculating the velocities, elastic properties, density and pressure as a function of radius are reviewed. The important assumptions of each method are outlined. Representative result were presented in Table 2.1. The non-uniqueness of these distributions (Gilbert and Backus, 1968;

Dziewonski, 1970) is due to the imprecise and incomplete data, and the limitations of each theoretical model and its computational methods. In spite of the non-uniqueness, possible solutions are constrained within certain limits which are surprisingly narrow in certain regions.

The uncertainties of the temperature distribution are reviewed. The equation of state (EOS) is not complete without the knowledge of this distribution. A comparison of the derived properties of the internal structure with the properties of FeSi alloys as found in the laboratory is made in Section 7 for the earth's core.

### 2.2.1 Bulk Properties of Materials

Seismic P and S waves are very low frequency sound waves and their velocities $V_\ell$ and $V_s$ are given in terms of the ratio of their respective elastic moduli and the density $\rho$ :

$$V_\ell = \sqrt{\Lambda / \rho} \tag{2.1}$$

$$V_s = \sqrt{\mu / \rho} \tag{2.2}$$

where $\mu$ is the rigidity. $\Lambda$ is related to Young's modulus $\beta$ and Poisson's ratio $\nu$ by the following equation (Joos, 1934, gives the full derivation starting from the standard stress-strain relationship for deformation of a constrained medium):

$$\Lambda = \frac{\beta\,[1-\nu]}{[1-2\nu][1+\nu]} \tag{2.3}$$

The bulk modulus $\kappa$ and the rigidity $\mu$ are also related to Young's modulus and Poisson's ratio:

$$\kappa = \frac{\beta}{3\left[1 - 2\nu\right]} \tag{2.4}$$

$$\mu = \frac{\beta}{2\left[1 + \nu\right]} \tag{2.5}$$

or $$\Lambda = \kappa + \frac{4}{3}\mu \tag{2.6}$$

The P and S wave velocities are now written in their usual form:

$$V_\ell = \sqrt{\frac{\kappa + 4/3\,\mu}{\rho}} \tag{2.7}$$

$$V_s = \sqrt{\mu/\rho} \tag{2.8}$$

Bullen (1963) has rigorously applied the theory of elasticity in the derviation of eqs 2.7 and 2.8. Another useful quantity called the seimic parameter, $\phi$ , is given by

$$\phi = \frac{\partial \mathbf{P}}{\partial \rho} \equiv \frac{\kappa}{\rho} = V_\ell^2 - \frac{4}{3} V_s^2 \tag{2.9}$$

where **P** is the pressure.

The early work on deriving the density and pressure was based upon a few simple assumptions. For a chemically homogeneous layer (no changes of phase or composition), the density varies only with pressure. The temperature gradient within the earth must be adiabatic; i.e., thermal expansion was neglected. This method was developed by L. M. Adams and E. D. Williamson in 1923. For a spherically symmetric earth, a hydrostatic condition was assumed. This is reasonable because the strength of rock materials is

negligible compared to the pressures in all but the top few kilometers. Therefore shearing stresses are ignored. For a hydrostatic state,

$$d\mathbf{P} = -g(r)\,\rho\,dr \tag{2.10}$$

where $g(r)$ is the value of gravitational acceleration at radius $r$, given as

$$g(r) = \frac{G\,m(r)}{r^2} \tag{2.11}$$

where

$$m(r) = \int_0^r 4\pi r^2 \rho(r)\,dr \tag{2.12}$$

is the mass contained within radius $r$. The negative sign in eq 2.10 is due to the radius being measured outward. The density as a function of radius is given by

$$\frac{d\rho}{dr} = \frac{d\rho}{d\mathbf{P}}\frac{d\mathbf{P}}{dr} = \frac{\rho}{\kappa}(-g(r)\,\rho) = -\frac{g(r)\,\rho}{\phi} \tag{2.13}$$

This is the Adams-Williamson equation. Alternatively, it can be rewritten as

$$\frac{d\rho}{dr} = -\frac{G\,\rho\,m(r)}{r^2(V_\ell^2 - \frac{4}{3}V_s^2)} \tag{2.14}$$

Equations 2.14 and 2.10 may be used to calculate $\rho$ and $\mathbf{P}$ starting from the surface and working inwards, in small increments of depth. Since $V_s$ and $V_\ell$ are known, the elastic properties of

the material $\kappa$ and $\mu$ may also be calculated as a function of depth.

The division of the earth into distinguishable regions with a variety of changes of homogemity is apparent from the velocity data. It is clear that the Adams-Williamson equation cannot be applied throughout the interior of the earth. Therefore, it is interesting to estimate the dependence of bulk properties of materials on pressure as it is increased (in terms of observed or calculated behavior of known materials and set the stage for the next two sections). At atmospheric pressure (1 atm = 1.013 bar and 1 bar = $10^6$ dynes/cm$^2$), the properties of solids are determined primarily by the forces between ions or atoms making up the crystal lattices. These forces determine the type of lattice and hence the density and elastic properties. Lattice energies are on the order of 1 eV and are large when compared to $\mathbf{P}\,\mathrm{V}$, where $\mathrm{V}$ is the atomic or molecular volume. For a presumed representative upper mantle mineral, olivine $(MgFe)_2 SiO_4$, the molecular mass is 140 and the molecular volume is $6.6 \times 10^{-22}$ cm$^3$. The product $\mathbf{P}\,\mathrm{V}$ is $6.6 \times 10^{-14}$ dyne cm or approximately $4 \times 10^{-4}$ eV. At pressures of 10 kilobars and above, the strain energy is greater than 1 eV (justifying the hydrostatic assumption made above) and the structure of the crystal lattice will not affect the bulk properties. The details of the atomic structure are important up to about 500 kilobars because the atomic energies are on the order of 10 to 50 eV. Between 500 kilobars and a few megabars it is the total number of electrons per atom

(the mean atomic number or atomic volume) that predominantly affect the bulk properties. The compression curves are determined by the structures of the electron shells of elements and compounds. The physical properties depend upon the character and specific features of the interatomic bonds. Great difficulties in theoretical analysis have prevented the derivation of reasonable models to explain the observables. Only at pressures above several hundred megabars, where the outer electron shells collapse, have statistical representations (such as the Thomas-Fermi-Dirac quantum statistical theory) met with success.

Thus, at pressures in the deep mantle and the core, only empirical data and the properties of materials experimentally investigated can be used at present. As pointed out earlier, the internal structure shows zones with abrupt physical changes. They must be explained in terms of pressure, phase, composition and temperature.

## 2.3 GEOMAGNETISM

The direct observables of the geomagnetic field are nowhere near as precise as the direct observables used in describing the bulk properties of the inner structure of the Earth. From the study of magnetism of certain rocks acquired at their formation (called paleomagnetism), it has been shown that the Earth possessed a magnetic field for most of its 4.5 billion years, or at least as far back in time that rock can be found. A further study of these rocks revealed that the geomagnetic field reverses it polarity within $10^3$ years at random time intervals on the

order of $10^6$ years. These field reversals are reviewed in detail by Bullard (1968).

Based on estimates of the conductivity of the Earth's outer core, a resistive decay time of $10^4$ years is calculated. That is, if the mechanism responsible for the generation of the Earth's magnetic field were to be "turned off," then it would take at least $10^4$ years for the observed field to collapse. Time variations of the magnetic field have been observed only with periods longer than three years. The non-dipole portion of the geomagnetic field has been observed to drift westward at the rate of $0.18°/yr$. The most prominent non-dipole feature, known as the westward drift, has been reviewed by Roberts and Soward (1972).

Thus, any theory of the geomagnetic field must explain both the maintenance of the field over times long compared with $10^4$ years and the field reversals which occur over times shorter than the $10^4$ year resistive decay time. Many types of dynamo theories have been proposed to explain these observations. They share the commonly deduced properties of the core including that the outer core is fluid and has a metal-like conductivity. Recent observations of residual magnetism of lunar rock and a magnetic field around Mercury pose an interesting question. Is one mechanism flexible enough to explain the extra-terrestial magnetic fields as well or is more than one mechanism necessary to explain the observations? Perhaps the structures are so different that more than one mechanism is necessary.

Magnetohydrodynamic theories have constructed many classes of motion, including small scale and turbulent velocity fields, which are capable of dynamo action (Bullard, 1972; Roberts, 1971; Malkus, 1971). Of greater interest here are the most plausible energy sources that may be responsible for driving a dynamo in the outer core. This subject is addressed in Section 8.

The most extensively studied dynamo motions are caused by thermal convection on a global scale both for turbulent and non-turbulent flows. Radioactive heating (originally suggested by Bullard in 1950) has been recently reproposed as the most likely heat source for this mechanism (Lewis, 1971; Murthy and Hall, 1970 and 1972). The important condition that must be satisfied is that the temperature gradient must be at least adiabatic. The release of latent heat due to crystallization at the inner core boundary has been considered as another source for the thermal convection (Verhoogen, 1961). Malkus (1968) has proposed that precessional torques between the mantle and the core can drive either turbulent motions or laminar flow. The thermodynamic consequences of these three energy sources are discussed in Section 8.

Another fruitful consideration is the estimation of the allowable limits of the electrical conductivity of the core. The lower limit of electrical conductivity is frequently estimated (roughly) by considering a dimensionless quantity known as the magnetic Reynolds number, $Rm$ , (Jackson, 1965) given by

$$Rm = \frac{v \ \tau}{\ell} \tag{2.15}$$

where v is a characteristic velocity of the medium, $\ell$ is the scale size and $\tau$ is the diffusion time in which an initial magnetic field will decay (if the fluid were to be stopped suddently). The diffusion time is given as

$$\tau = \mu_0 \sigma \ell^2 \tag{2.16}$$

where $\sigma$ is the electrical conductivity and $\mu_0$ is the permeability of the non-magnetic medium. Magnetohydrodynamics requires the electrical resistivity to be sufficiently high to ensure that the transport of the lines of force dominates over the diffussion of the field lines. For the dynamo action to be self sustaining, Rm must be on the order of 10 to 100. As Rm approaches infinity, the magnetic flux is trapped inside the core and cannot get out. If a characteristic velocity is chosen to be twice the mean rate of the westward drift at core depth, $v \approx 3 \times 10^{-6}$cm/sec and the scale size is taken as the outer core depth, $\ell \approx 2 \times 10^8$ cm, then

$$\sigma > 10^2 \text{ to } 10^3 \text{ mho/cm}$$

The upper limit is set by the condition that the heat flux conducted out of the outer core cannot exceed 3 to 4 X $10^{19}$ erg/sec (Stacey, 1972; Murthy and Hall, 1972; Frazer, 1973). This corresponds to about 8 to 12% of the total observed geothermal flux. The associated electrical conductivity must be $\sigma < 10^4$mho/cm

(discussed in Section 8). Various calculations of the generation of heat in the mantle and transfer of heat out of the mantle conclude that not more than 8 to 12% of the total geothermal flux can be generated in the Earth's core (Wang, 1972; Tozer, 1967 and 1972; Clark, 1971; Cook, 1973).

It is hoped that the study of bulk and electrical properties of FeSi alloys at high temperatures and pressures achieved behind shock fronts may narrow the gap between the geophysical observables and the theories proposed to explain them.

## 3.0 SHOCK WAVE PHYSICS AND EQUATION OF STATE

The properties of the inner structure of the earth (i.e., shear and longitudinal velocities, density, pressure and temperature) can be compared to the properties of materials as found in the laboratory in order to more fully interpret the geophysical observables. This is not easily done because the temperatures and pressures that can be usually achieved in the laboratory are substantially less than those associated with the deep interior of the earth. Only dynamic shock wave experiments have been able to significantly narrow this gap.

### 3.1 VALIDITY OF DYNAMIC TECHNIQUES

In the last few years, sufficient data has been obtained by three completely independent experimental techniques in order to compare them for consistency. Acoustical velocity data at low pressures, static compression data at pressures up to 300 bars and shock wave data from 50 Kbars to above 1 Megabar (and extrapolated

down to 1 atmopshere) were compared (S. N. Vaidya and G. C. Kennedy, 1970; R. Grover, 1970). All three types of data are consistent up to 45 Kbars (the limit of acoustical experiments) and static compression and shock velocity data agree to the limit of static experiments. In almost all cases, the agreement is better than 2 percent. An X-ray photograph technique under static pressure developed by Jamieson and Lawson (1962) was used to unambiguously identify many crystal structures (phases) including iron at high pressures. These specific phase transitions have been identified as discontinuities in the slope in the Us vs Up plots of shock wave data (discussed in the next section). Dynamic methods have gained full acceptance in gathering semiempirical equation of state descriptions of solids at high pressures.

Numerous experimental investigations have shown (for example, J. M. Walsh and R. M. Christian, 1955; L. V. Al'tshuler, 1965; M. I. Rice, R. G. McQueen, and J. M. Walsh, 1958) that the width of the shock front is less than 0.1 mm over a wide range of pressures. This means that the pressure gradient between the unshocked and shocked material is almost discontinuious and the shocked state is reached in 20 to 10 nanoseconds (fluid viscosity, radiation and heat conductivity tend to limit the steepness of the gradient). A well designed experiment will maintain the shocked state for times as large as $0.5 \times 10^{-6}$ sec before other events interfere with it. This means that the shocked state can be described by an equation of state that satisfies the usual thermodynamic relations.

The first successful X-ray diffraction experiment of a shock-wave compressed solid was performed in 1970 (Q. Johnson, et al, 1970). Lattice spacing measurements of LiF before and after a 130 Kbar shock clearly showed:

a. A diffraction pattern behind the shock front. This implied that crystalline order can exist and that the ordering takes place in a time that is shorter than 20 nanoseconds.

b. The location of the (200) X-ray reflection implied that the unit cell dimension changed isotropically. This means that, at least for the material studied, shock compression is essentially hydrostatic.

The seemingly contradictory change in dimensions (microscopic change is three dimensional while the macroscopic change is one dimensional) is phenomenologically explainable by the small movement of nearest neighbor atoms. The preferred arrangement of a lattice with smaller dimensions occurs with little movement of the atoms in a plane perpendicular to the shock wave while the sample undergoes a large compression in the direction of the shock wave.

## 3.2 SHOCK WAVES AT HIGH PRESSURES

A shock wave* results from the property that the transmission of a compressional disturbance (which exceeds some minimum amplitude) proceeds at a velocity greater than the speed of elastic

---

*For a rigorous discussion of shock wave physics see Courant, et al, 1947; McQueen, 1973; Al'tshuler, 1965; Huang, 1966; Keeler, et al, 1971.

waves and reinforces itself. This is due to two effects. The material behind the shock front is compressed, increasing the sound velocity, and the material itself is given a forward velocity which is added to the velocity of sound of the uncompressed material. This occurs for most materials in compression where the compressibility decreases with increasing pressure.

Three basic assumptions are used to construct the one dimensional shock wave theory:

a. Equilibrium (steady state) conditions exist ahead of and behind a plane wave shock front (one dimensional shock).

b. The shock front thickness is so small that it can be treated as a discontinuity.

c. The shock pressure exceeds the shear strength of the material. Therefore the material can be treated as a fluid and the pressure in the compressed state is hydrostatic.

These three assumptions are very well supported by plane wave experimental data.

The conservation of mass, momentum and energy across the shock front lead to the so-called Rankine-Hugoniot relationships. Let the undisturbed state be described by pressure $P_o$, density $\rho_o (= 1/V_o)$, internal energy $E_o$ and particle velocity $U_{po}$ (assumed to be at rest, i.e., $U_{po} = 0$). The shocked state is described by the same variables with the subscript 1 (and let $U_{p1} = U_p$). Let the shock front travel with a velocity $U_s$ (See Fig 3.1). After some time $dt$, the shock front has moved a distance $D = U_s dt$ while the shocked material (defined at time $t = 0$)

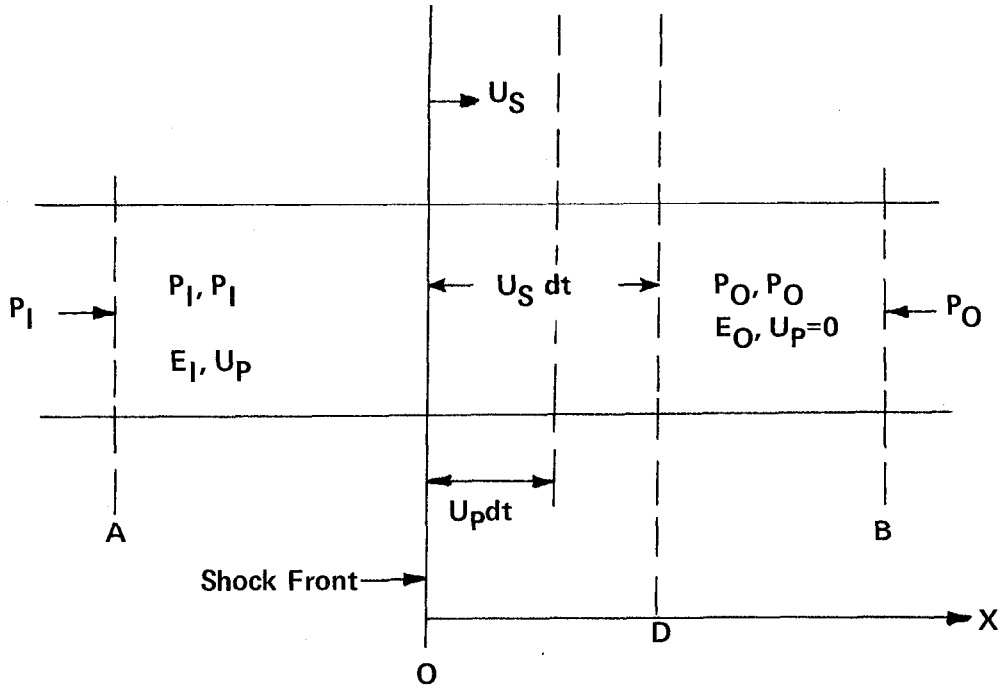


FIGURE 3.1 SHOCK WAVE THROUGH MEDIUM

will have moved $U_p dt$ . The material $\rho_o U_s dt$ has been compressed into $\rho_1 ( U_s - U_p )dt$ . Conservation of mass gives

$$\rho_o U_s = \rho_1 ( U_s - U_p ) \tag{3.1}$$

This is another way of saying that the mass flux in and mass flux out of the shock front are equal.

The net force on a unit cross section of the material between A and B is $P_1 - P_o$ . The time rate of change of momentum is the mass flux ( $\rho_o U_s$ ) multiplied by the velocity change ( $U_p$ ). This is Newton's second law. It gives

$$P_1 - P_o = \rho_o U_s U_p \tag{3.2}$$

The net work done by the shock on the mass is equal to the change in its kinetic and internal energies. The net work done on the mass $\rho_o U_s dt$ in time $dt$ is equal to the net work done by the pressure difference per unit area, $P_1 U_p dt$. The change in kinetic energy is $\rho_o U_p^2 U_s dt/2$ and the change in internal energy of the mass is $(E_1 - E_o) \rho_o U_s dt$. One gets

$$\rho_1 U_p = \rho_o U_s U_p^2 / 2 + \rho_o U_s (E_1 - E_o) \tag{3.3}$$

Solving for $U_s$ and $U_p$ gives

$$U_s = V_o \sqrt{\frac{(P_1 - P_o)}{V_o - V_1}} \tag{3.4}$$

and

$$U_p = \sqrt{(P_1 - P_o)(V_o - V_1)} \tag{3.5}$$

Substituting eq. (3.4) and (3.5) into (3.3) gives

$$(E_1 - E_o) = (P_1 + P_o)(V_o - V_1)/2 = \Delta E \tag{3.6}$$

which is the area under the straight line AB in Figure 3.2. For shock experiments, $P \gg P_o$ (where $P_o$ = 1 bar) and $P_o$ can be set equal to zero for simplicity. Equation 3.1 can also be rewritten as

$$V_1 = V_o(1 - U_p/U_s) \tag{3.7}$$

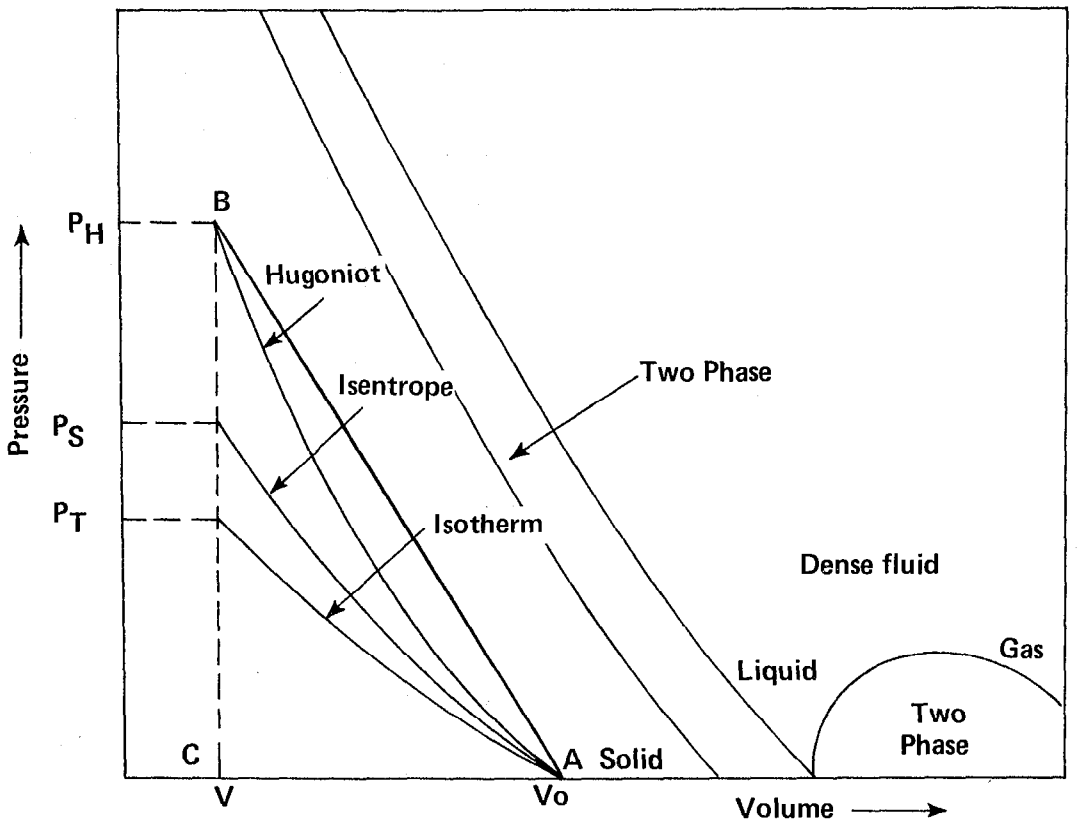


FIGURE 3.2 SHOCK WAVE, ISENTROPIC AND ISOTHERMAL COMPRESSION

The three conservation equations (3.1), (3.2), and (3.6) contain five variables and therefore only two are independent. The most easily measured variables are $U_s$ and $U_p$ and shock wave experiments are designed to measure them. Normally $U_p$ is found indirectly by measuring the free surface velocity $U_{fs}$ or by impedance matching (to be discussed in the next section). Many shock wave experimental techniques are described in a review by Keeler, et al (1971).

The dependence of the specific internal energy of a material upon pressure and volume defines the equation of state (EOS), $E = E(P,V)$

of the material. If the EOS is known, eq (3.6) and the EOS are used to remove the energy dependence. The resulting equation defines the locus of all possible final states, $P_1$ , $V_1$ reachable by shocking the material in its initial state $P_o, V_o$ . The defined curve is called the Hugoniot and is shown in Fig 3.4. Each point on the Hugoniot is defined by the intersection of a straight line, $U_s$ = constant, and a hyderbola, $U_p$ = constant. The straight line connecting the initial and final states is called the Rayleigh line with a slope given by $- U_s^2 \rho_o^2$ . Even when the EOS is not known, the Hugoniot can still be experimentally established. Then semi-empirical EOS's can be constructed from the data. For most materials, the shock wave velocity increases with shock pressure. Differentiating eq (3.4) gives $\frac{dP}{dV} < 0$ and $\frac{d^2P}{dV^2} > 0$ for Hugoniot curves for these materials. Two exceptions to this rule are elastic-platics wave structures due to finite material rigidity (at relatively low pressures) and two wave structures connected with first order polymorphic phase changes.

It can be shown that when the Hugoniot is concave upward (as in Fig 3.2), the entropy change is positive. This is not surprising because the work done by the shock is irreversible and results in an entropy and temperature increase in the shocked material. The energy going into these two increases cannot be partitioned without a full EOS of the material. In practice, a number of semi-empirical EOS's are used with varying degrees of validity. For a typical material shown in Fig 3.2 (where polymorphic

transitions in the solid phase are ignored), three other curves are of interest. The energy required to compress the material from $V_o$ to $V_1$, while holding the entropy or the temperature constant, is given by

Isentrope: (area under curve AD) $\Delta E_s = -\int_{V_o}^{V} P\, dV_s$ , (3.8)

$dS = 0$

Isotherm: $\Delta E_T = \int_{S_o}^{S} T\, dS_T - \int_{V_o}^{V} P\, dV_T$ , $dT = 0$ (3.9a)

$$= \int_{V_o}^{V} T\, (\partial P/\partial T)_V dV_T - \int_{V_o}^{V} P\, dV_T \qquad (3.9b)$$

$0^oK$ Isotherm (cold compression curve):

$$\Delta E_c = -\int_{V_o}^{V} P\, dV , \qquad T = 0^o K \qquad (3.9c)$$

For both the isentrope and the isotherm, the series of states can be reached continuously. For the Hugoniot, the locus of all states which can be reached with shocks is achieved with no heat exchange in going from the initial to the final state. The energy given by eq (3.6) is always greater than the area under the Hugoniot curve. The increase in energy from the isotherm curve to the isentrope curve and then to the Hugoniot curve leads to progressively higher temperatures for the same compression.

In addition to the $P - V$ plane, two others are most useful in interpreting experimental results. The $U_s - U_p$ plane is used in graphical solutions of experimental data of two (or more)

materials. When a shock wave passes from one material into another, the boundary conditions are such that the pressure and particle velocity are equal across the interface. The $U_s - U_p$ plane is used to establish certain thermodynamic properties and phase transitions (which show up as breaks in the slope if the phases are distinctly different).

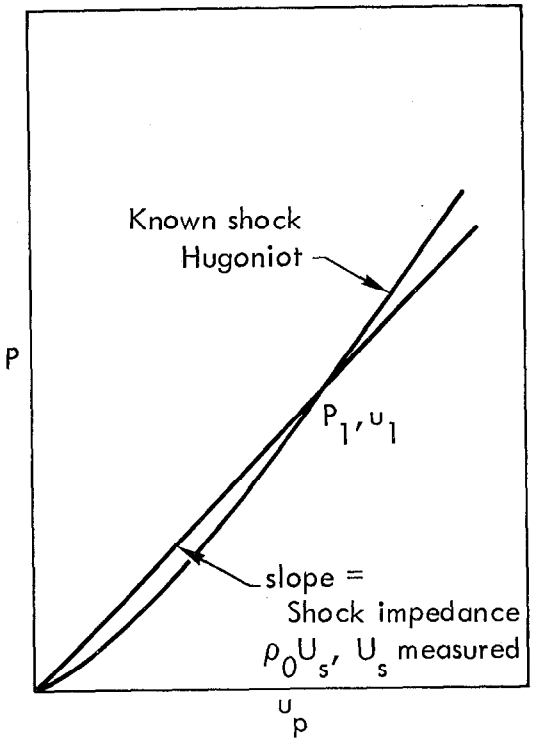


FIGURE 3.3 DETERMINATION OF $P$, $U_p$ FROM KNOWN HUGONIOT

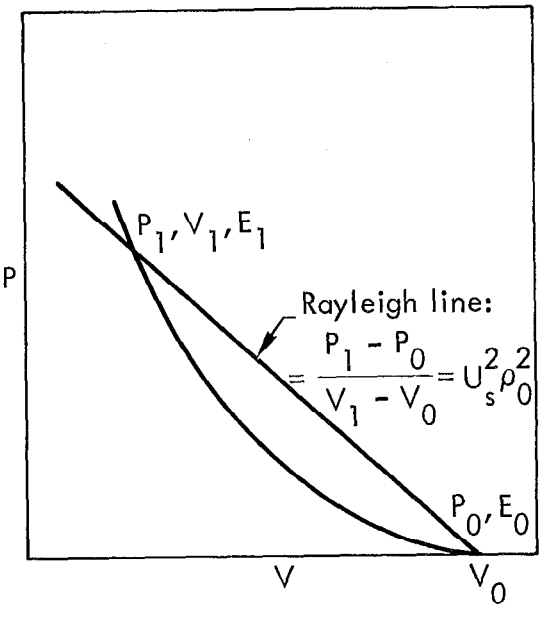


FIGURE 3.4 HUGONIOT IN $P - V$ PLANE

## 3.3 IMPEDANCE MATCHING TECHNIQUES

The mass flux $\rho_o U_s$ is called the shock impedance of the material. Transposing eq (3.2) gives

$$\rho_o U_s = P_1 / U_p \tag{3.10}$$

The shock impedance shows up as the slope of a straight line passing through the origin in the $P - U_p$ plane. For a material with a known Hugoniot, the measurement of the shock velocity and the initial density of the material will determine the pressure and particle velocity uniquely as shown in Fig 3.3. When a second material (II) with an unknown Hugoniot is placed against the first material (I) and the shock waves crosses the interface, the following occurs. Figure 3.5 depicts the possible pressure profiles across the interface. Upon impact with material II, a shock wave of magnitude $P_2$ is propagated into the second material. If the dynamic impedance of the second material is lower (Fig 3.5.b), then a rarefaction wave (adiabatic release wave) is propagated back into the first material, while a shock wave with a lower magnitude $P_2$ is propagated into the second material. On the other hand, if the dynamic impedance of the second material is higher (Fig 3.5.c) then a shock wave of higher magnitude $P_2$ is reflected back into the first material. The boundary condition at the interface is the same for all cases. Both the pressure and particles velocity are continuous at the interface.

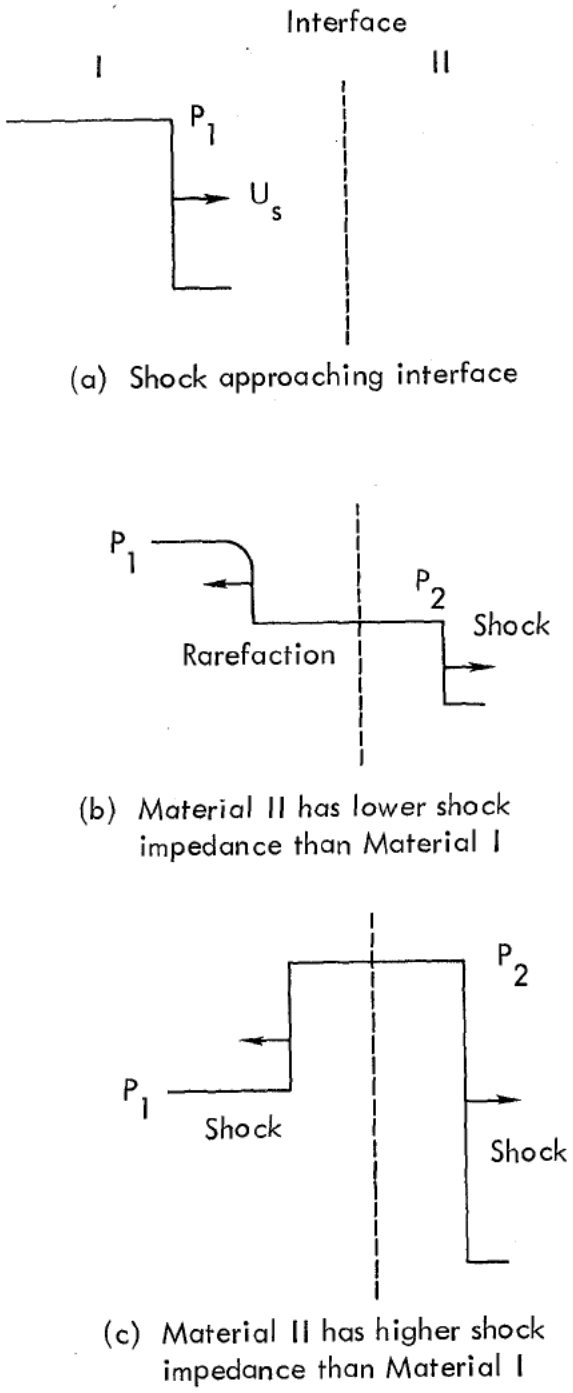


(a) Shock approaching interface

(b) Material II has lower shock impedance than Material I

(c) Material II has higher shock impedance than Material I

FIGURE 3.5 POSSIBLE PRESSURE PROFILES ACROSS INTERFACE

Figure 3.6 depicts the impedance matching techniques used in finding the Hugoniots of FeSi alloys which have higher impedances than aluminum (which is used as a base plate and a standard). The initial densities and shock velocities are measured for both materials. The initial shock pressure and particle velocity of aluminum are found at point A. The dynamic state behind the reflected wave (has the same pressure and particle velocity for both materials) is found by the intersection at point B of the mirror image of the Hugoniot of aluminum about point A and the Hugoniot of the unknown FeSi alloy. This, of course, is equivalent to the intersection of the dynamic impedance of the FeSi alloy with the reflected aluminum Hugoniot. Thus, a series of experiments at different pressures will determine the Hugoniot of the FeSi alloys.

If the unknown material has a lower shock impedance than aluminum, then the rarefaction wave reflected back into aluminum is used to find the Hugoniot of the unknown material. In general, a full equation of state must be known, because the rarefaction velocity is given by

$$U_r = \int_{P_o}^{P} - \left(\frac{\partial V}{\partial P}\right)_S^{1/2} dP \qquad (3.11)$$

The rarefaction is also known as an adiabatic release wave because the condition $dS = 0$ is satisfied. At pressures up to a Megabar, the assumption that $U_p = U_r$ (in magnitude) holds for most stiff (dense, high melting point) materials to about 2% to 5% and is known as the "free surface approximation."

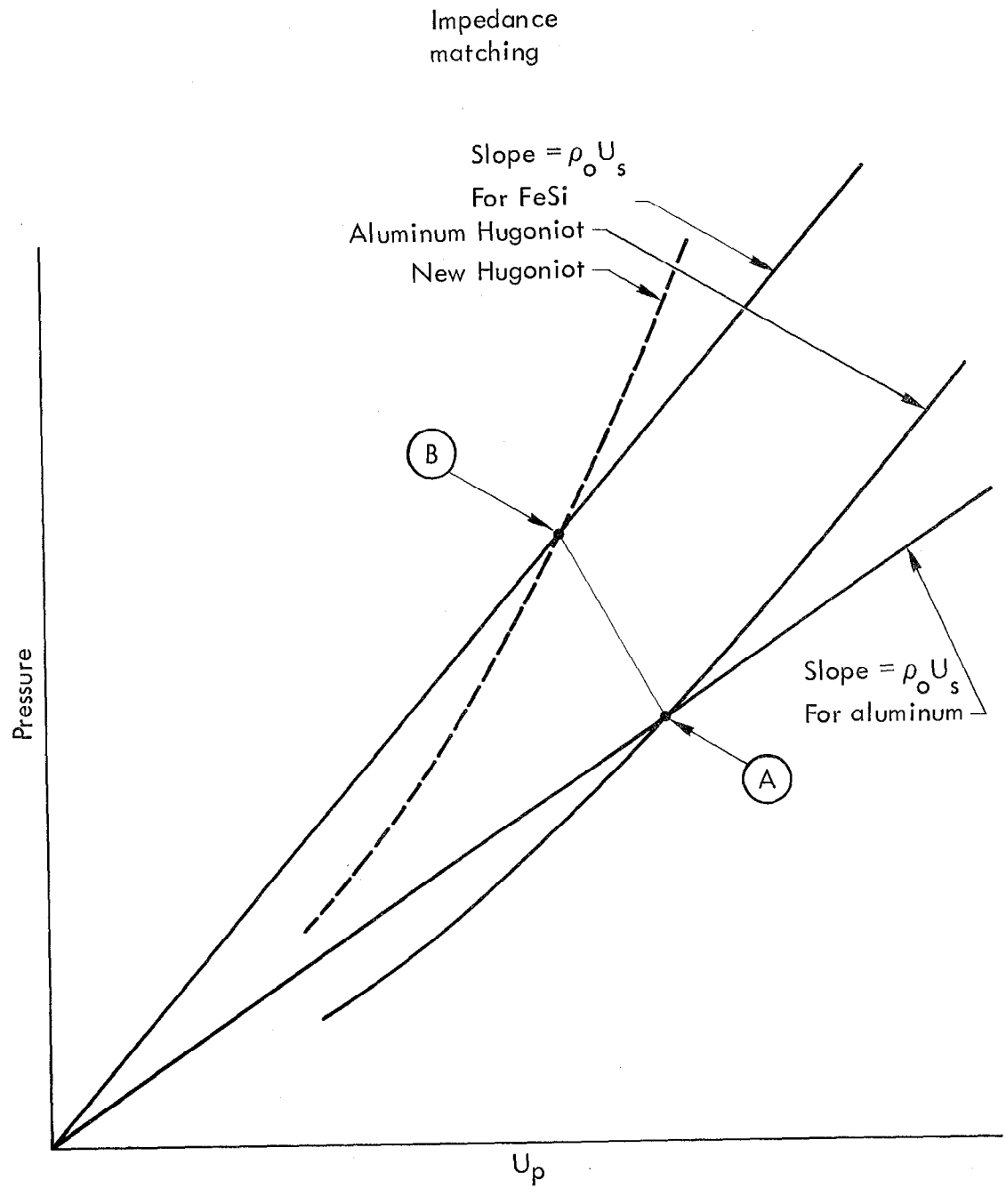


FIGURE 3.6 IMPEDANCE MATCHING TECHNIQUE

If the second material is a vacuum (or air), then its Hugoniot is given by the $U_p$ axis and the resultant free surface velocity of the aluminum is given by

$$U_{fs} = U_p + U_r \simeq 2U_p \tag{3.12}$$

In practice, $U_{fs}$ can be measured to an accuracy of about 2% up to 500 Kbars and can be used as a check upon semiempirical EOS's. However, these EOS's are usually not sensitive enough in the $P - U_p$ plane for the $U_{fs}$ measurements to be used to discriminate among them. Above 500 Kbars, the integrity of the free surface is compromised by jetting, warping and disintegration. Therefore, the impedance matching technique is most often used to determine the Hugoniot of an unknown material.

## 3.4 OFF-HUGONIOT MEASUREMENTS

The impedance matching technique is used in this work to reach off-Hugoniot states in thin conductivity samples of FeSi sandwiched between two thick alumina (polycrystaline $Al_2O_3$) plates. Previous work by Royce (R. N. Keeler, et al, 1970) on iron demagnetization assumed that the final shock state in the thin metal samples was the same as that characterizing the alumina. The final state in iron was reached by reverberations between the two alumina plates. Since the shock impedance of alumina is not too far from that of iron, he reasoned that the reverberations are small compared to the initial shock wave and the final sample state reached in iron is just the state reached in a single shock in alumina.

The reverberations are considered here in more detail because it is not only the final pressure reached that is important but also the final volume. The conductivity of the shocked state will depend upon the actual compression of the FeSi alloy achieved in the off-Hugoniot state.

The reverberating shock waves and rarefactions are depicted in Fig 3.7, 3.8, and 3.9. Point 1 describes the first shocked pressure and particle velocity and volume in alumina just prior to the shock wave reaching the FeSi alloy. Point 2 describes the highest pressure $P_2 = P_H$, and the corresponding volume $V_H$ reached on the FeSi Hugoniot (along the reflected alumina Hugoniot from point 1 to 2) after the shock has passed through the conductivity sample. Point 3 describes the first rarefaction wave as it propagates back into the FeSi sample. The pressure has dropped along the FeSi isentrope to $P_3$. Point 4 describes the second shock wave and the pressure reached along the FeSi Hugoniot. The "final" pressure $P_F$ is then reached by a second rarefaction wave within FeSi. The calculated pressures $P_1$, $P_4$ and $P_F$ were all within 1% of each other. The calculation methods and results are described in Section 7. This fully justifies Royce's assumptions with respect to pressure.

The importance of the volume correction $\delta V$ becomes evident in Fig 3.9 where the volume associated with point 1 is quite different from that reached in the final state. The volume correction ( $\delta V$ ) calculations and their effects are discussed in Section 7.

FIGURE 3.7 PRESSURE PROFILES FOR OFF-HUGONIOT STATE

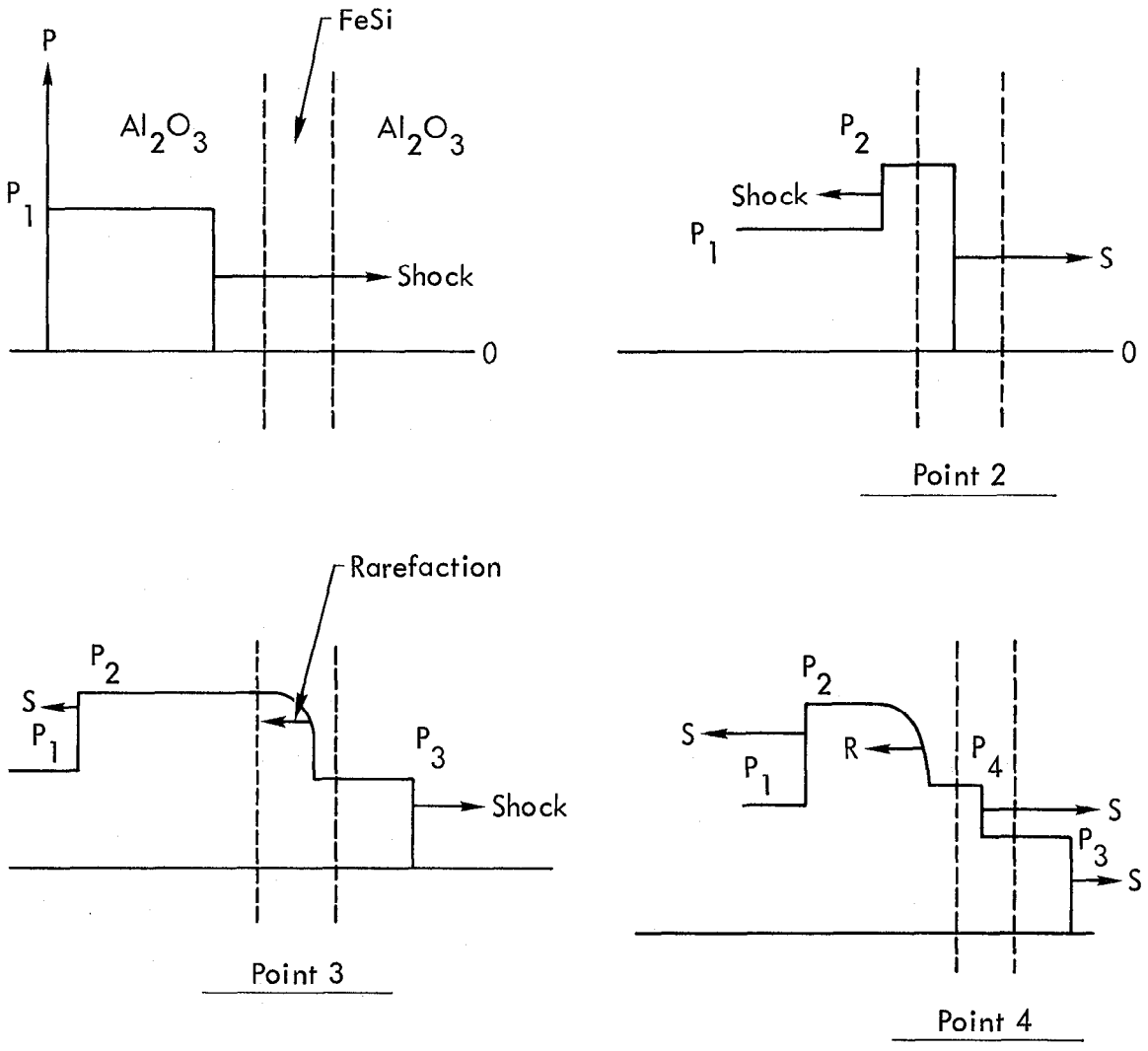


Boundary conditions at each interface

P continuous

$U_P$ continuous

FIGURE 3.8 P VS $U_p$ FOR OFF-HUGONIOT STATE

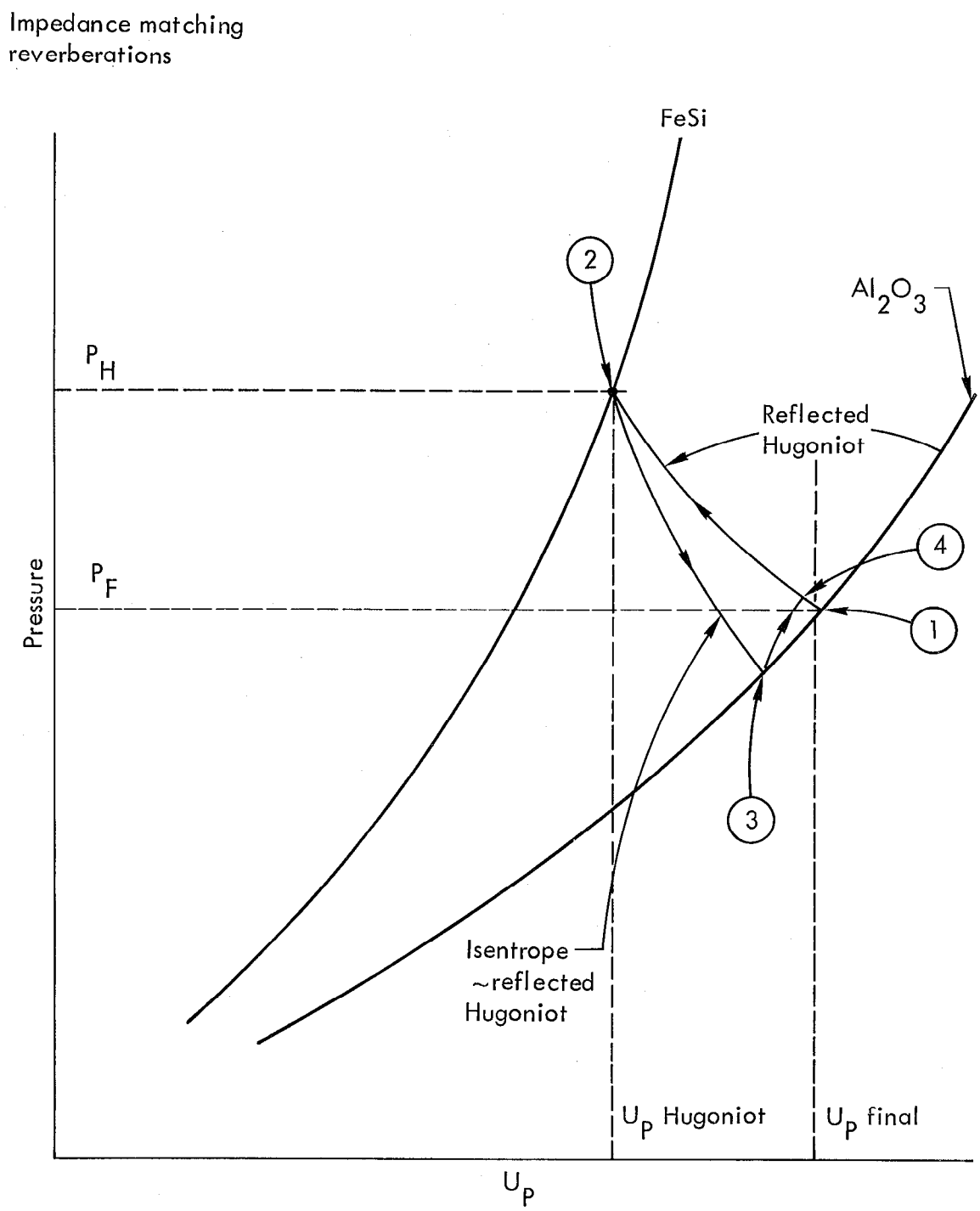

FIGURE 3.9 P VS V FOR OFF-HUGONIOT STATE

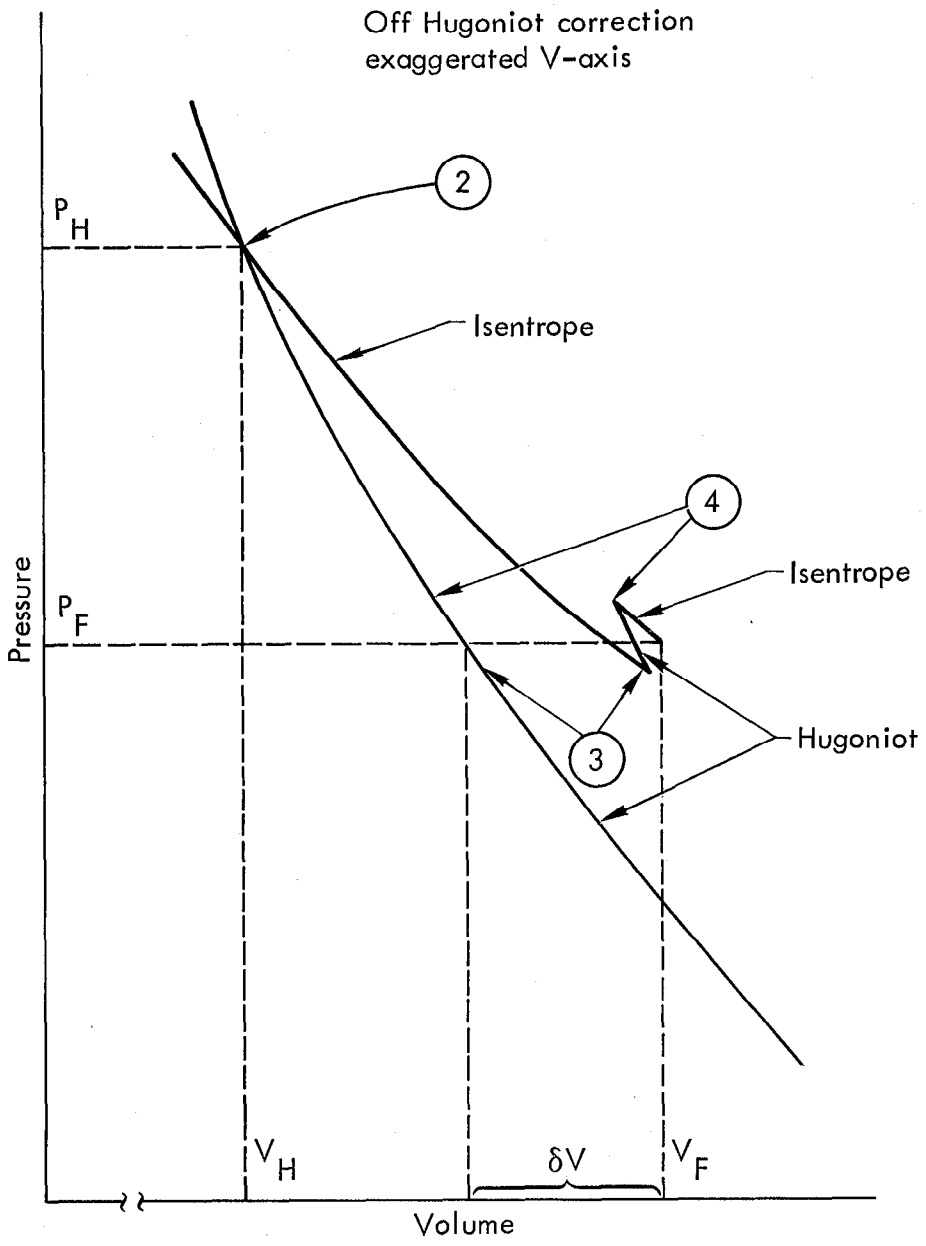

The associated reverberation times are shown (in Section 6) to be fast and the reverberations are over in a time that is short compared to the shocked state in which the conductivity measurements are made.

## 3.5 SEMI-EMPIRICAL EQUATIONS OF STATE

The use of a semi-empirical equation of state (EOS) is required to calculate the $\delta V$ correction and the temperature in the conductivity experiments as well as to calculate the bulk properties of FeSi along an isentrope (for comparison with Earth models). The properties of materials under high pressures and temperatures are determined by the internal energy (due to cohesive forces along the $0^{o}K$ isotherm), by the thermal vibrations of atoms and by the thermal exitation of electrons. Various methods for describing the above three contributions to the EOS and the use of Hugoniot data lead to a number of theories.*

The largest thermal compression contribution is due to atomic vibrations. At normal densities, the potential barrier for atoms in a lattice is on the order of one to several electron volts and is much higher than the average vibrational energy of the atoms. This barrier is equivalent to tens of thousands degrees. Under compression, the repulsive forces raise the heights of the potential barriers. This means that the harmonic oscillation approximation is valid over a wide temperature range. The anharmonic effect of

---

*See references cited in the footnote of Section 3.2.

interatomic interaction can be taken into account by allowing the various normal modal frequencies to be volume dependent. The simplest form is the Grüneisen EOS,

$$P(V,E) - P_c(V) = \gamma(V)(E - E_c(V))/V \qquad (3.13)$$

where the assumption is that gamma, $\gamma(V, T)$ is a function of volume only and is independent of temperature or thermal energy ( $E - E_c(V)$ ).

It has been shown (for instance Keeler, et al, 1971) that the Grüneisen gamma and the thermodynamic gamma, defined as

$$\gamma(V,T) = V(\partial P/\partial E)_V = V(\partial P/\partial T)_V/(\partial E/\partial T)_V \quad , \qquad (3.14)$$

(and $\left(\frac{\partial E}{\partial T}\right)_V = C_v$ is the Dulong-Petit classical limit)

are equivalent only if the thermodynamic gamma is independent of temperature. The assumption of equipartition of energy between normal modes is justified for most metals because their Debye temperature is below or near room temperature (the Debye function $D(\Theta/T)$ approaches 1 when $T$ is greater than the Debye temperature, $\Theta = h\nu/k$, where $\nu$ is the frequency of lattice vibration, $h$ is Plank's constant and $k$ is Boltzmann constant).

The initial value of $\gamma$ (at $V_o$) is given by (Kittel, 1966) $\gamma_o = \frac{3\alpha}{\rho_o \kappa C_v}$, where $\alpha$ is the coefficient of linear expansion, $\kappa$ is the coefficient of compressibility, $\rho_o$ is the

initial density and $C_v$ is the specific heat at constant volume. Alternately, $\gamma_o = \frac{3\alpha}{C_p} \phi^2 M$ where $C_p$ is the specific heat per mole at constant pressure, $\phi$ is the seismic parameter (defined by eq 2.9), and $M$ is the mean molecular weight. Ultrasonic measurements of the longitudinal and transverse velocities can thus be used to help determine $\gamma_o$ .

The behavior of $\gamma(V)$ as a function of volume can be obtained with the help of a model. Several models relate the gamma to the curvature of the cold compression curve. The generalized form is given as

$$\gamma(V) = (a/2 - 2/3) - V/2 \frac{\frac{d^2}{dV^2}(P_c(V)\, V^a)}{\frac{d}{dV}(P_c(V)\, V^a)} \qquad (3.15)$$

where $a = 0$ gives Slater's model (with the assumption that Poisson's ratio is independent of volume); $a = 2/3$ gives Dugdale and MacDonald's model (this has been rederived for cubic materials); and $a = 4/3$ gives Zubarev and Vashchenko's free volume theory. If Hugoniot data can be represented in the $U_s - U_p$ plane by a straight line, $U_s = C + S\, U_p$ , then

$$\gamma_o = 2S - 2/3 - a/2 \quad \text{at } V_o \qquad (3.16)$$

The comparison of this value with the thermodynamic data is best for the Dugdale - MacDonald theory for common metals. It must be pointed out that the various $\gamma(V)$'s approach each other at higher pressures. Therefore, the particular choice of $\gamma_o$ will not have a significant effect at high pressures.

The practical generation of a Grüneisen EOS from an experimental Hugoniot proceeds as follows. Solving eq (3.13) for gamma gives

$$\gamma(V) = V \frac{P_H(V) - P_c(V)}{E_H(V) - E_c(V)} \quad , \tag{3.17}$$

and rewriting eq (3.15) for the Dugdale MacDonald model gives

$$\gamma(V) = -1/3 - \frac{V \frac{d^2}{dV^2}\left( P_c(V)\, V^{2/3} \right)}{2 \frac{d}{dV}\left( P_c(V)\, V^{2/3} \right)} \tag{3.18}$$

Substituting $P_c(V) = -\dfrac{dE_c(V)}{dV}$ (3.19)

into eq (3.17) and (3.18) and eliminating $\gamma(V)$ between the two equations gives a third order differential equation for $E_c(V)$ which can be solved numerically. Then equations (3.19) and (3.18) are used to find $P_c(V)$ and $\gamma(V)$.

In order to calculate the velocity of a rarefaction wave $U_r$ along an isentrope, both $E_S(V)$ and $P_S(V)$ must first be found along the isentrope. Using Grüneisen's EOS again,

$$E_S(V) - E_H(V) = V\left( P_S(V) - P_H(V) \right)/\gamma(V) \quad , \tag{3.20}$$

Differentiating it with respect to volume and substituting $P_s(V) = -\dfrac{dE_s}{dV}$ gives a first order differential equation for $P_S(V)$ which can be solved numerically. $E_S(V)$ is found by finding the area under the $P_S(V)$ curve. The rarefaction velocity is then found by numerical solution of eq (3.11).

In order to calculate thermodynamic properties such as the temperature and entropy, the specific heat at constant volume $C_V$ must be known or specified. The Debye model for specific heat, $C_V(V, T) = C_V D(\Theta(V)/T)$, is used for solids. The volume dependence of the Debye temperature $\Theta(V)$ is found by integrating

$$\gamma(V) = -\frac{d \ln \Theta(V)}{d \ln V} \tag{3.21}$$

The electronic contribution to the specific heat due to the free conduction electrons should be added at high temperatures. At high temperatures, the electronic density of states at the Fermi surface begins to become significant. The temperatures reached in the present shock experiments are below the Fermi energy but the contribution is not insignificant.

Using the first law of thermodynamics

$$TdS = dE + PdV \tag{3.22}$$

and the thermodynamic identity

$$TdS = C_V dT + (\partial P/\partial T)_V TdV \tag{3.23}$$

and combining them gives

$$dE + PdV = C_V dT + (\partial P/\partial T)_V TdV \tag{3.24}$$

Differentiating eq (3.24) with respect to volume along the Hugoniot gives

$$\frac{dE_H(V)}{dV} + P_H(V) = C_v(V,T)\frac{dT_H(V)}{dV} + (\partial P/\partial T)_V T_H(V) \qquad (3.25)$$

solving eq (3.14) for $(\partial P/\partial T)_V$ gives $\left(\frac{\partial P}{\partial T}\right)_V = \frac{\gamma(V)\ C_v(V,T)}{V}$ and substituting it in eq (4.25) results in a differential equation for $T_H(V)$ along the Hugoniot. This equation can be integrated numerically to yield the temperature along the Hugoniot.

Along an isentrope (where $dS = 0$), eq (3.24) becomes

$$C_v dT + (\partial P/\partial T)_V\, TdV = 0 \ . \qquad (3.26)$$

This equation can be solved for the temperature to give

$$\ln\frac{T}{T_i} = -\int_{V_i}^{V}\frac{\gamma(V)}{V}dV \qquad (3.27)$$

where $T_i$, $V_i$ is some initial condition. The initial condition can be picked as a point which is the intersection of a Hugoniot and isentrope. Now, a complete EOS can be generated in the vicinity of the measured Hugoniot.

The effects of polymorphic transitions (from one solid phase to another) can be observed as breaks on the $U_s - U_p$ or the $P - V$ plots of Hugoniot data. A first order phase transition in the $P - V$ plane is shown in Figure 3.10a. For pressures below $P_1$ and above $P_3$, ordinary shock waves are observed. Both states 1 and 3 lie on the common Rayleigh line and have the same propagation velocity $U_{s1}$, $U_{s3}$ given by eq (3.14).

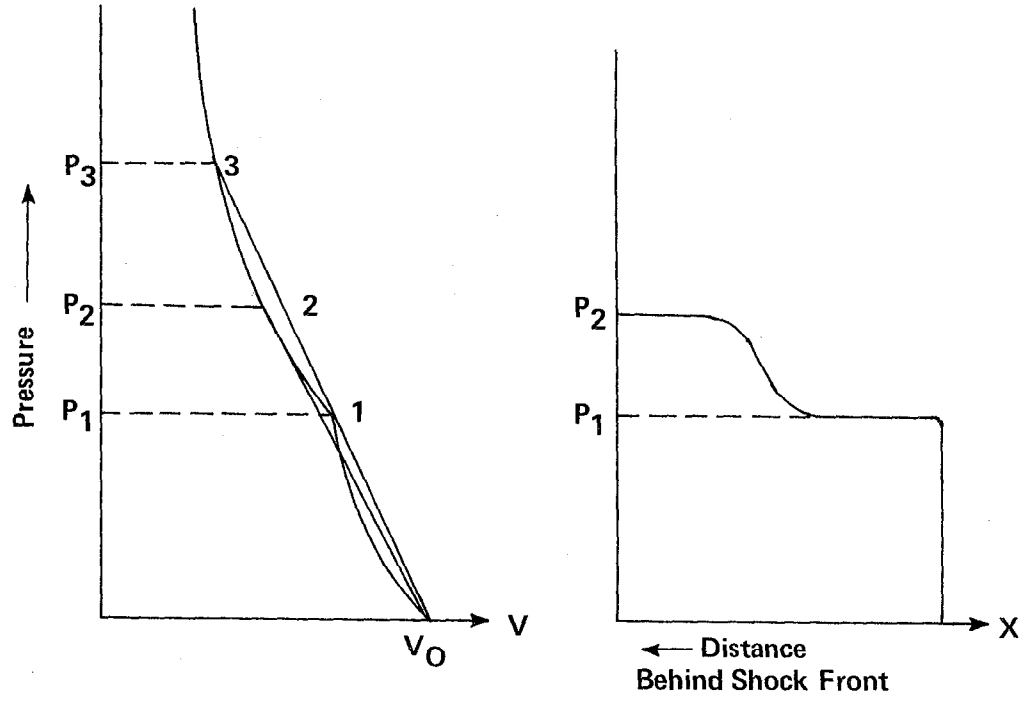


(a) - PLANE (b) DOUBLE SHOCK FRONT

FIGURE 3.10 FIRST ORDER PHASE TRANSITION

For states between 1 and 3, direct transitions to a state 2 are unstable. The shock velocity $U_{s2}$ of state 2 is slower than that of state 1 (which also has a lower emplitude). This leads to the formation of two shock fronts (Fig 3.10b), with the first shock wave having the critical pressure $P_1$ of the first phase. The velocity of the second shock wave depends upon the applied pressure $P_2$ and is given by

$$U_{s2} = U_{p1} + V \sqrt{( P_2 - P_1 )/ ( V_1 - V_2 )} \qquad (3.28)$$

At pressures just above $P_1$, the rate of transformation to the new phase is most sluggish (and can be as slow as 200 nanosec for iron as an example). As the pressure $P_2$ approaches $P_3$, the rate of transformation speeds up and approaches the normal 10 to 20 nanoseconds. Above $P_3$, the polymorphic transformation proceeds at the rate characteristic of the ordinary shock front. This shows up as a smooth (and linear in most cases) relationship in the $U_s$ - $U_p$ plane.

The region of metastable phases is not large for most metals because the change in volume $\Delta V$ of the transition is small. These transitions have not been successfully analyzed for iron (Duff and Minshall, 1957; Altshuler, 1965). Experimentally, the change in enthalpy $\Delta H$ can not be measured along the Hugoniot and therefore semi-empirical methods can not be used. The phase change contribution to the EOS is small and is ignored at pressures well above the transition.

The present work on the FeSi alloys is well above the transition pressures which have been measured for a series of Si concentrations in FeSi alloys (E. G. Zukas, C. M. Fowler, F. S. Minshall, and J. O'Rourke, 1963).

## 4.0 IRON-SILICON ALLOYS

The relevant portion of the phase diagram, thermodynamic and physical properties of iron-silicon alloys are reviewed. Sample preparation and characterization of the initial states of both shock wave and conductivity samples is described.

## 4.1 PHASE DIAGRAM

Understanding the phase diagram of the iron silicon alloys at one atmosphere and at high pressures is necessary to characterize the initial and final states of the Hugoniot and electrical conductivity experiments.

Because the alloys were prepared from a liquid, the samples may contain more than one phase. The iron silicon system at one atmosphere is shown in Fig 4.1 for silicon concentrations $0 \leq X_{si} \leq 0.5$. There are seven distinct phases in this region. The structure of the phase diagram is discussed in detail in Appendix B.

Three of the phases are called daltonides (stable over a narrow range of composition). They are: Phase $\beta$ ($Fe_2Si$), which is a high temperature phase which decomposes below 1040°C; Phase $\eta$ ($Fe_5Si_3$), another high temperature phase (1090 to 825°C) which is metastable below 825°C and can be retained at room temperature by quenching and is ferromagnetic below 90°C; Phase $\epsilon$ (FeSi), which is stable throughout the temperature range.

The other four phases are called berthollides. These phases are stable over various ranges of composition where the silicon enters the crystalline matrix by substitution of iron at the lattice sites. Since the atomic size of the two species is similar (Fe atomic diameter 1.26Å, Si atomic diameter 1.17Å), the atomic spacing changes more slowly than the density. A high temperature phase, $\gamma$ , exists up to $X_{si} = 0.025$ and coexists with the $\alpha$ phase up to $X_{si} = 0.045$. This phase was easily avoided by using

FIGURE 4.1 IRON SILICON PHASE DIAGRAM

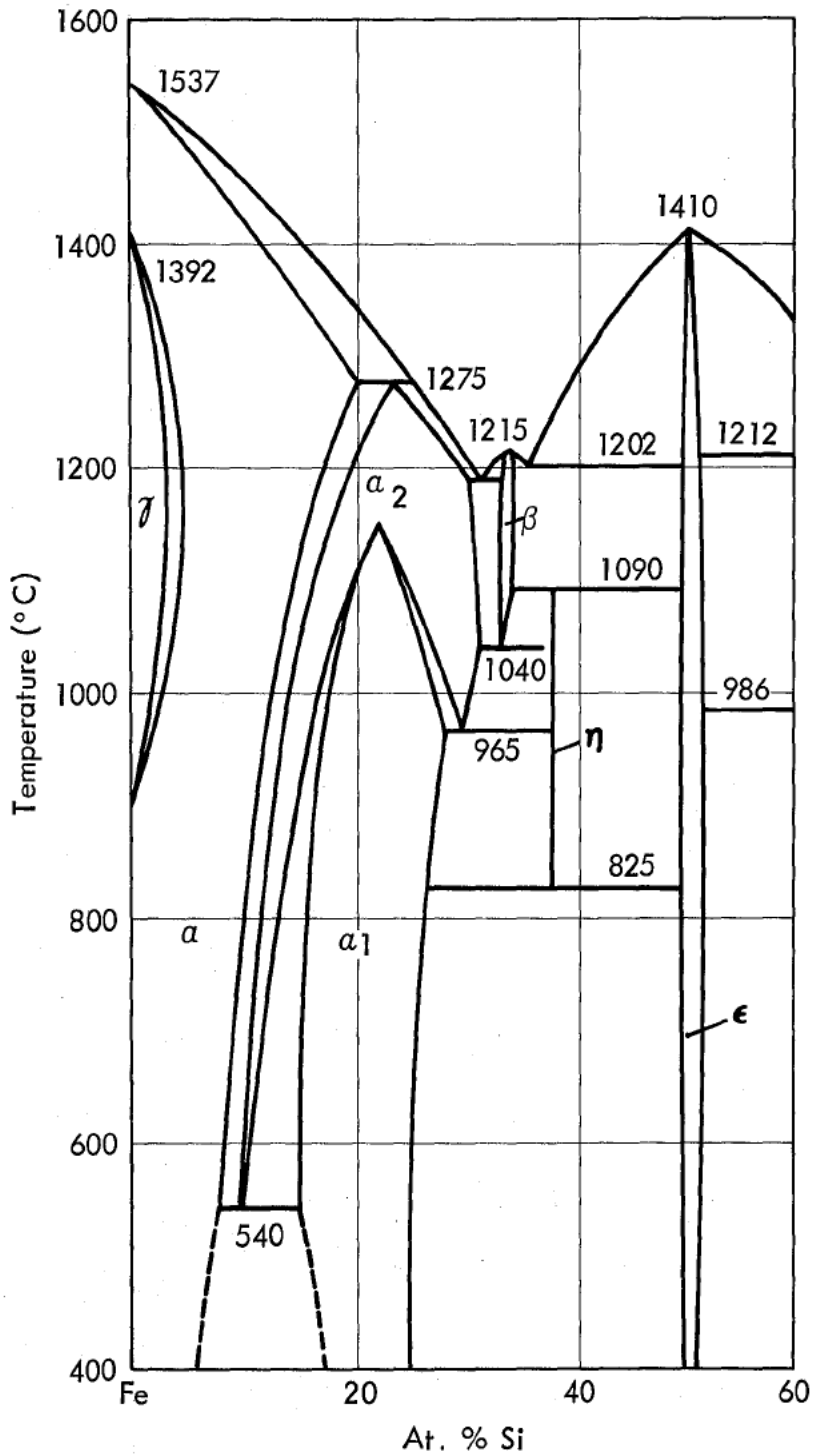

melt concentrations of $X_{si} \geq 0.077$. As can be seen from the phase diagram, the solidus and liquidus curves follow each other closely and the $\gamma$ phase cannot be reached with the melt starting at $X_{si} = 0.077$. The other three berthollide phases are $\alpha$, $\alpha_1$ and $\alpha_2$, all having a body centered cubic (bbc) structure with a continuous and narrow range of atomic lattice constants. These phases differ from each other only by exhibiting second order phase effects. Phase $\alpha$ is disordered, $\alpha_1$ shows short range order and $\alpha_2$ shows long range order. For our applications, phases $\alpha$, $\alpha_1$ and $\alpha_2$ can be considered to be one equivalent bcc phase with a varying silicon concentration. At room temperature, above $X_{si} = 0.25$, phase $\alpha_1$ coexists with phase $\epsilon$ and the metastable phase $\eta$.

Fortunately for the experiments, the details of the second order phases and their transition regions do not affect the bulk properties and electrical conductivity of the high pressure phase reached in the shock experiments.

Relatively little work has been done on FeSi alloys at hydrostatic and shock pressures. Tanner and Kulin (1961) have measured the effect of pressure on the $\gamma$ phase of the FeSi alloy at 42 Kbars hydrostatically. They found that the temperature of the transformation was lowered by about 250°K and the $\gamma$ phase extended to at least $X_{si} = 0.07$. They did not follow the transformation to higher silicon concentrations. The calculated transformation temperature agreed with the experiment at low silicon concentrations and the disparity between experiment and calculation grew at increasing silicon concentrations.

Clendenen and Drickamer (1966) have statically investigated two concentrations of FeSi alloys, $X_{si}$ = 0.08 and "$Fe_3Si$" ($X_{si}$ = 0.25) to 216 and 282 Kbars respectively as well as pure iron to about 200 Kbars. The $X_{si}$ = 0.08 alloy had a compressibility very near that of iron. This is in agreement with some early work at $X_{si}$ = .0575 to 30 Kbars (Bridgeman, 1964). The alloy transformed to a hexagonal close-packed structure (hcp) similar to that of iron (see for example, the review of the effect of pressure upon phase diagrams by D. Young, 1975). The high pressure phase and its transition were not studied in detail but at 150 Kbars, c/a was measured to be 1.67. The c/a ratio is very close to that of hcp hard spheres where c/a = 1.633. The compressibility of "$Fe_3Si$" was found to be somewhat less than of pure iron. The important point to note is that at higher pressures FeSi alloys transform into a hcp structure.

The transformation of pure iron from bcc $\alpha$ phase to hcp $\epsilon$ phase (which should not be confused with the FeSi $\epsilon$ phase) was measured by many workers both statically and dynamically. Early static and shock experiments showed the transformation to occur at about 130 Kbars (Bundy, 1965; Fuller and Price, 1962). Mitchell and Keeler (1967) presented evidence suggesting that the transformation starts at lower pressures. This evidence was duplicated by subsequent shock experiments (Wong, et al, 1968; Keeler and Mitchell, 1968 and 1969). The transition was observed to start at 80 and 50 Kbars respectively. Static X-ray diffraction work (Giles, et al, 1969) reported the transition

to occur at 70 $\pm$10 Kbars. The transition pressure is still not fully resolved (see, for example, Liu and Bassett, 1975).

The high pressure hcp phase of pure iron was found to be nonferromagnetic by static, dynamic recovery and Hugoniot techniques. X-ray diffraction photographs under static pressure established that the high pressure phase of iron has a hexagonal close packed structure (Jamieson and Lawson, 1962; Takahashi and Basset, 1964). Mossbauer measurements of the hcp phase at static pressures have positively confirmed that the state is nonferromagnetic (Pipkorn, et al, 1964; Millet and Decker, 1969). Shock experiments measuring the electrical conductivity of iron (Keeler, et al, 1968) and the demagnetization of iron and iron silicon alloys (Royce, 1968 and 1970; Graham, 1968) have also confirmed that the hcp phase is paramagnetic. The results of these shock experiments are discussed in Section 7.2. The effects of the analogous transformation of the FeSi alloys shall be discussed in Sections 6.0 and 7.0.

Shock wave experiments on seven FeSi alloys and iron ($X_{si}$ = 0.009 to $X_{si}$ = 0.13) were performed (Zukas, Fowler, Minshall and O'Rourke, 1963) investigating the phase transition from $\alpha$ to hcp. Investigation of $X_{si}$ = 0.056 found that the transition pressure was not dependent on crystal orientation. Single crystal (only concentration at which single crystals were obtained) samples of 100, 111, and 112 orientation as well as polycrystaline samples showed the same transition pressure of 145 Kbars. They also found that the transition pressure followed a linear relationship

as a function of silicon concentration from 130 Kbars for iron to 160 Kbars for $X_{Si} = 0.087$. This has been interpreted to mean that no evidence of the $\gamma$ phase was seen. The $\gamma$ phase would have caused a discontinuity in the straight line. The transition pressure of the $X_{Si} = 0.13$ sample was not uniquely determined because the authors acknowledged that they could have overdriven the shot. A similarly overdriven experiment at $X_{Si} = 0.037$ showed an apparent transition pressure of 151 Kbars which was subsequently found to be 139 Kbars by more careful experiments. A third finding was that the two wave region extended from the transition pressures to about 320 Kbars. For all silicon concentrations, the single wave region was seen for pressures above 320 Kbars extending to the high pressure limit of the experiments at 480 Kbars. The Hugoniots above 320 Kbars were well behaved and none of them overlapped each other.

Two separate shock wave Hugoniot studies were made at high pressures of three FeSi alloys. Their results are included in Section 7.1.

## 4.2 THERMODYNAMIC PROPERTIES OF FeSi ALLOYS

An assessment of 47 references was made by Chart (1970) on the thermodynamic properties of the iron-silicon system. A subsequent analysis of the same and newer references was made by Hultgren, et al (1973) in which some of the derived values have been changed. Some differences between the two reviews are attributed by Hultgren to the use of slightly different phase diagrams. In spite of the large number of references used, there

was insufficient data in the high temperature region (at one atmosphere pressure) for silicon concentrations below $X_{si} = 0.5$. Specifically, the only concentration between $X_{si} = 0$ and $X_{si} = 0.50$, that has any data worth reporting is $X_{si} = 0.25$. The high temperature data on the specific heat at constant pressure ( $C_p$ , and its integral, $S_T - S_{st} = \int_{st}^{T} C_p \, dT$ , the change in entropy from the standard state at 298.15°K to the temperature, T , in question) extends up to 1300°K. This is 230°K below the melting point. Consequently the change in entropy upon melting of the alloy, $X_{si} = 0.25$, could not be obtained.

The low temperature electronic specific heat coefficient has been measured for iron-silicon, iron-germanium and iron-tin alloys (Gupta,et al, 1964). It was found that the addition of these alloying elements to iron do not increase the Fermi energy in the d-band in their alloys with iron. The results are shown in Table 4.1 for iron silicon alloys together with iron and silicon for comparison. The Debye temperature, $\Theta$ , is also given in the table.

TABLE 4.1

ELECTRONIC SPECIFIC HEAT

| $X_{si}$ | $\gamma_e X 10^4$ cal/g atom deg$^2$ | $\Theta$ °K |
|---|---|---|
| 0 | 12.0 | 464 |
| .039 | 12.2 | 450 |
| .078 | 12.6 | 413 |
| .138 | 11.6 | 421 |
| .245 | 11.65 | 397 |
| 1.0 | 0 | --- |

This completes the listing of the thermodynamic and physical properties that had to be obtained from the literature in order to perform the data reduction and analysis. All other properties needed in the calculation have been measured within this work and will be described as needed.

## 4.3 SAMPLE PREPARATION

The bulk ingots for three of the four FeSi alloy concentrations were obtained from Materials Research Corporation (Orangeburg, NY) on a purchase order based on competitive bidding. The purchase order requested Silicon concentrations by weight, at 5%, 10%, and 20% plus or minus 0.5% by weight. These concentrations were chosen with the help of the available phase diagram to span the desired Silicon range with a smooth transition from iron while avoiding the multiple phases where possible (Hansen, 1958). The ingots were to be void free and impurities were not to exceed 0.05% by weight. The actual starter materials were specified to be VP grade with the lot analysis of the starter materials requested. The anticipated purity was about a factor of ten better than specified. The method of preparing the castings was specified as induction melting and casting in a vacuum. This ellimiated the problem of contamination of the alloys with electrode materials encountered by Balchan and Cowan (1966) when they prepared FeSi alloys by the electrode melting technique.

The ingots, emission spectrographic analyses of starter materials, analysis of Si concentration, and certification of materials were received with the remark: "The Iron-Silicon alloys

are extremely brittle. Fracture occurred during attempts to machine the surface." The remark was confirmed on numerous ocassions.

The lot analysis of the starter materials revealed impurties in iron to be less than 78 parts per million (pps) 0; 50 ppm Mo; 40 ppm Cu; the other 23 elements (mostly metals) were below 40 ppm each, typically being 10 ppm. Silicon was much cleaner, showing less than 0.5 ppm 0, and traces of B and P with no other elements detected. The chemical analysis revealed the measured Silicon concentrations to be 4.0%; 10.0%, and 20.7% by weight with an accuracy of $\pm 0.5\%$ or better.

Two types of samples were made:

a. Equation of State Samples. These samples were to be placed into standard holders of a long EOS experimental series called Ester at Lawrence Livermore Laboratory (known at the time as The Lawrence Radiation Laboratory). At certain times in the Ester series, there was room to fit up to four samples per shot when another material had to be tested on short notice. The standard sample sizes required were 1/4 inch thickness for $U_s$ measurements and 1/8 inch thickness for $U_{fs}$ measurements, both of 1 inch diameter.

b. Conductivity Samples. Samples that were to be used in the conductivity measurement experiments ideally should have been flat thin strips at least 2.5 cm long and on the order of 0.05 cm thick.

It was decided not to subject any of the samples during fabrication to elevated temperatures so as not to encourage any

solid state transformations. In addition, a method of fabrication was found which did not stress the material. A fixture was built to cut the bulk material by sputtering or spark erosion. The method involves mounting the material to be cut on a conducting plate that is insulated from the rest of the equipment. The material is immersed in a non-corrosive, non-conductive fluid such as kerosine. A voltage of about 2,500 volts is applied between the material and another conductor in the form of a wire for linear cuts or in the form of a hollow cylinder for forming cylinders. As the two conductors being to touch, a current starts to pass between them. The resultant sparks erode both of the conductors if the rate at which the conductors are brought together is slower than the rate of erosion (which unfortunately could not be speeded up). A typical cut through 0.6 cm thickness took from one to three hours depending upon the length (or circumference) of the cut. This method has been used by others (Balchan and Cowan, 1966; Alberts and Wedepohl, 1971; Inden and Pitsch, 1972) to fabricate brittle samples.

The EOS samples were finished flat and parallel to an accuracy of $\pm 0.00025$ cm by surface griding at a rate slow enough so as not to heat the samples past a temperature uncomfortable to the touch. A decision was made to make the sample diameter 3/4 of an inch rather than 1 inch in order to avoid the central portion along the axis of each 2 inch diameter ingot. Ultrasonic inspection revealed shrinkage cracks in one ingot along the axis which were avoided in subsequent samples. Compensating rings were made so that each

sample would fit the 1 inch diameter slots. Each surface was inspected for cracks and voids under ultraviolet light after being immersed in fluoroscene dye. Since the surface tension of the dye is extremely small, this technique can spot cracks not visible to the unaided eye. The EOS samples were also X-rayed and the shadow graphs inspected for any voids or other imperfections.

Several 1/2 inch thick disks of 10% by weight Silicon were homogenized at 1423°K (below the melting point of the eutectic, vis Figure 4.1) for 30 hours. The recommended procedure for ensuring uniform concentration was followed. Hot working the disks to 50% of their original thickness and subsequent water quenching from 1423°K, produced no useful material after four attempts. This effort was not pursued further.

A fourth alloy with $X_{Si} = 0.25$ was personally prepared for conductivity measurements. The iron starter material was bought from Electronic Space Products with lot analysis showing 50 ppm Ni; 5 ppm Zn; 3 ppm Mg and Si; with the other five elements at less than 1 ppm.

Silicon from Research Inorganic Chemicals showed all four impurities at less than 1 ppm. Samples of both materails were X-ray analyzed to confirm their identity. The materials were handled in an Argon atmosphere glove box, where they were weighted, mixed and loaded into crucibles. The bulk material was melted in an atmosphere of cleaned argon by an induction coil which was made to slip around a quartz envelope. The crucible was suspended inside the envelope by a Molybdinum wire. The temperature was monitored

by an optical pyrometer which viewed the visible portion of the melt. The induction coil was made of copper tubing within which water was circulated to keep the coil from melting. Cleanliness was insured at all stages by following accepted laboratory practices.

The following procedure evolved. Polycrystaline alumina ($Al_2O_3$) crucibles from Aremco Products Incorporated and later higher purity recrystalized alumina crucibles from Coors Porcelain Company were used in the form of cylinders with tapered bottoms in the shape of a cone. The crucibles are commonly used to grow single crystals of high melting point metals. The taper and long cylinder encourage growth in the vertical direction when a temperature gradient is maintained and slowly moved with respect to the crucible so that solidification starts at the bottom. The solidified FeSi consistently showed that a reaction seemed to be taking place at the crucible/melt interface. A white material solidified on the quartz envelope as a result of the outgassing of the melt. The outgassing material was identified as $SiO_2$ by X-ray analysis. Since the only source of oxygen inside the system was in the form of $Al_2O_3$, a literature search revealed that a chemical reaction can sometimes take place. The reaction starts by the FeSi melt in contact with $Al_2O_3$ forming an obscure tertiary phase that does not stay stable. The end result is the formation of excess oxygen as $SiO_2$ is formed and Al enters the melt. Needless to say, another crucible material was found.

Hot pressed Boron Nitride powder, which is an excellent crucible material, is physically soft (not much harder than chalk)

and tends to absorb moisture from the atmosphere. A long tapered crucible was fashioned out of a 1 inch diameter Boron Nitride rod by slowly drilling a 3/4 inch diameter, 5 inch deep hole by an altered drill bit. The crucible was then cleaned, and preliminarily baked out before loading it with iron and silicon. The loaded crucible was then subjected to 24 hours of vacuum at $2 \times 10^{-6}$ microns inside the quartz envelope of the induction apparatus. It was then baked at about 300°C for another 24 hours or until the vacuum settled back to $2 \times 10^{-6}$ microns for a least 2 hours. This ensured that water and any other volatile cleaning agents were completely removed from the hydroscopic Boron Nitride. The envelope was back filled with purified argon back up to 1 atmosphere in order to ensure that no outgassing of Fe or Si occurred at the melt temperatures (Hultgren, et al, 1973). The temperature was gradually raised until the whole charge was melted at 1790°K. At that temperature, viewing the side of the crucible showed a maximum temperature gradient of 100°K from the top of the melt down to the point of the taper. The temperature of the melt was then reduced by 100°K ensuring that the temperature at the taper end was still above the solidification curve at 1548°K. The induction coil was mounted on a set of rails with a mechanism that could move the coil smoothly at low constant rates. The coil was raised at a rate of 3/4 of an inch an hour. No single crystals were grown. However, the resulting single phase was homogeneous and had a lower initial resistivity than any of the other concentrations. How the ingots were analyzed is discussed in the next

section. The concentration was chosen to be $X_{si} = 0.25$.

The ingots were then homoginized at 1425°K (about 120°K below the melting point) for 24 hours in a Brew Furnace under a vacuum of $10^{-3}$ microns. This was done to eliminate concentration gradients. An estimate of the diffusion of Si and Fe in the $X_{si} = 0.25$ alloy was made in order to choose a proper time interval for homogenization. Lai and Borg (1968a, 1968b) measured the diffussion constants of both elements in dilute alloys of FeSi at high temperatures. The estimates made here are crude because the diffussion coefficients were measured at significantly lower silicon concentrations. The diffussion coefficients at approximately 1425°K for Fe are $7 \times 10^{-9} cm^2/sec$ at $X_{si} = 0.047$ and $1.2 \times 10^{-8} cm^2/sec$ at $X_{si} = 0.117$ and for Si are $9 \times 10^{-9} cm^2/sec$ at $X_{si} = 0.005$ and $1.1 \times 10^{-8} cm^2/sec$ at $X_{si} = 0.042$. Extrapolating to $X_{si} = 0.25$ at the same temperature gives roughly $2.2 \times 10^{-8} cm^2/sec$ for both iron and silicon. Assuming a random process, the mean distance $\bar{X}$ is given as $\bar{X}^2 = 2Dt$ where D is the diffussion constant and t is the time in seconds. In one hour, the mean distance traveled by an atom is about 0.12 cm. This is probaly more than sufficient to equilibrate the concentration distribution because only concentration gradients need be compensated for. Twenty four hours was used to give plenty of margin. This time interval is also in agreement with others (Gupta, et al, 1964; Koster and Godecke, 1968; Ettwig and Pepperhoff, 1972; and Inden and Pitsch, 1972). At this pressure, it takes a temperature of about 1610°K to drive off iron and 1687°K to drive off silicon (Hultgren, et al, 1973). The material was then cooled before exposure to the atmosphere.

The conductivity samples were made 2.5 cm (or more) in length, 3 to 4 mm wide and 0.3 to 0.4 mm thick. The reasoning for the dimensions will be discussed later. Each sample was roughly shaped by the spark cutter and the final width and thickness lapped flat and parallel to an accuracy of a fraction of one percent. Each sample was held in place with pitch in a groove cut out of a large brass cylinder. The brass cylinder and sample were heated to 150°C on a thermostat controlled hot plate and pitch was allowed to melt and flow into the groove. After cooling, the cylinder could be handled easily and placed on an optical lapping machine. Both the holder and sample were then lapped. Once one of the two opposing faces was made flat, it was then easy to lap the other face flat and parallel, providing that the bottom of the groove and the face of the holder stayed parallel. If everything went well, a sample could be machined in three to five days. The pitch was easily removed by acetone and the sample measured. About ten readings of each width edge were taken on an optical comparator with an accuracy of $\pm 5$ microns. At least twenty readings of the thickness were taken on a Baush and Lomb DR25C optical gauge capable of an accuracy of 0.00025 mm. The mounting of both types of samples shall be described in another chapter.

## 4.4 SAMPLE CHARACTERIZATION

Each concentration was analyzed by metallography, X-ray diffraction and X-ray fluorescence techniques. The density and sound velocities were measured to characterize the samples. Initial state conductivity measurements shall be discussed in the next chapter.

Samples of each concentration were mounted, lapped and etched for microphotographs. Final lapping was done with 1 micron diamond plus oil on silk. Nital (nitric acid and alcohol) in various concentrations and time durations proved to be a good etching agent. Figure 4.2 through 4.9 show the grain sizes of each type of sample. Regular, single phase grains are seen in the 4%, 10%, and 14.3% by weight ($X_{si}$ = 0.077, 0.181, and 0.25) concentrations. The black dots seen randomly scattered in pictures for $X_{si}$ = 0.077 and $X_{si}$ = .342 (20.7% by weight) proved to be minute pits when the samples were viewed with light incident at a grazing angle (the same area was viewed with light incident nearly normal to and nearly parallel to the plane of the sample). The light was seen to be scattered out of the small voids while the rest of the surface remained dark. Figure 4.3 shows the grains of $X_{si}$ = 0.181 highlighted when viewed with nearly cross polarized light. Figure 4.4 and 4.5 show the same area of a sample of $X_{si}$ = 0.342. Figure 4.4 appears to have intermingling phases on a grey background. When viewed with nearly cross polarized light (Fig 4.5), the intermingling seems to disappear. Instead various "patches" are seen with different shades of grey. Each "patch" of a similar structure represents one crystaline orientation of one phase. At least two and possibly three phases are present. The dark grey boundaries near the center of Figure 4.2 proved to be deeper and wider erosion of the actual grain boundaries of $X_{si}$ = 0.077 when viewed with high magnification (Fig 4.7). Homogenized samples of $X_{si}$ = 0.25 showed a lot more ordering of grain boundaries than

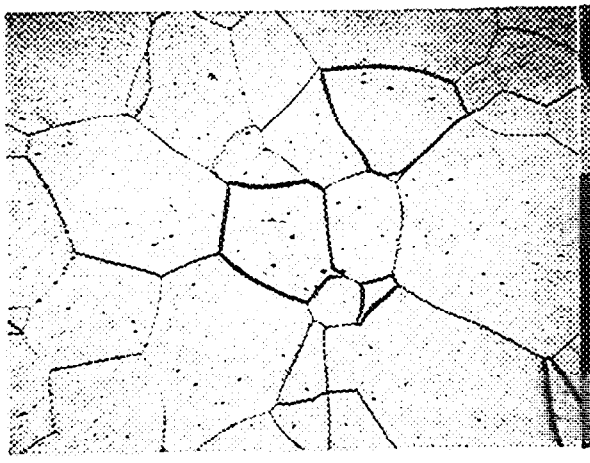

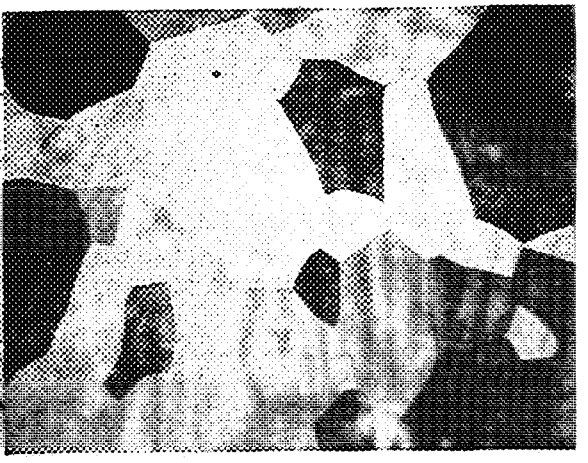

FIGURE 4.2 $X_{si}$ = 0.077, 20X

FIGURE 4.3 $X_{si}$ = 0.181, 20X

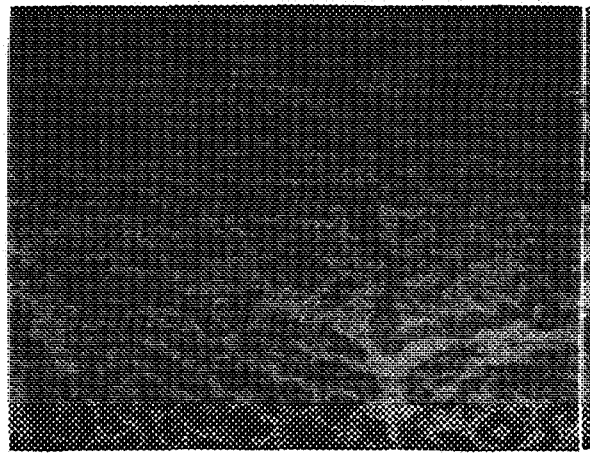

FIGURE 4.4 $X_{si}$ = 0.342, 200X

FIGURE 4.5 $X_{si}$ = 0.342, 200X
VIEWED WITH POLARIZED LIGHT

the original ingots (Fig 4.8 and 4.9). This may help explain the reason why no single crystals were grown. It seems that the motion of the melt caused by the induction process above the solified portion of the ingot prevented the formation of an ordered structure.

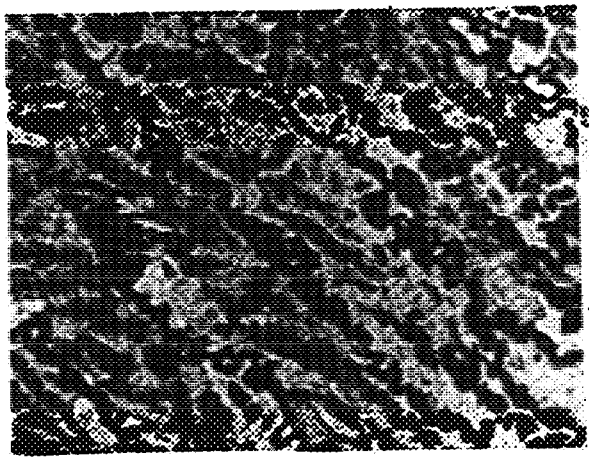

FIGURE 4.6 $X_{si}$ = 0.342, 20X

SHOWING RANDOM PHASES

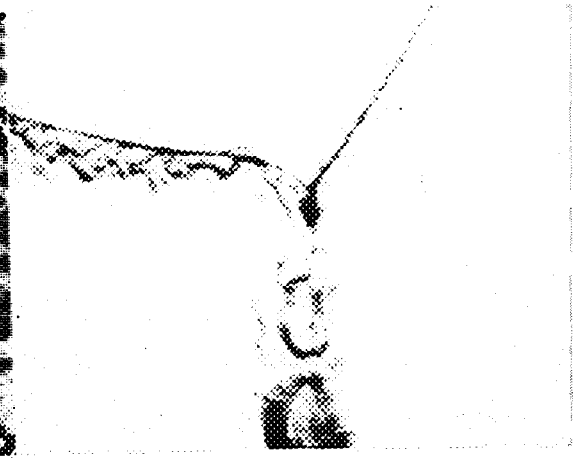

FIGURE 4.7 $X_{si}$ = 0.077, 2000X

DETAIL OF GRAIN BOUNDARIES

FIGURE 4.8 $X_{si}$ = 0.25, 128X

BEFORE HOMOGENIZATION

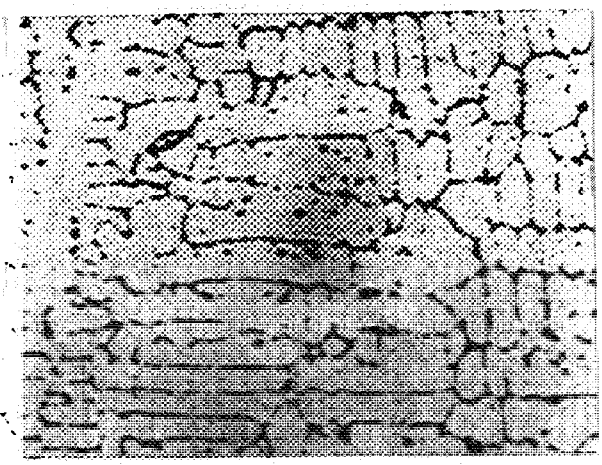

FIGURE 4.9 $X_{si}$ = 0.25, 64X

AFTER HOMOGENIZATION

Comparison of the microphotographs of the four compositions with the phase diagram reveals the following. Concentration $X_{si}$ = 0.077 is identified as single phased with the $\gamma$ phase being missed entirely. Concentration $X_{si}$ = 0.181 can be either the disordered

phase $\alpha$ or a combination of the ordered phases $\alpha_1$ and $\alpha_2$ and the disordered phase $\alpha$. Concentration $X_{si} = 0.25$ can be a only a mixture of the two ordered phases, $\alpha_1$ and $\alpha_2$. Concentration $X_{si} = 0.342$ is the most complicated, with the possibility of $\alpha_1$, $\alpha_2$, $\eta$, and $\epsilon$ phases being present.

X-ray diffraction analysis of the $X_{si} = 0.25$ alloy identified that only $\alpha_2$ was present by determining the bcc lattice spacing to be 5.635Å. Only the lattice symmetry of hcp $\eta$ phase with its lattice constants was positively identified for the $X_{si} = 0.342$ alloy. Sufficient intensity was seen for $\alpha_1$ or $\alpha_2$ to be present in substantial quantity but the lattice spacings could not be accurately determined. This strongly implies a berthollide structure and rules out phases $\beta$ or $\epsilon$ as a major constituent of the alloy. These results together with the phase diagram identify the only plausible phases to be present in the $X_{si} = 0.342$ alloy as $\alpha_1$, $\alpha_2$, and $\eta$. Another argument against $\epsilon$ phase being present instead of $\alpha_1$ or $\alpha_2$ in substantial quantity is based upon the measured density of this concentration. The ideal crystal densities of $\eta$ and $\epsilon$ phases are 6.5055 and 6.1626 $gm/cm^3$ respectively. For the overall measured density of 6.770 $gm/cm^3$ to be this value, and with a large quantity of $\eta$ phase present, $\epsilon$ phase is estimated to be possibly present in no more than a few percent. This is not expected to affect the EOS experimental results because the bulk properties at high pressures depend on the mean atomic number, rather than the initial crystal structure. This is especially the case here because of the small and random grain size.

The effect of the initial states on the conductivity measurements will be discussed in the next chapter.

The density of samples of each composition were determined by the displacement method of purified distilled water. The weight of each sample in air and in the water was taken by an analytical balance with an accuracy of $\pm 0.00005$ gm. Each sample was allowed to come to thermal equilibrium in a temperature controlled room. The water temperature was measured to an accuracy of $\pm 0.1°C$. Both sources of error were negligible in comparison with the variation in density from sample to sample. The densities are shown in Table 4.2. The variation of density with composition is shown in Figure 4.10. The ideal density of pure iron, and density data from Balchan and Cowan (1966), Kormer and Funtikov (1965), and Zukas (et al, 1963) are also shown in Figure 4.10. The experimental data from these authors does not specify the uncertainties in density or composition with the exception of one data point (Kormer and Funtikov, 1965) where only the variation in density is given. The chemical analysis of the FeSi alloys was checked against an independent determination of Si concentration using an X-ray fluorescence technique. The Si $K_\alpha$ emission intensities were measured with a mask (large with respect to grain size) to ensure that the analyzer viewed the same surface area for each specimen. The Si concentration was calculated relative to the $X_{si} = 0.25$ sample, which was assumed to be known most accurately. Due to a large background around the $K_\alpha$ line, only the $X_{si} = 0.181$ and $X_{si} = 0.342$ are considered accurate to $\pm 0.005$. The relative

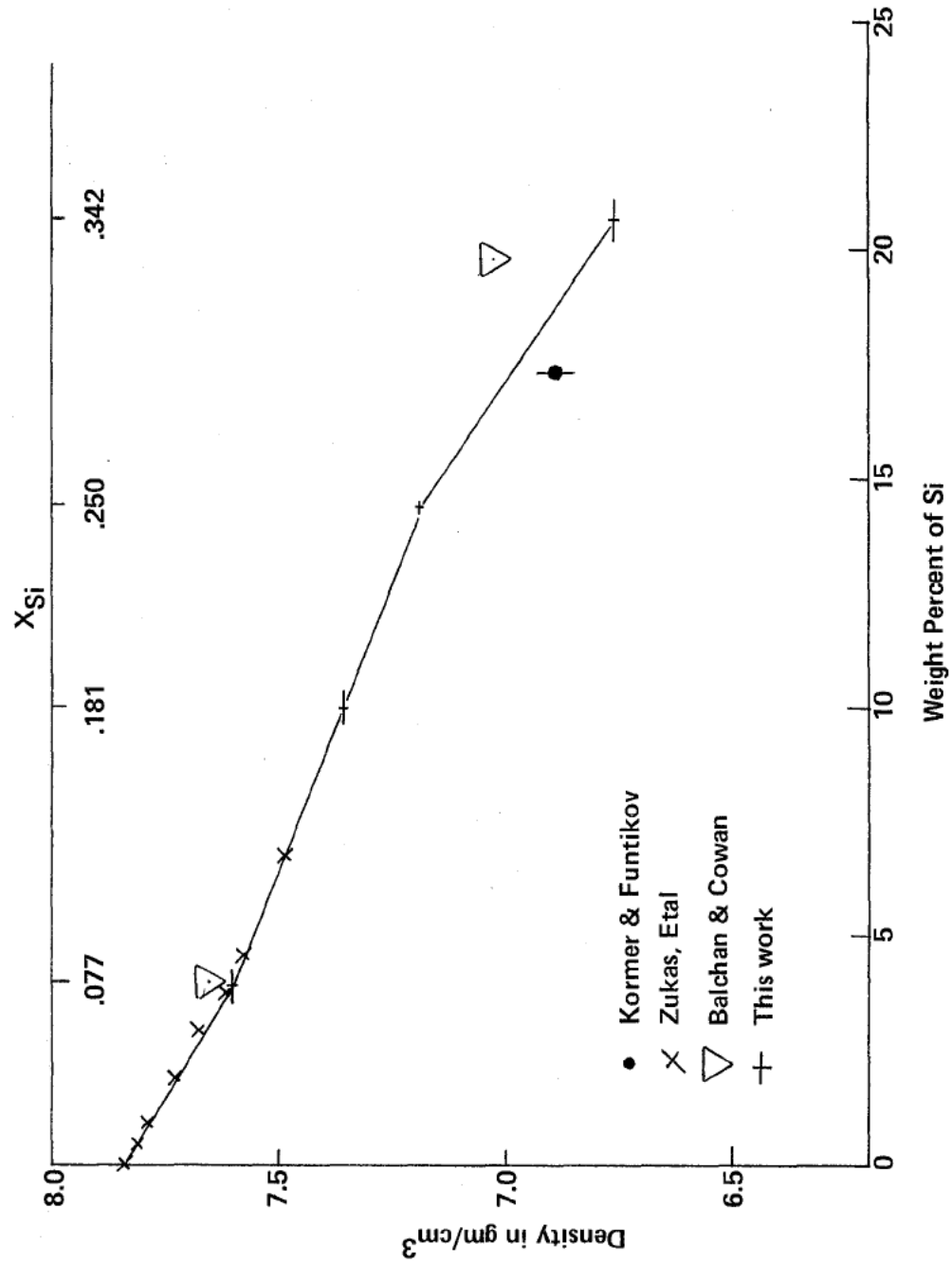


FIGURE 4.10 FeSi DENSITY AS A FUNCTION OF COMPOSITION

error in the $X_{si}$ = 0.077 is estimated at $\pm$0.01. The two methods agree for all three concentrations. The only traces of elements encountered were Cl, K, and Ca. This is most probably due to handling of the specimen and not cleaning it before the X-ray fluorescence was made. Finally, the Silicon concentration was determined by gravimetrical analysis to an accuracy of $\pm$0.003. The concentrations are $X_{si}$ = 0.077, 0.181, 0.250, and 0.342. There is good agreement with the data from Zukas, et al.

The only data point that seriously departs from the pattern is the 19.7% Si by weight point given by Balchan and Cowan. The authors prepared their samples by arc melting and subsequent homogenization at 750°C for 48 hours and furnace cooling. Examination of the phase diagram reveals that phase $\eta$ ($Fe_5Si_3$) is metastable below 825°C. The homogenization process would certainly encourage the decomposition of the $\eta$ phase to $\alpha_1$ and $\epsilon$ phases. Perhaps their samples contained an appreciable amount of $\epsilon$ phase that they did not identify. Their X-ray diffraction analysis claimed only "$Fe_3Si$" ($\alpha_1$) and $Fe_5Si_3$ ($\eta$) phases present at odds with the homogenization procedure. Further, correcting the density due to 0.4% W impurity (introduced by the electrodes in arc melting) changes it from 7.016 to 6.940 g/cm$^3$, which does not account for most of the discrepancy in density at the claimed concentration. The density of the Kormer and Funtikov sample was also corrected for the 1.1% carbon impurity.

The longitudinal and transverse sound velocities were measured to $\pm$3% accuracy by a standard technique (Truell, et al, 1969).

X- and Y-cut quartz transducers were used to generate the sound waves. The seismic parameter $\phi$ (also referred to as the bulk sound speed) was calculated according to equation 2.9 and is given in Table 4.2. (Fe data is also given for comparison). The density, sound velocity and average molecular weight (also given in Table 4.2) will be used together with the thermodynamic and physical properties in subsequent EOS calculations.

From the above sample concentration characterization and the phase diagram it is safe to say that, for $X_{Si}$ = 0.077, 0.181, and 0.25 the initial states are ferromagnetic. Of all the possible phases present in samples of $X_{Si}$ = 0.342, only the $\epsilon$ phase is not ferromagnetic. Furthermore, from the dependence of the Curie temperature on Silicon concentration it can also be concluded that the permeabilities of the different concentration samples are different. The observed demagnetization during the experiments confirmed the fact that all the initial states had permeabilities characteristic of ferromagnetic phases.

## 5.0 ELECTRICAL CONDUCTIVITY

The results of previously reported measurements of electrical conductivity of FeSi alloys are summarized. Current methods of extrapolating conductivity to the Earth's core including predicted behavior as a function of concentration, temperature and pressure are reviewed. The measurement of initial conductivity of FeSi alloy samples is described.

TABLE 4.2

PHYSICAL PROPERTIES OF FeSi ALLOYS

$X_{si}$ CONCENTRATION

| QUANTITY | 0 | 0.077 | 0.181 | 0.250 | 0.342 | REMARKS |
|---|---|---|---|---|---|---|
| % Si by Wt | 0 | 4.0 ±0.3 | 10.0 ± 0.3 | 14.26 ± 0.02 | 20.7 ± 0.3 | |
| $\rho$ (g/cm$^3$) | 7.85 (1) | 7.606 ± .010 | 7.354 ± .005 | 7.183 ± .005 | 6.770 ± .005 | (1) AIP Handbook 1972 |
| $\phi$ X $10^{-5}$ (cm/sec) | 4.64 (2) | 4.73 ± .14 | 4.80 ± .14 | 4.83 (3) | 4.87 ± .15 | (2) Calculated |
| $\overline{M}$ | 55.847 (1) | 52.68 (4) | 50.03 (4) | 48.907 (4) | 46.45 (4) | (3) Data Interpolated |
| $\alpha$ X $10^6$ (1/deg C) | 11.7 (1) | 11.93 (3) | 12.16 (3) | 12.3 (5) | 14.39 (3) | (4) Calculated |
| $C_p$ at 298°K | 5.97 (6) | 5.92 (3) | 5.90 (3) | 5.87 (6) | 5.75 (3) | (5) Kalishevich<br>(6) Hultgren |

## 5.1 PREVIOUS MEASUREMENTS

Only a small amount of work on the measurement of electrical conductivity of FeSi alloys has been reported in the literature. The most recent work investigated the electrical behavior of solid solutions of FeSi, $X_{si} = 0.008$ to $X_{si} = 0.058$, at temperatures from 300°K to 1300°K at 1 atmosphere and compared it to that of pure iron (Zinovev, et al, 1973). The influence of silicon (as an impurity) upon the various electron scattering mechanisms at high temperatures were found to qualitatively agree with a disordered spin model and disagree with the Mott s-d model. The above concentrations were chosen because Si does not contribute to the magnetic properties of Fe while significantly decreasing the conductivity without changing the lattice appreciably. At the lowest concentration, they found that above the Curie temperature, the conductivity of the FeSi alloy became larger than that of Fe in disagreement with the Mott s-d model. Mathiessen's Rule states that the total electrical resistivity is given by

$$\rho_e = \rho_i + \rho_l + \rho_m \tag{5.1}$$

where $\rho_e$, $\rho_i$, $\rho_l$ and $\rho_m$ are respectively, the total, residual (impurity), lattice and magnetic components of resistivity. Zinovev and his co-workers reported that they found that the separate contributions interact with each other and cannot be added. They also reported that the change of resistivity with temperature became essentially constant for different Si concen-

trations above the Curie temperature. This shows that the impurity atoms affect the magnetic contribution to resistivity much more than the lattice contribution below the Curie temperature.

The measurements imply that the initial conductivity of the FeSi samples are not simply correlatable with the various components of conductivity.

It is nevertheless interesting to qualitatively speculate upon the effect of various contributions to the resistivity both in the initial state (at 1 atmosphere and room temperature) and in the shocked state (at pressures between 500 and 1400 Kbars and elevated temperatures). In the initial state the impurity effects not only contribute directly but also affect the magnetic contribution to the resistivity. Therefore, a smaller number of residual impurities should result in a lower resistivity.

In a shocked, non-magnetic state, only the lattice contribution is temperature dependent. Therefore the resistivities should be dependent upon the total number of Silicon atoms and their contribution to the electron scattering by lattice vibration.

Another interesting set of observations has been reported on the conductivity of (concentrated) FeSi alloys in the 800 to 1700°C range at 1 atmosphere (Baum, et al, 1967). Close to the melting temperature, $\partial \sigma / \partial T$ became positive in contrast with iron which has a negative slope. For the applicable concentrations used ($X_{si} = 0.25$ and $X_{si} = 0.375$), no discontinuous change in conductivity was observed upon melting. In the melt, the slope ( $\partial \sigma / \partial T$ ) was zero for $X_{si} = 0.25$ and slightly positive (or the order of a few percent) for $X_{si} = 0.375$,

in contrast to the slope for pure iron (which is negative). The authors suggest that the covalent bond between Fe and Si in the solid is broken at high temperatures, releasing the bound (iron) electrons and increasing the conductivity. The effects of temperature and impurities on conductivity are seen as non additive factors. The conductivity of $X_{Si} = 0.25$ was measured to be 5.65 X $10^3$ mho/cm from T = 1530°K to T = 1973°K in the melt.

The only measurements of the effect of pressure upon the electrical conductivity of FeSi alloys that were found were done by Bridgeman in 1957 at static pressures up to 100 Kbars (Bridgeman, 1964). Incidently, the early pressure standards used in the static experiments were revised downward twice due to better instrumentation and correction factors due to pressure effects. The concentrations investigated were $X_{Si} = 0.0039$ to 0.0575 with only two samples (at $X_{Si} = 0.0078$ and $X_{Si} = 0.0195$) uniform enough to make direct measurements of conductivity. Therefore, only qualitative correlation is expected with the present effort. The significant finding was that Si decreases the effect of pressure on conductivity. It is not known what the impurity effect on the slope will be in the pressure range of 500 to 1400 Kbars.

At this point it is relevant to review the only two known high pressure measurements of conductivity of pure Fe in anticipation of similar behavior of FeSi alloys at low Si concentrations.

Keeler and Mitchell (Keeler and Mitchell, 1969; and Keeler, et al, 1971) have directly measured the conductivity of Fe by monitoring the change in resistance in the pressure range from 50 to

1400 Kbars. Flat, thin samples of rectangular cross sections were used in the shock experiments instead of the flattened wires previously used both in static and dynamic pressure experiments (Bridgeman, 1952; Fuller and Price, 1962). The measured change in voltage across the sample, together with the EOS, was converted to an absolute resistivity measurement of Fe behind the (plane wave) shock front.

Large demagnetization pulses were observed in addition to the anticipated change in conductivity above 130 Kbars. This was dramatic evidence that the high pressure phase of Fe is non-magnetic. Measurements on copper (Keeler, et al, 1971) did not show a negative pulse. Below 200 Kbars, the bcc to hcp transition was slow enough to be seen on a Techtronix 585 oscilloscope (which had a rise time of less than 5 ns). The numerical results are discussed in Section 7.

Royce (Royce, 1970; Keeler, et al, 1971) studied the shock demagnetization of Fe between 160 and 1200 Kbars by using a magnetic circuit and a pickup coil to measure the change in the magnetic flux. The demagnetization observed between 160 to 220 Kbars was not quite complete, in agreement with pressure-volume Hugoniot data which shows a two phase region (below the Rayleigh line). Above this pressure the experiments show complete shock-induced demagnetization. The time constant of the decay of the demagnetization pulse was found to be proportional to the conductivity of the shocked sample and the square of the sample thickness. Sufficient experiments were done at four separate

pressures to verify the predicted quadratic variation with thickness. The observed decay was in fact due to eddy current decay. The decay times were observed to be 30 nanoseconds at about 180 Kbars and shorter at higher pressures. Between 130 and 200 Kbars, the derived electrical conductivity was found to agree with the static data (Balchan and Drickamer, 1961). Below the phase transition, static and dynamic methods did not agree. The agreement between the two dynamic methods was very good at all pressures.

## 5.2 THEORETICAL PREDICTIONS

Two types of calculations are widely used in the literature to predict the conductivity of the Earth's core. The first depends upon a "nearly" free electron model of liquid metals and alloys (Dreirach, et al, 1972). The electron scattering is numerically calculated by evaluating the phase shifts due to periodic potentials. The potential of a single atom must be known in sufficient detail to describe electron scattering by one atom. Reasonable agreement with experimental data at 1 atm has been obtained in some cases. Iron Germanium has curious properties (experimentally observed) that cannot be explained by their theory: The conductivity of FeGe alloys decreased by only a few percent on melting. This observation is similar to the FeSi alloys reveiwed in the last section.

The extrapolation of the conductivity of liquid iron at atmospheric pressure has been carried out by Evans and Jain (1972). The pressure dependence is estimated by a hard sphere model while the temperature dependence is obtained from a 0 to 40 Kbar melting

curve of iron (Higgins and Kennedy, 1971). The impurity (alloying) effect is included by using 1 atmosphere liquid alloy conductivity measurements.

The interesting prediction of this theoretical treatment is that the alloying dependence of resistivity is much the same for liquid alloys at normal and very high pressures. For liquid iron, the theory predicts an increase in conductivity with temperature and pressure. The calculated Earth's core conductivity, based on this theory, is between $1 \times 10^4$ and $5 \times 10^3$ mho/cm (Jain and Evans, 1972).

The second theoretical approach uses the law of corresponding states to relate the reduced electrical conductivity to the reduced temperature (Gardiner and Stacey, 1971). This involves choosing a critical temperature of pure iron from a deduced range of temperatures (from 6,750°K to 10,000°K) and evaluating an empirical constant based on the initial slope of change in conductivity with temperature in the melt. The pressure dependence of conductivity is modeled after solids including the inverse proportionality to temperature. An approximation, which may not be valid, of $\alpha K =$ constant is used ( $\alpha$ is the coefficient of expansion and K is the bulk modulus). An empirical extrapolation of 1957 Bridgeman data on resistivities of iron alloys up to 100 Kbars is used to take the impurity factor into account. The predictions of the conductivity of the Earth's core include:

a. Practically no variation with pressure at constant concentration and temperature.

b. Inverse variation with temperature.

c. The total range of conductivities for the core is within $1 \times 10^4$ to $1.4 \times 10^3$ mho/cm.

In addition, Stacey (1972) concludes that the estimated conductivity of the core is 8 to 10 times greater than for pure iron at the same temperature and pressure. It will be interesting to see which aspects of the theoretical predictions will agree or disagree with the experimental measurements of FeSi alloy conductivities, keeping in mind that the shocked state will most likely still be in solid phase.

## 5.3 INITIAL CONDUCTIVITIES OF SAMPLES

The cut and lapped FeSi conductivity samples were enclosed in an insulating sandwich of Wesgo 995 alumina (polycrystaline $Al_2O_3$, Western Gold and Platinum Corporation, Belmont, California). Alumina was chosen for a number of reasons, the most important being its insulating properties and close shock impedance match to FeSi. The insulating properties of alumina have been measured at high pressures to be $\sigma = 7.9 \times 10^{-6}$ mho/cm at P = 420 Kbar and $\sigma = 1.57 \times 10^{-4}$ mho/cm at P = 1100 Kbar (Keeler, et al, 1971).

The alumina plates extended well beyond the dimensions of the conductivity sample, to avoid the effects of lateral rarefactions in the alumina. The bottom plate was nominally either 6.35 or 3.18 mm thick depending on the shock pressure while the top plate was always 6.35 mm thick. These dimensions were chosen to allow at least 0.5 $\mu$ sec time after the shock front to make the measurement before the release waves destroy the shocked state. The top plate had four

3.18 mm (nominal) circular holes cut out for the current and voltage probes. All alumina surfaces parallel to the shock front were fine ground to $\pm$ 0.0005 cm.

Indium was chosen for the current and voltage leads because of its very close shock impedance match to alumina and because it melts at low temperature (157°C). This choice of terminals minimized the possibility of shock induced shearing effects between the sample and the leads. See Fig 5.1 and 5.2 for the physical arrangement of the sandwich.

The remaining space between the alumina plates surrounding the FeSi sample was filled with thermo-setting polyethylene which also served to bind the sandwich together. A special fixture was made so that the extra polyethylene that was forced into the holes in the alumina could be removed and the terminals made while the sandwich was held rigidly at a temperature about 10°C higher than the melting point of Indium.

Aluminum flux was found to properly prepare the FeSi surface that was exposed by the holes in alumina. The outer two terminals were made first. The leads were extended by carefully inserting standard wires to a depth of not more than 2 mm into the Indium and the wires supported while the sandwich was allowed to cool to room temperature. Then the exposed inner two sample surfaces were cleaned with 5% phosphoric acid. Another fixture was made that allowed two spring loaded probes to be inserted into the inner two holes and make an electrical contact with the sample. Electrical

FIGURE 5.1 CONDUCTIVITY SANDWITCH

(Isometric drawing)

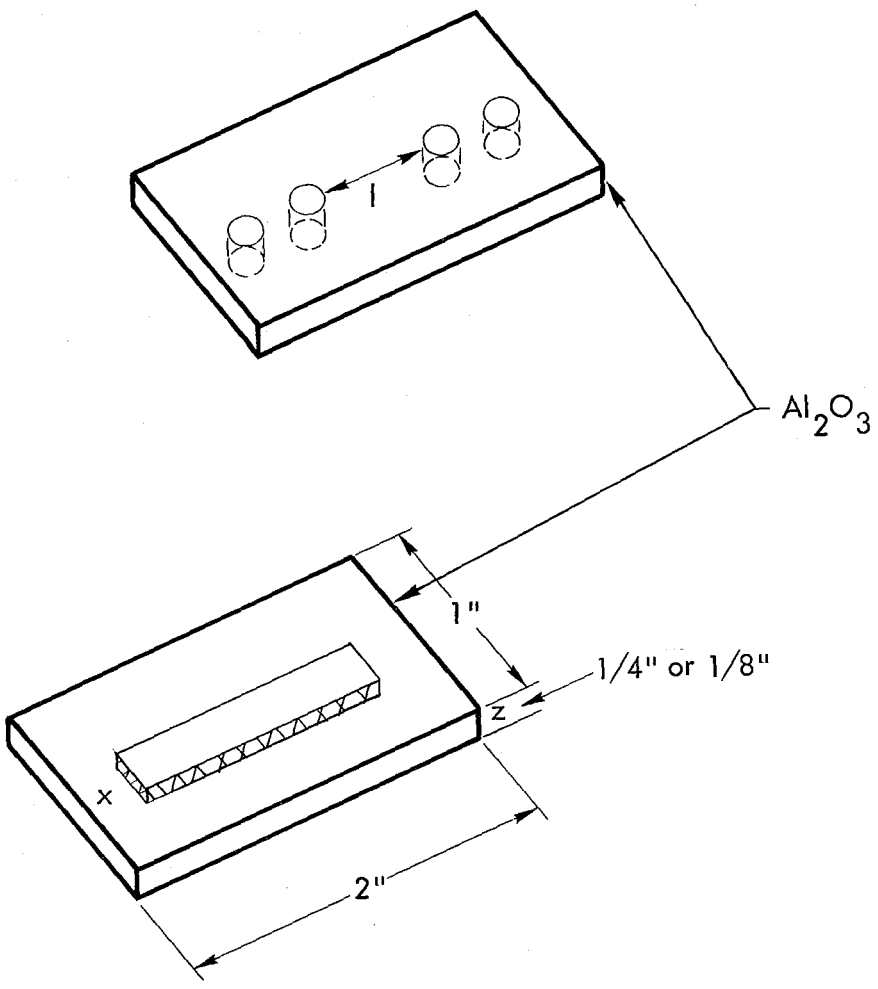


Conductivity sample
sandwiched in
alumina

terminals were provided such that no additional forces or torques were exerted on the sample while conductivity measurements were being made. The two probes were also mounted so that their lateral

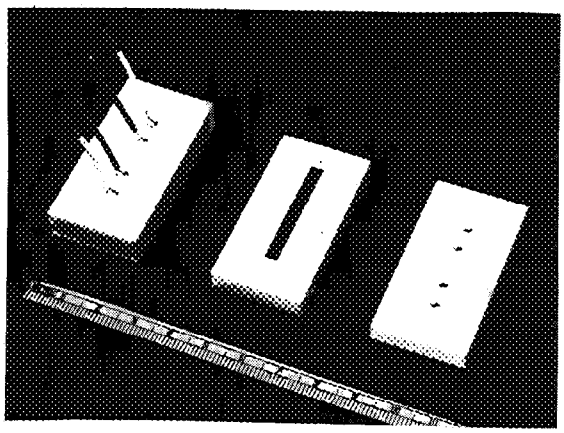

FIGURE 5.2 PARTIALLY ASSEMBLED CONDUCTIVITY SAMPLE

motion was severely restricted. A number of measurements was made of the separation of the two probes from the other side of the top alumina plate (before each sandwich was made). The accuracy of positioning of the two probes upon repeated mountings was better than 0.5%. The minimum distance between the inner two holes in the top alumina plate was also measured on the optical comparator.

The resistance of the samples, first with the probes and then with the Indium terminals, was measured at a constant 20°C temperature on a Precision Kelvin Bridge (Leeds and Northrop Company) in the standards laboratory of LLL. The difference in potential between the unknown and a standard resistance is nulled by adjusting the known resistance. The accuracy of this bridge is 0.04% down to $2.5 \times 10^{-5}$ ohm. Select values of the standard resistances were compared to secondary NBS resistance standards and found to be within their allowable tolerances.

The conductivity of a sample is given by

$$\sigma = \frac{L'}{RXZ} \tag{5.2}$$

where $L'$ is the distance between the probes, R is the measured resistance and X and Z are the dimensions of the cross section of the sample. The initial conductivities of the four concentrations are given in Table 5.1.

TABLE 5.1 INITIAL CONDUCTIVITIES AT 20°C

| $X_{si}$ | $\sigma$ X $10^{-4}$ mho/cm | Uncertainty |
|---|---|---|
| 0.077 | 1.664 ± 0.017 | 1.0% |
| 0.181 | 1.017 ± 0.020 | 1.9% |
| 0.250 | 2.313 ± 0.018 | 0.76% |
| 0.342 | 0.974 ± 0.026 | 2.6% |

The uncertainty in the conductivities is consistent with Fe measurements of samples 0.1 X 0.3 X 2.0 $cm^3$ where 2% was quoted (Arajs and Colvin, 1964).

Another measure of the resistance of each sample was done after the second set of Indium terminals was in place. The terminals were redone if the difference between the calculated distance between the terminals and the distance between the holes in the top plate differed by more than 6%. The error in the separation between the terminals was expected to be significantly reduced with the arrival of the shock front (discussed below).

A detailed Hugoniot study of polycrystaline aluminum oxide (alumina) was performed because of the technical uses of the material

(T. A. Ahrens, W. H. Gust and E. B. Royce, 1968). Measurements made on Wesgo 995 alumina revealed a precursor shock (elastic shock) with a very fast velocity of about 10 mm/micro sec (the actual velocity measurements revealed a range of velocities from 9.82 to 10.38 mm/micro sec) below 900 Kbars. Above 900 Kbars, only the normal deformation shock was seen.

Clear evidence that the Indium (which makes up the potential probes) fully fills the holes in the alumina cover has been seen in the iron conductivity experiments. Oscilloscope traces of the voltage for experiments below 900 Kbars show a definite dip of a constant voltage. The timing of the dip was positively identified as due to the arrival of the elastic precursor before the deformation shock wave.

The dimensions of the cross section and the accompanying distance between the holes in the top plate are given in Table 5.2 for each sample. The four terminals were then reinforced with epoxy on the outside of the top plate in order to provide mechanical support before each sandwich was put into an experimental assembly.

## 6.0 EXPERIMENT

Plane wave explosive systems, the Hugoniot experiments, the design of the electrical conductivity experiments, and the diagnostics used to record the experimental measurements are described. The capabilities and the limitations of the shock wave techniques used in this work are discussed.

TABLE 5.2 INITIAL STATE PARAMETERS FOR CONDUCTIVITY MEASUREMENTS

| SHOT | $X_{si}$ | R X $10^2$ OHMS | L mm | Z mm | X mm |
|---|---|---|---|---|---|
| 1 | .342 | 1.071 | 12.617 ± .019 | 0.4197 ± .00059 | 3.0354 ± .0100 |
| 1 | .342 | 1.663 | 12.584 ± .017 | 0.2955 ± .00083 | 2.8283 ± .0064 |
| 2 | .342 | 1.733 | 12.595 ± .004 | 0.2986 ± .0042 | 2.5167 ± .0061 |
| 2 | .077 | 0.7432 | 12.609 ± .007 | 0.3349 ± .0041 | 3.2003 ± .0050 |
| 3 | .181 | 0.1012 | 12.693 ± .004 | 0.4133 ± .0021 | 2.1693 ± .0041 |
| 3 | .077 | 0.8071 | 12.640 ± .002 | 0.3183 ± .0098 | 3.0860 ± .0069 |
| 4 | .077 | 0.5981 | 9.296 ± .002 | 0.3043 ± .0005 | 3.2160 ± .0096 |
| 4 | .181 | 0.7107 | 9.039 ± .005 | 0.3955 ± .0010 | 3.3026 ± .0100 |
| 5 | .250 | 0.3628 | 9.319 ± .004 | 0.3637 ± .0027 | 3.2297 ± .0020 |
| 5 | .342 | 1.39 | 12.609 ± .005 | 0.3545 ± .0018 | 2.5643 ± .0097 |
| 6 | .077 | 0.5015 | 9.188 ± .007 | 0.3618 ± .0017 | 3.1774 ± .0061 |
| 6 | .181 | 0.7018 | 9.030 ± .004 | 0.4130 ± .0014 | 3.1465 ± .0054 |
| 7 | .342 | 2.532 | 12.591 ± .004 | 0.2324 ± .0017 | 2.280 ± .0072 |
| 7 | .250 | 0.3709 | 9.289 ± .007 | 0.3601 ± .0019 | 3.1520 ± .0283 |
| 8 | .181 | 0.6996 | 9.110 ± .001 | 0.4025 ± .0013 | 3.274 ± .0032 |
| 8 | .342 | 1.052 | 9.370 ± .003 | 0.3397 ± .0023 | 2.827 ± .0122 |
| 9 | .077 | 0.5923 | 9.202 ± .008 | 0.3100 ± .0018 | 3.1814 ± .0036 |
| 9 | .250 | 0.4284 | 9.116 ± .005 | 0.3042 ± .0008 | 3.1348 ± .0044 |
| 10 | .181* | 0.7154 | 9.205 ± .012 | 0.4202 ± .0018 | 3.1453 ± .0024 |
| 10 | .250* | 0.3623 | 9.429 ± .017 | 0.2937 ± .0029 | 3.9382 ± .0049 |
| 11 | .250 | 0.3068 | 9.439 ± .001 | 0.3516 ± .0054 | 3.9358 ± .0067 |
| 11 | .250* | 0.3564 | 9.428 ± .008 | 0.3095 ± .0016 | 3.9270 ± .0037 |

*On-Hugoniot samples

## 6.1 SHOCK WAVES

A planar shock wave for a dynamic high pressure experiment was achieved using a detonator, plane wave lens and a high explosive cylinder. The key to achieving a one-dimensional planar shock front is a Snell's Law plane wave lens. The outer cone of this device is made of a high velocity explosive while the inner cone is made of a slower velocity explosive as shown in Figure 6.1.

After detonation takes place at a single point at the apex of the outer cone, the velocity $D_1$ of the high explosive detonation sets off the detonation of the explosive of the inner cone in such a way that the two detonations keep pace with each other at their interface. This is achieved by choosing the angle $\theta$ so that $D_1 \sin\theta = D_2$. This results in a shock planarity which is within 30 nanosec across a diameter up to 30 cm. The planar shock wave is further enhanced within the main high explosive cylindrical charge (Keeler, et al, 1971). For pressures up to about 500 Kbars a direct contact was made with the experimental base plate. For pressures up to 1500 Kbars, a flyer plate was used between the explosive and the base plate (Figure 6.2). During the flyer plate free flight of about 2.4 cm, the plate is accelerated by repeated rarefactions and shock waves with the explosive reaction products. A high pressure shock is generated at the impact interface of the flyer plate and the base plate and travels into both the flyer and base plate.

FIGURE 6.1 PLANE WAVE LENS

FIGURE 6.2 CONTACT AND FLYING PLATE ARRANGEMENT

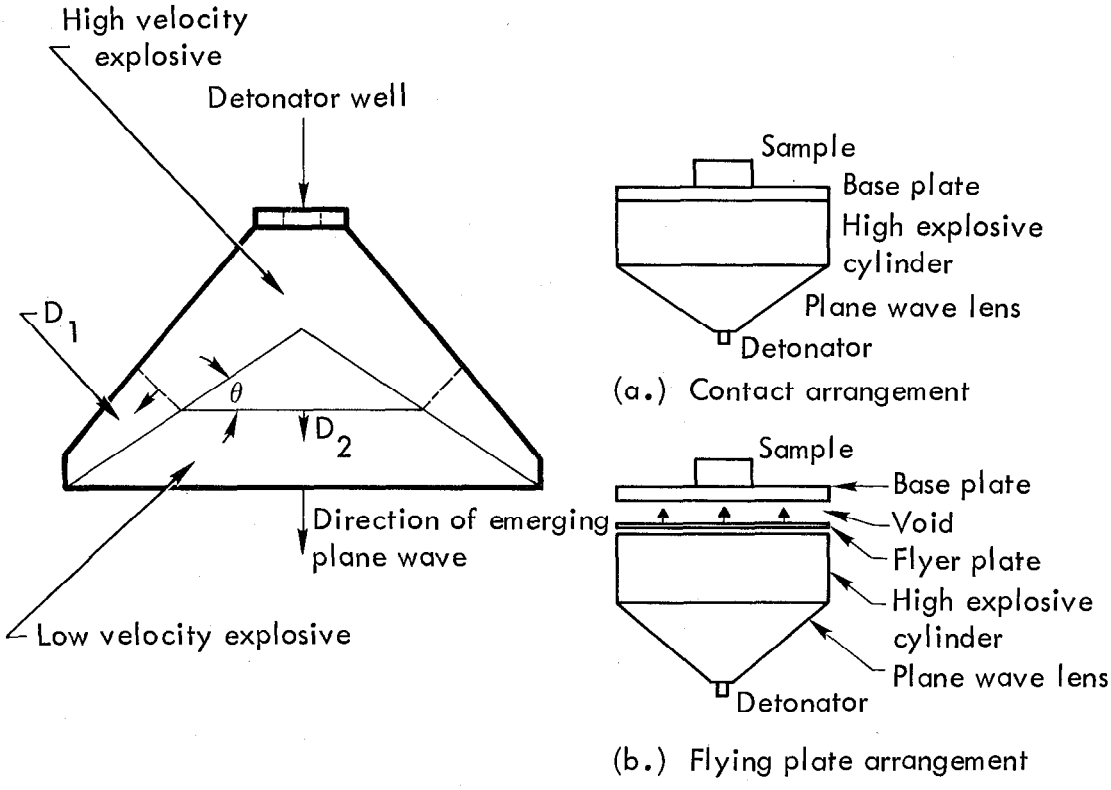


The pressures and velocities which can be achieved in specific base plates have been tabulated for various explosives and flyer plates (Gust, 1966). This allows estimates to be made for each experiment in the placement of timing devices and the speeds of the recording instruments. The greatest uncertainty comes from the exact thickness of the flyer plate. The variations in density of

the pressed explosives are minimized by careful processing and X-ray inspections for anomalies. A carefully machined and assembled experiment will usually perform within 10% of the tabulated pressure. It is therefore extremely important to independently measure the pressure in a standard impedance sample in each experiment. A sufficient number of sensors must also be used to measure any deviations from planarity ("tilt"). The nominal pressure systems used are given in Table 6.1.

TABLE 6.1

HIGH EXPLOSIVE SHOCK WAVE GENERATING SYSTEMS

FOR CONDUCTIVITY EXPERIMENTS

| LENS DIAMETER INCHES | H.E. SYSTEM | H. E. WEIGHT LBS | BREAKOUT FROM DETONATION MICROSEC | EXPECTED PRESSURE IN ALUMINUM KBARS |
|---|---|---|---|---|
| 8 | 4" thick 9404; 1/2" Al Base Plate | 26 | 35 | 366 |
| 12 | 6" thick TNT, 1/8" airgap, 1/8" Monel Flyer, 1" airgap, 3/16" Al Base Plate | 65 | 60 | 565 to 650 |
| 12 | 6" thick 9404, 1/8" airgap, 1/8" Monel Flyer, 1" airgap, 3/16" Al Base Plate | 66 | 55 | 780 |
| 12 | 6' thick 9404, 1/8" airgap, 1/16" Monel Flyer, 1" airgap, No Base Plate | 66 | 54 | 1100 |

## 6.2 DESIGN OF CONDUCTIVITY EXPERIMENTS

The base plate of all conductivity experiments was made of an aluminum alloy (2024 aluminum) nominally 0.418 cm thick. This material is one of the most extensively used materials in shock wave physics and it is easily machinable. All flyer plate experiments used monel, another well known alloy. The flyer thickness was nominally 0.312 cm and was held in place 2.54 cm away from the base plate by a spacer ring. Figure 6.3 is a drawing of the sample holder used to position the electrical self shorting pins, the sandwiched conductivity samples and the impedance standards. This housing was bolted to the base plate. Figures 6.4 and 6.5 show a partially assembled experiment with coaxial electrical leads connected to a few of the self shorting pins. The free surface pins (three each; five sets used) were epoxyed in at three different levels above the base plate. Sufficient aluminum was removed around these pins above the base plate to prevent interference with the free surface velocity measurements of the base plate. The distances between the three levels were chosen to provide time intervals of about 0.4 microseconds. The height of each pin was carefully measured with respect to a reference surface, since only the height differences were used in calculating the free surface velocities. The final measurements were made, after the pins were expoxyed, using a Bauch and Lomb DR25C optical gauge capable of an accuracy of 0.00025 mm.

The square and round holes in the sample holder were used for the impedance standards which were placed on top of the base plate.

FIGURE 6.3 LAYOUT OF SAMPLE HOLDER

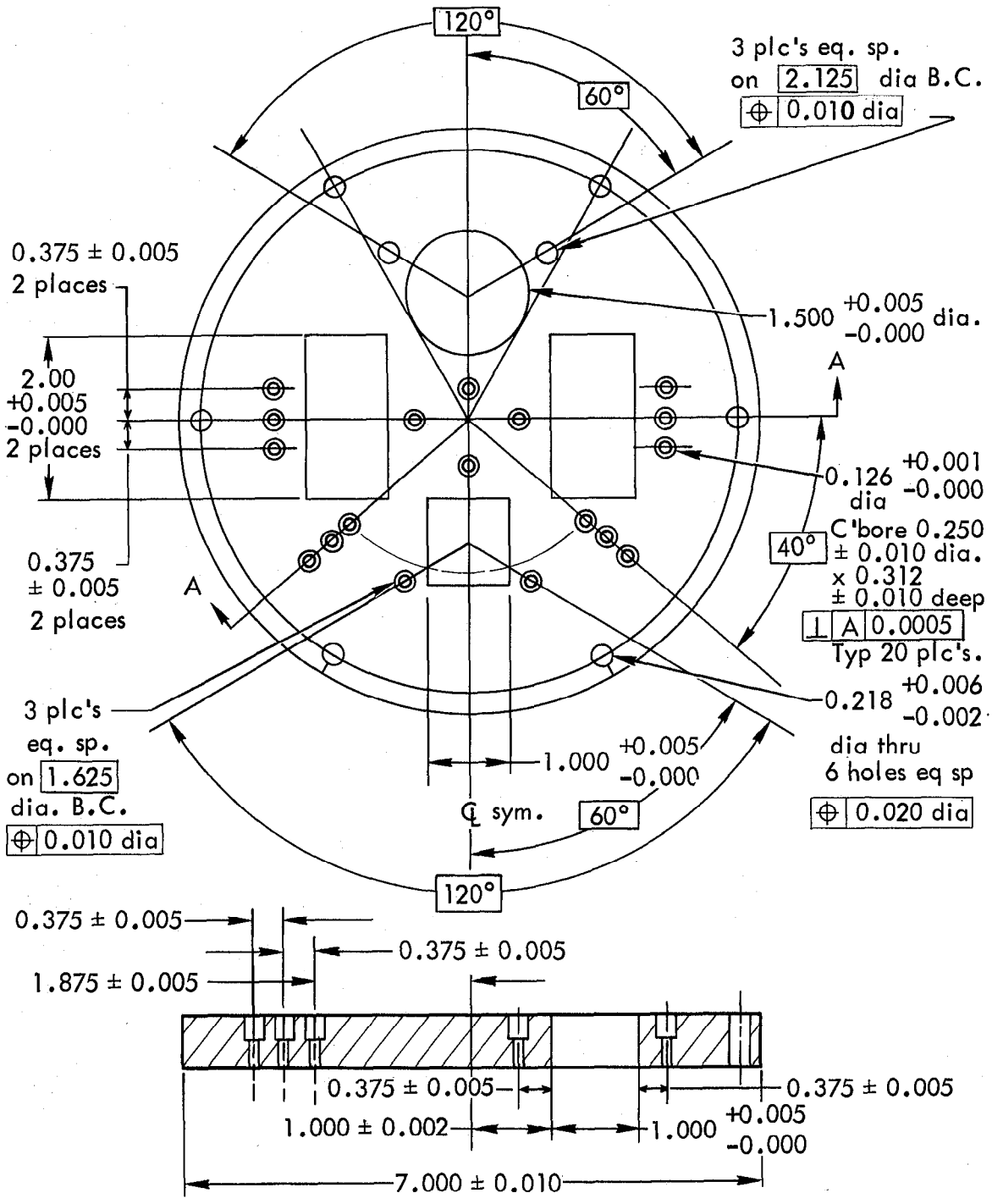


Section AA

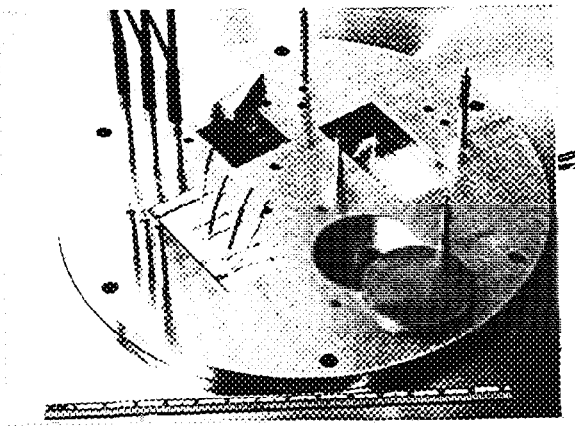

FIGURE 6.4 SAMPLE HOLDER ON BASE PLATE

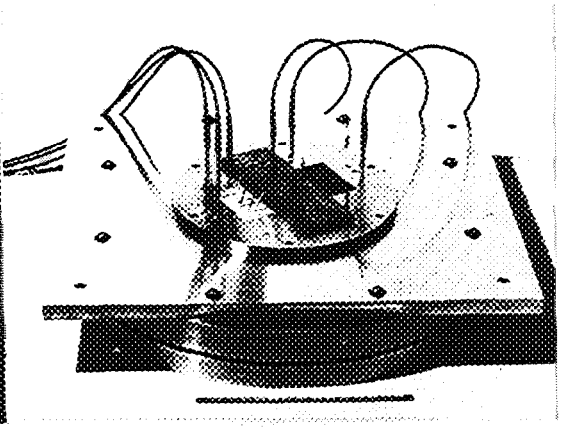

FIGURE 6.5 PARTIALLY ASSEMBLED CONDUCTIVITY EXPERIMENT

Table 6.2 gives the thicknesses of the standards used. A total of six pins were used for each standard. The pins were spring loaded against the base plate and against the standard. The signals from these pins gave the time of transit of the shock wave though the impedance standard and hence the shock velocity. The brass plate on top of the sample holder (as seen in Fig 6.5) was used to mount the spring loaded pins against the standards. Three additionall holes were provided in the brass plate for another set of free surface measurements. The location of each free surface and shock velocity pin was placed so as to avoid any rarefaction effects from the walls of the sample holder. The location of the spring loaded pins also provided the capability of determining the "tilt" of the shock front by comparing a number of shock arrival times.

Two pins were used as trigger pins to trigger oscilloscopes

and give a stop signal to a time interval counter. For the highest pressure shots, the aluminum base plate was not used. Instead, the sample holder was used to hold all of the samples directly in the path of the monel flyer. All surfaces were double checked for planarity with the optical gauge after they have been firmly epoxyed in place on the back surface (away from the flyer plate).

The sample holder was designed so that any bowing effects of the shock front would be minimized by placing the centers of all of the samples an equal distance from the center of the experiment.

TABLE 6.2

HUGONIOT STANDARDS FOR CONDUCTIVITY EXPERIMENTS

| SHOT | ALUMINUM IN mm | $Al_2O_3$ IN mm |
|---|---|---|
| 1 | 6.4301 ± .0014 | 6.6458 ± .0017 |
| 2 | 6.4332 ± .0021 | 6.4638 ± .0018 |
| 3 | 6.4169 ± .0034 | 6.6329 ± .0037 |
| 4 | 6.3836 ± .0001 | (Not Used) |
| 5 | 6.3895 ± .0017 | 6.4635 ± .0017 |
| 6 | 6.4118 ± .0014 | 6.5372 ± .0012 |
| 7 | 6.3932 ± .0018 | 6.6431 ± .0006 |
| 8 | 3.1646 ± .0019 | 6.5672 ± .0030 |
| 9 | 3.1971 ± .0020 | 6.4623 ± .0031 |
| 10 | 6.4067 ± .0004 | 6.3566 ± .0051* |
| 11 | 6.3647 ± .0037 | 6.3573 ± .0035* |

*Fe used as standard instead

## 6.3 EXPERIMENTAL MEASUREMENTS

Three types of measurements were made behind the shock front. The first type used the argon flash gap technique (M. van Thiel and B. J. Alder, 1966) on Equation of State samples. A very thin argon filled gap between the sample and a Lucite block is used to indicate either shock arrival time or free surface arrival time. An

intense light flash is generated by the rapidly compressed gas. The gas becomes incandescent immediately (on the order of $10^{-12}$ sec) after shock front arrival and lasts for about 20 nsec. By using brass or aluminum impedance standards on the same experiment with the unknown, both the shock and free-surface velocities can be determined. The optical signals are related to known locations of the gaps directly on the baseplate and samples. A slit is placed over each gap and the flashes are recorded by a streaking camera. The image of the slit is moved across the recording film at a precisely known velocity. From the known distance and time information both the shock and particle velocities are computed. Either of the two independent variables together with the known Hugoniot standard is then used in the Rankine-Hugoniot relationships to calculate the other variables. Appendix A shows the appropriate calculations. A series of six experiments were performed at different pressures to determine the Equation of State of the FeSi alloys. The known Hugoniots used in all calculations were obtained from Lawrence Livermore and Los Alamos Laboratory compendiums: Monel and alumina (van Thiel, et al, 1962; updated 1976); Indium, iron, brass and aluminum 2024 (McQueen, et al, 1969).

Once the EOS of the alloys was established, a shock impedance matching technique was used to determine the states reached in the conductivity samples. Self shorting pins were used to determine the state reached in the alumina and/or aluminum standard. The gap between the center conductor and the base of a coaxial pin forms the open circuit of a pin circuit. When the arriving shock

wave drives the base of the pin into the center conductor; it closes the circuit producing a pulse. A typical pin record is shown in Figure 6.6. The maximum error in repeatibility of the leading edge of the pulse is about 5 nanoseconds. The shock velocity measurements through the impedance standard were obtained by recording the time of arrival of the shock wave at the base plate and on top of each standard. The pin signals were transmitted by two foot coaxial cables to the pulse shaping circuit on a pin board where they were combined. A partially assembled pin board with three pins is shown in Figure 6.7. Each pair of pulses, representing the transit time of the shock through the sample, was brought to the firing bunker by a 50 ohm impedance coaxial cable. The signals were displayed on Denver raster scopes and recorded on glass photographic plates. The raster scopes were triggered about 5 microseconds before the projected shock arrival at the top of the aluminum base plate. The raster sweep rate used was 2.5 microsec per line, with a time marker every 0.5 microsec. The shock transit time was calculated from the time markers and pin pulses by reading each photographic plate on a Grant film reader. The uncertainties in the transit time are mostly due to pin repeatibility, and resolution of the leading edge of each pulse. The film reader, kept in a temperature controlled room, was capable of reading one part in a million or typically 0.0025 nsec (well beyond experimental resolution).

A dry run of up to 48 raster scopes was made before each experiment and the best set was selected based upon the focus,

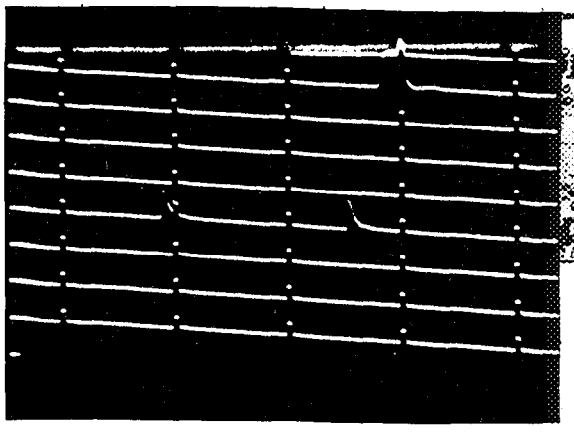

FIGURE 6.6 TYPICAL PIN RECORD

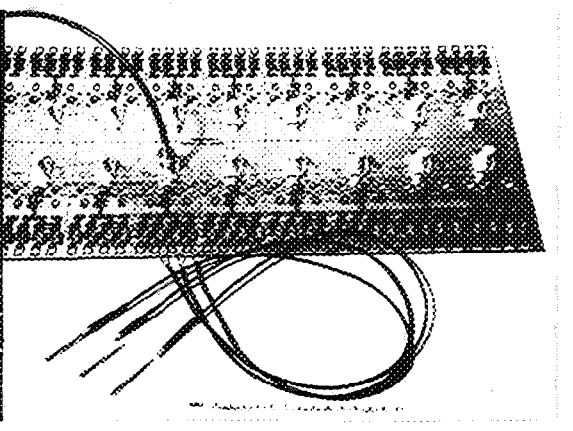

FIGURE 6.7 PARTIALLY ASSEMBLED PIN BOARD

linearity and clarity of the scopes. These scopes were adjusted for peak performance prior to each experiment. In addition to the three sets of shock velocity measurements taken for each standard, a number of free surface velocity measurements were also made. The free surface measurements were not essential since impedance standards were used. Free surface measurements were initially included to provide a separate means of determining the final state by independently finding the particle velocity through the standard samples. The free surface measurements showed more scatter in the data and were subsequently dropped. This phenomenon is very commonly observed and is due to the larger non-planarity of the free surface when compared to the interface between two solids. The 2024 aluminum standard is most useful up to about 1.0 Mbars while the alumina standard is useful only at pressures above 1.0 Mbars where the two wave structure of alumina is overdriven. Iron standard

samples were used where double sandwich (Fe, $Al_2O_3$, FeSi, $Al_2O_3$, Fe) conductivity samples were used.

The conductivity samples were sandwiched between two plates of alumina as shown in Figure 6.2. The final shock state reached in the thin FeSi alloy samples is reached by a series of reverberating shock waves and rarefactions. Figure 6.8 shows the displacement of the materials as a function of time. Section 3.4 described what occurs during the first three reverberations and how the final state was reached.

The third type of measurement involved the monitoring of the electrical conductivity as a function of time. A four electrode circuit was used in order to eliminate the effect of contact resistance. A constant current was passed through the outer electrodes of the sample. The potential drop between the inner electrodes was monitored on Tektronix 585A oscilloscopes. A schematic (Figure 6.9) illustrates the concept of the constant current source and Figure 6.10 shows the constant current circuit diagram used. The start circuit used Silicon Controlled Rectifiers (SCR's) to cleanly trigger the large capacitors (Figure 6.11). The capacitor-resistance (RC) time constant was very large compared to the duration of a shock experiment (Figure 6.12). The constant current pulser was triggered during the experiment by a time delayed detonation pulse through the start circuit. In the laboratory, and during a conductivity measurement just prior to the detonation, a pair of pulse generators were used to manually trigger the SCR's. The stop circuit was used for the purpose of

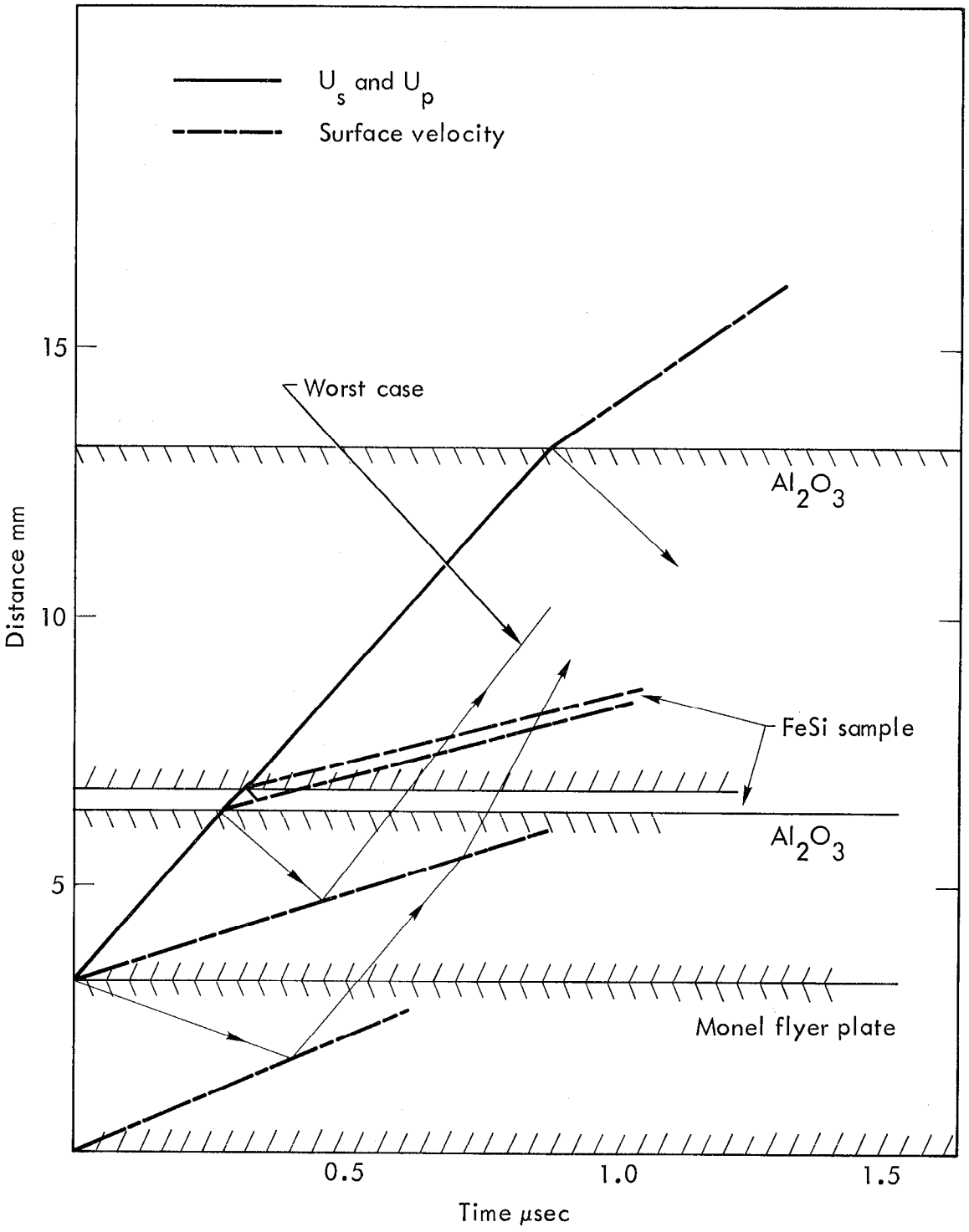


FIGURE 6.8 DISTANCE VS TIME FOR A FLYING PLATE CONDUCTIVITY EXPERIMENT

limiting the duration of the large current through the sample (to 100 microseconds) and thereby avoid heating the sample while it was monitored in the laboratory and prior to each experiment. A 900 volt regulated power supply was used to charge the current pulser.

A separate current pulser was close coupled to each conductivity sample in order to minimize the effect of ringing of

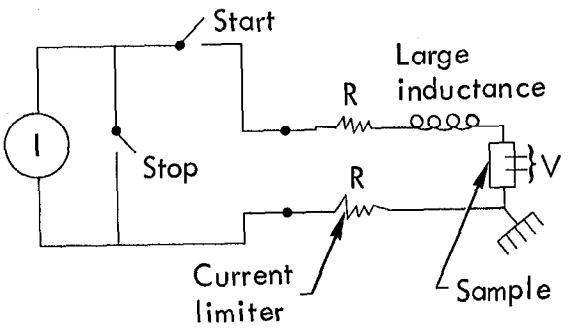


Constant current circuit

FIGURE 6.9

the observed demagnetization pulse. The current pulsers were physically mounted less than 10 cm away from the conductivity

samples. A large grounded brass can enclosure was used to surround each experiment in order to minimize stray electromagnetic interference. Only one common ground was used to tie the experimental set up and the entire bunker and thereby avoid stray

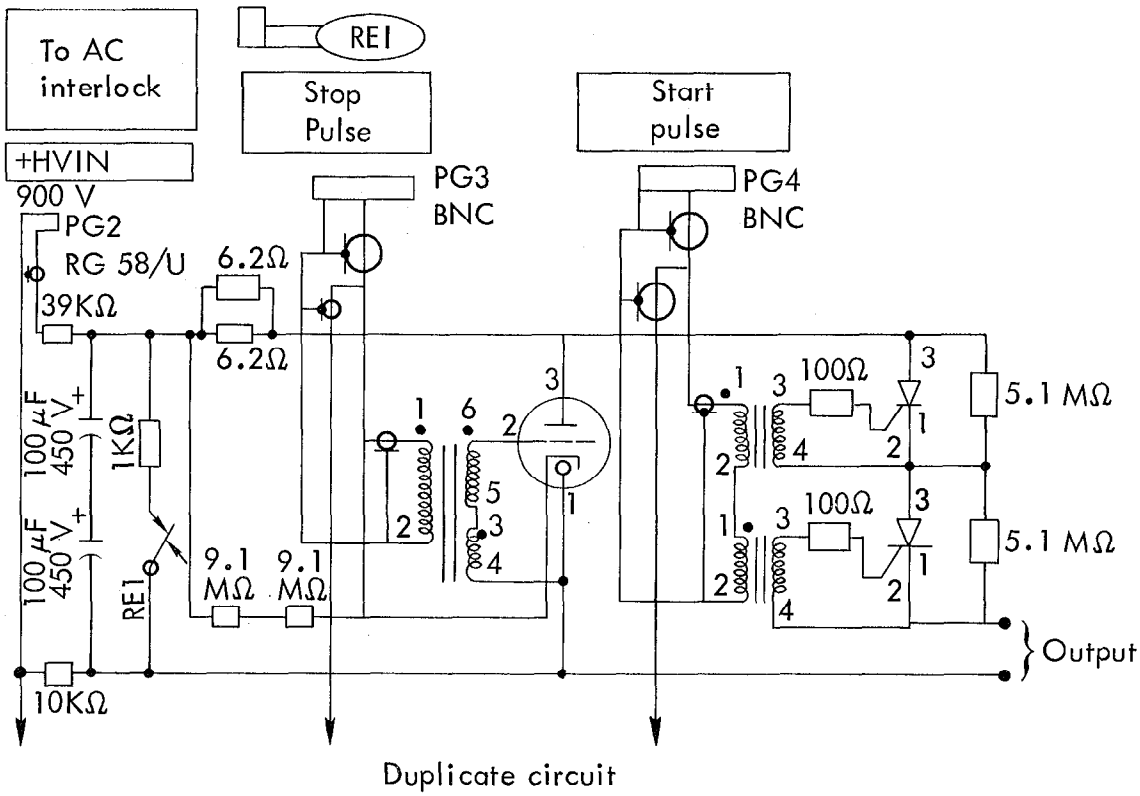


FIGURE 6.10 ELECTRICAL SCHEMATIC OF

CURRENT PULSER

ground loops. An AC interlock was used in order to ensure that no electrical charge was present while the experiment was positioned above the high explosive (Fig 6.13 shows the capacitors and the AC interlock).

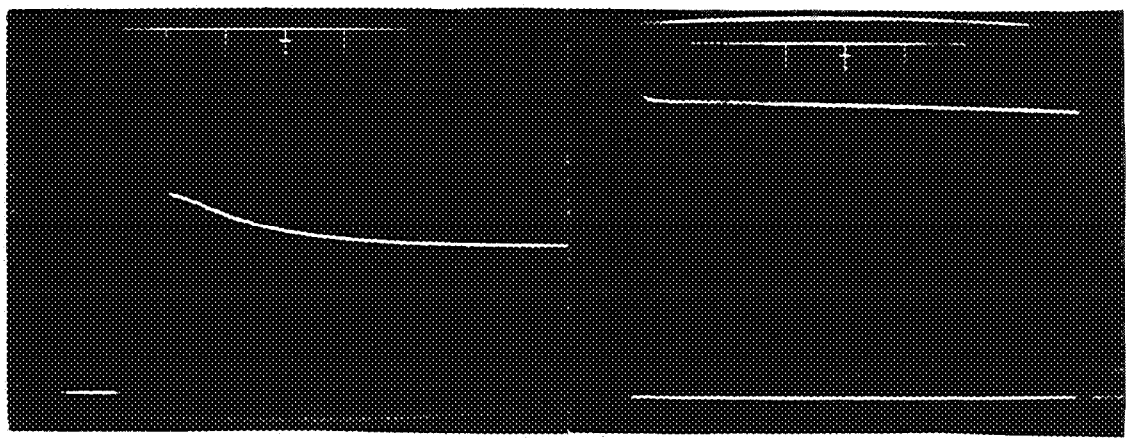

FIGURE 6.11 LEADING EDGE OF CURRENT PULSE, 0.5 MICROSEC/CM

FIGURE 6.12 LONG RC TIME OF CURRENT PULSE, 5 MICROSEC/CM

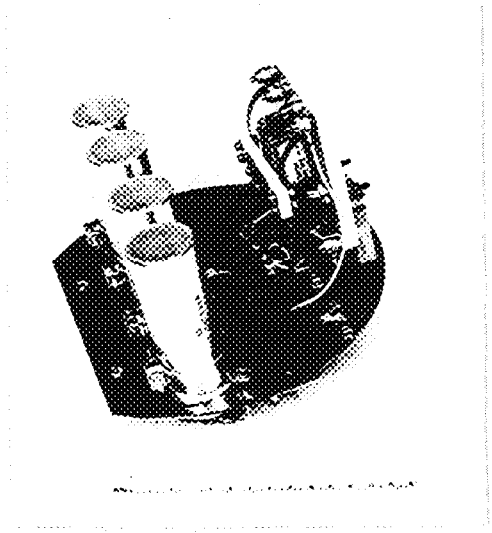

FIGURE 6.13 TOP VIEW OF CURRENT PULSER

The Tektronix scopes were triggered by a pair of self shorting pins. The preamp rise time for these scopes is on the order of 1.5 nanosec. Five scopes were typically used for each conductivity

sample. One or two of the scopes for each sample was triggered by the detonation pulse and an appropriate delay line. These scopes used a slow time sweep to insure that a record would be obtained even if both trigger pins failed. Another scope was used with a low vertical sensitivity and offset baseline in order to try and record the complete demagnetization pulse. The other three scopes were set at varying time sweeps and voltage sensitivities in order to make sure that the voltage drop before and after the shock front would be recorded. All of the conductivity data was recorded on Polaroid Type 410 film. Typical records of the demagnetization pulse and the conductivity before and after the shock front are shown in Figures 6.14, 6.15, and 6.16. The scope arrangement used is shown in Figure 6.17.

The change in conductivity appeared as a change in the voltage trace. The scopes were calibrated using an LEA70-1041 Oscilloscope Calibrator with a Tektroniz Type 184 Time Mark Generator. The calibration traces of the time and voltage signal were recorded. (A typical calibration is shown in Figure 6.18). In order to minimize the reflections of the demagnetization pulse from imperfect scope terminations, long delay lines of 200 nanosec were used in the last few shots before the usual 50 ohm terminators. This way, the first reflection arrived 400 nanosec after the demagnetization pulse and at about the end of the experiment. This significantly reduced the interference of the demagnetization pulse on the oscilloscope traces.

The conductivity samples and their electrical leads were epoxyed firmly in place. After the first four experiments, extra

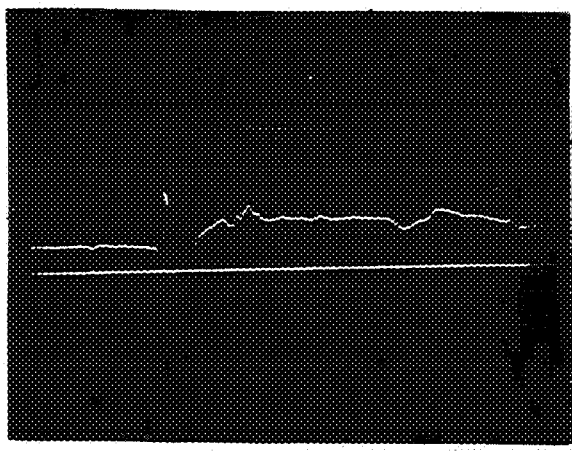

FIGURE 6.14 CONDUCTIVITY MEASUREMENT, 0.2 MICROSEC/CM

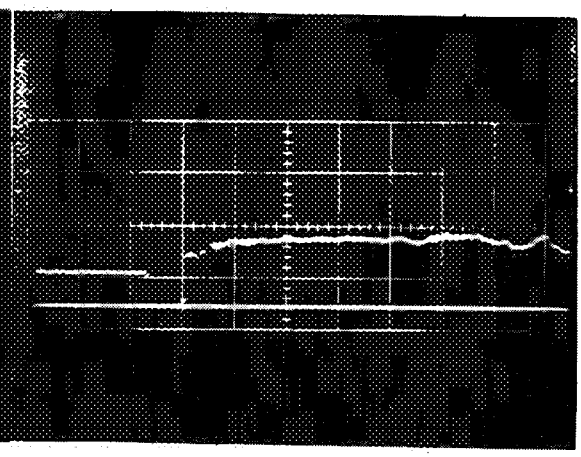

FIGURE 6.15 CONDUCTIVITY MEASUREMENT, 0.1 MICROSEC/CM

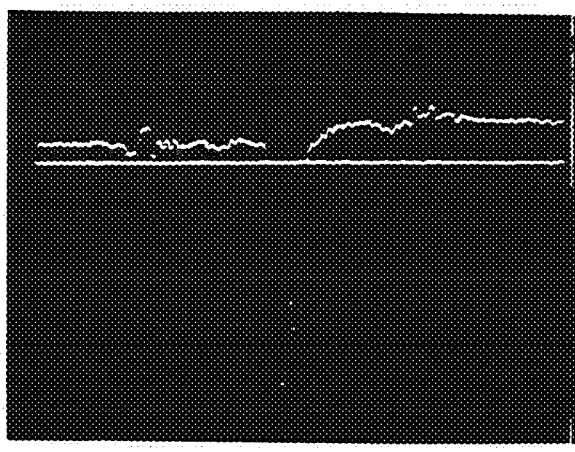

FIGURE 6.16 DEMAGNETIZATION PULSE, 0.1 MICROSEC/CM

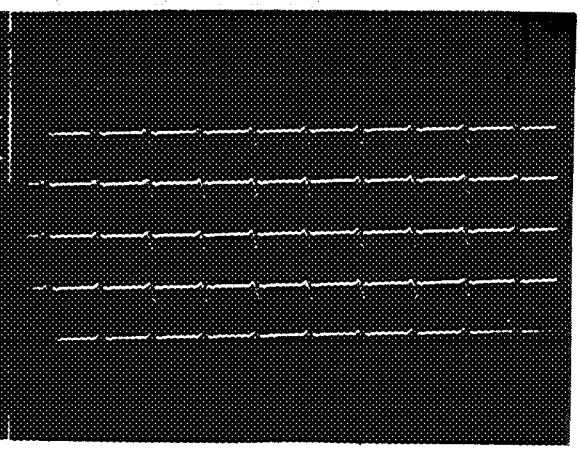

FIGURE 6.17 SCOPE CALIBRATION, VOLTAGE AND TIME

electrical shielding was provided on top of each conductivity sample in order to locate and possibly eliminate the observed noise ripple (discussed in another section). The electrical shielding consisted

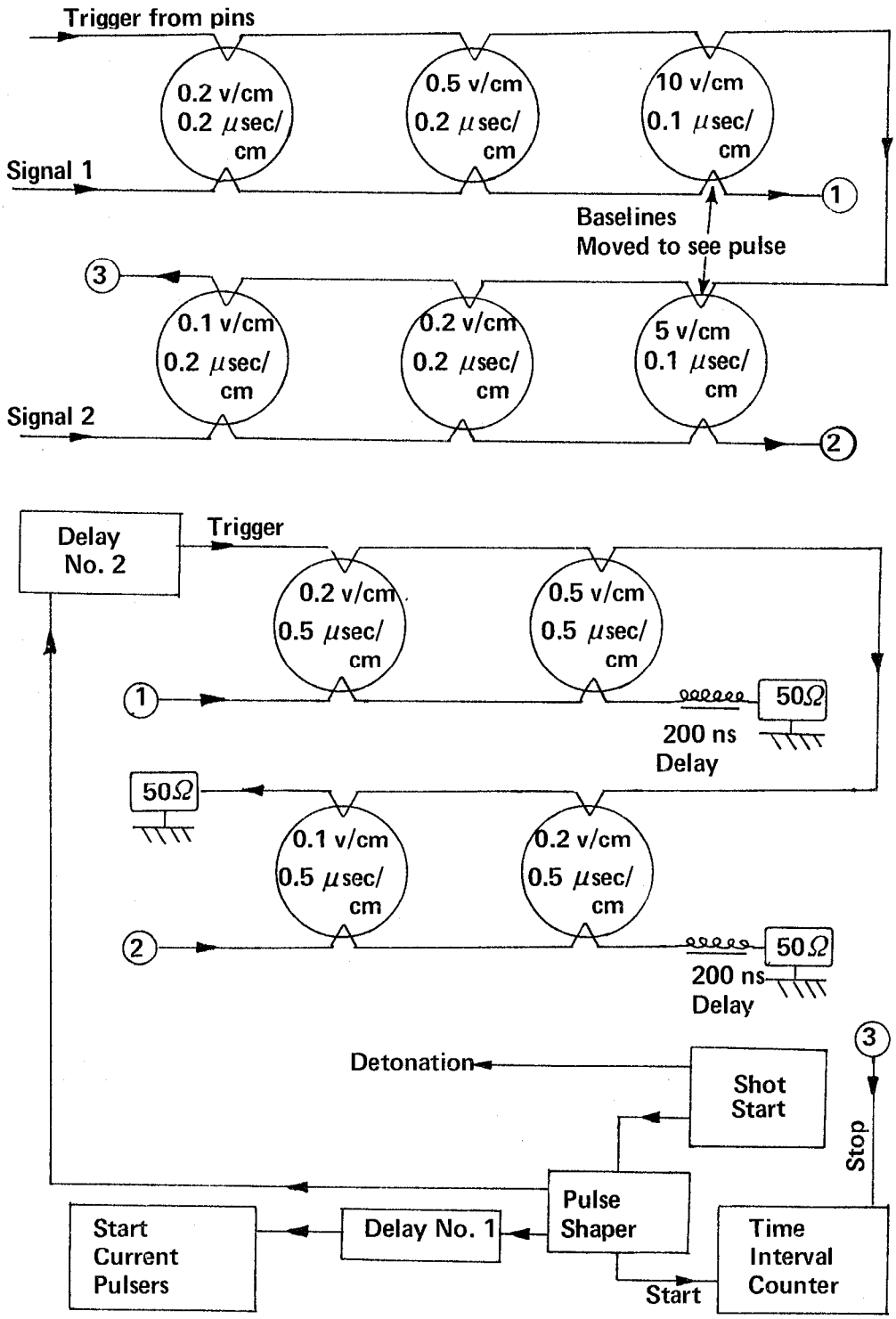


FIGURE 6.17 TYPICAL OSCILLOSCOPE ARRANGEMENT

of copper plates with 0.5 cm openings for the electrical leads. The copper plates were firmly grounded to the sample holder which was connected to the experimental common ground. The electrical shielding reduced only a small portion of the spurrious signals.

The lower ring of the shot assembly (see Fig 6.5) is used not only to accurately position the flyer plate with respect to the base plate, but also as a collar which is used to locate the experiment above the explosive.

Both conductivity samples on shot 10 and one sample on shot 11 were enclosed in much thinner $Al_2O_3$ sandwich plates (0.091 cm) which were in turn enclosed in a 0.315 cm thick iron base and cover (with the appropriate clearances for the electrical leads which had $Al_2O_3$ sleeves between the leads and the iron cover). The idea behind this double sandwich was to let the conductivity samples reverberate to a final pressure of iron that is very close to the FeSi alloys. This was to eliminate the off Hugoniot corrections required in all of the other experiments. Unfortunately, the voltage traces after the start of the demagnetization pulses could not be properly read. This could have been caused by the Indium electrical probes being sheared off the conductivity sample due to an impedance mismatch between iron and indium.

## 7.0 EXPERIMENTAL RESULTS AND ANALYSIS

As stated in the introduction, the two main objectives of the experimental effort were to: measure the Hugoniot of three FeSi alloy concentrations in the pressure range of 100 to 1500 Kbars and measure the electrical conductivity of four FeSi alloy

concentrations at the high off-Hugoniot pressures reached in the sandwich conductivity samples between 500 and 1400 Kbars.

## 7.1 EQUATION OF STATE

The Hugoniot of FeSi alloys, $X_{si}$ = 0.077, 0.181, and 0.342, has been measured using flash gap and impedance matching techniques (van Thiel and Alder, 1966). Brass and aluminum 2024 were used as impedance standards on separate experiments. Six Ester shock wave experiments were performed and a total of twenty samples used. The film records of each sample and four impedance standards of each experiment were read on the Grant film reader. First the shock velocity and free surface velocity of the impedance standards were used to calculate the pressure reached, then the EOS parameters were found for the unknowns. The sample calculations are shown in Appendix A. The resultant Hugoniot data is given in Table 7.1 and in Figures 7.1 and 7.2.

The $U_s$ vs $U_p$ and P vs V behavior show definite solid state phase transformations, presumably to a hcp structure, for $X_{si}$ = 0.077 and 0.181 somewhere between 106 and 366 Kbars. Above this pressure, linear fits of the data were obtained in the $U_s$ vs $U_p$ plane. For $X_{si}$ = 0.342, a possible break in the linear behavior can be observed between 525 and 600 Kbars in agreement with Balchan and Cowan. However, the possible break is so slight that a linear fit over the entire pressure range from 122 to 1532 Kbars is justified. For the most interesting cases, $X_{si}$ = 0.181 and $X_{si}$ = 0.342, the scatter in the data was less than that reported by Balchan and Cowan as well as

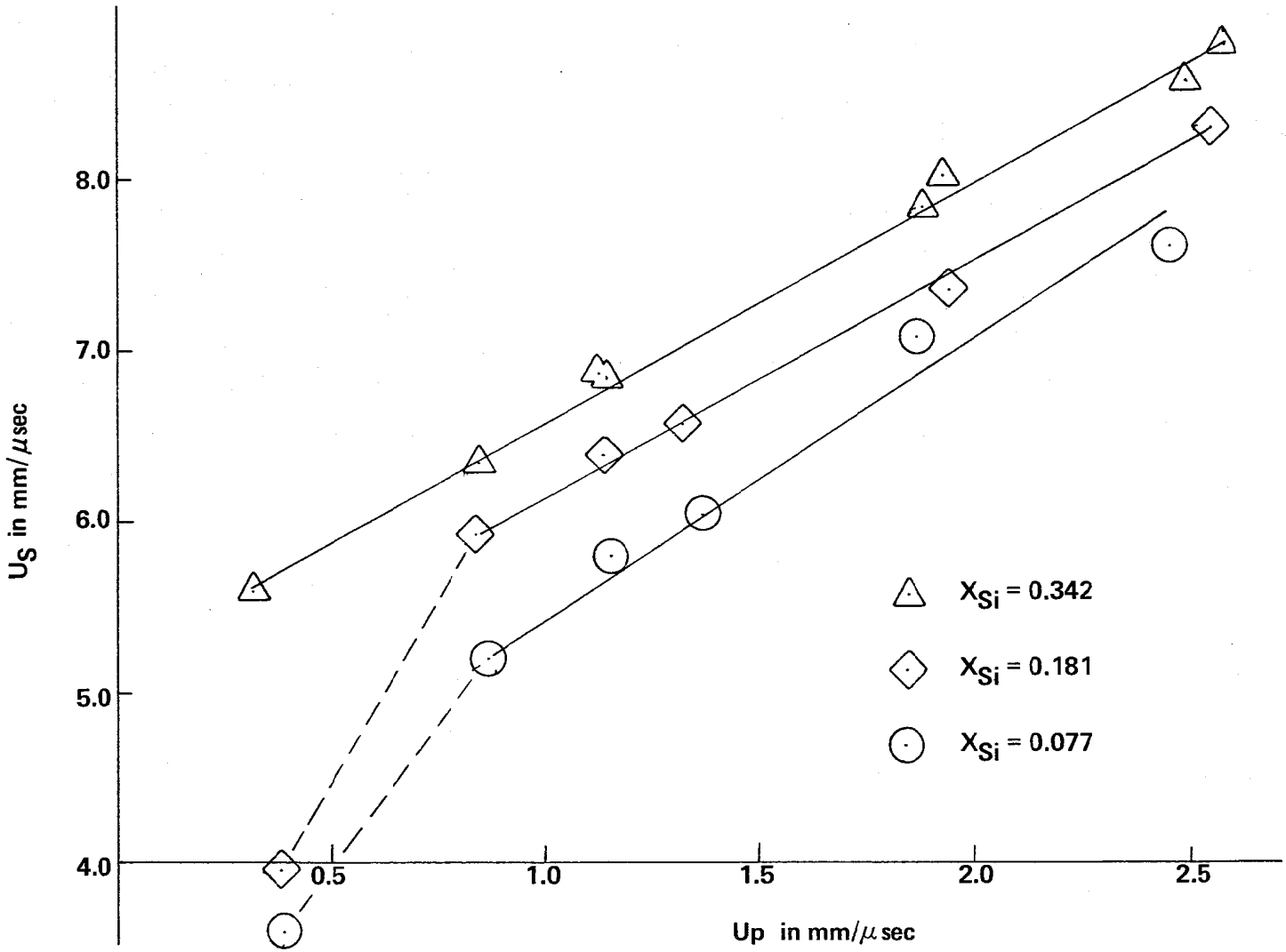


FIGURE 7.1 $U_s$ VS $U_p$, FeSi HUGONIOT DATA

FIGURE 7.2 P VS V, FeSi HUGONIOT DATA

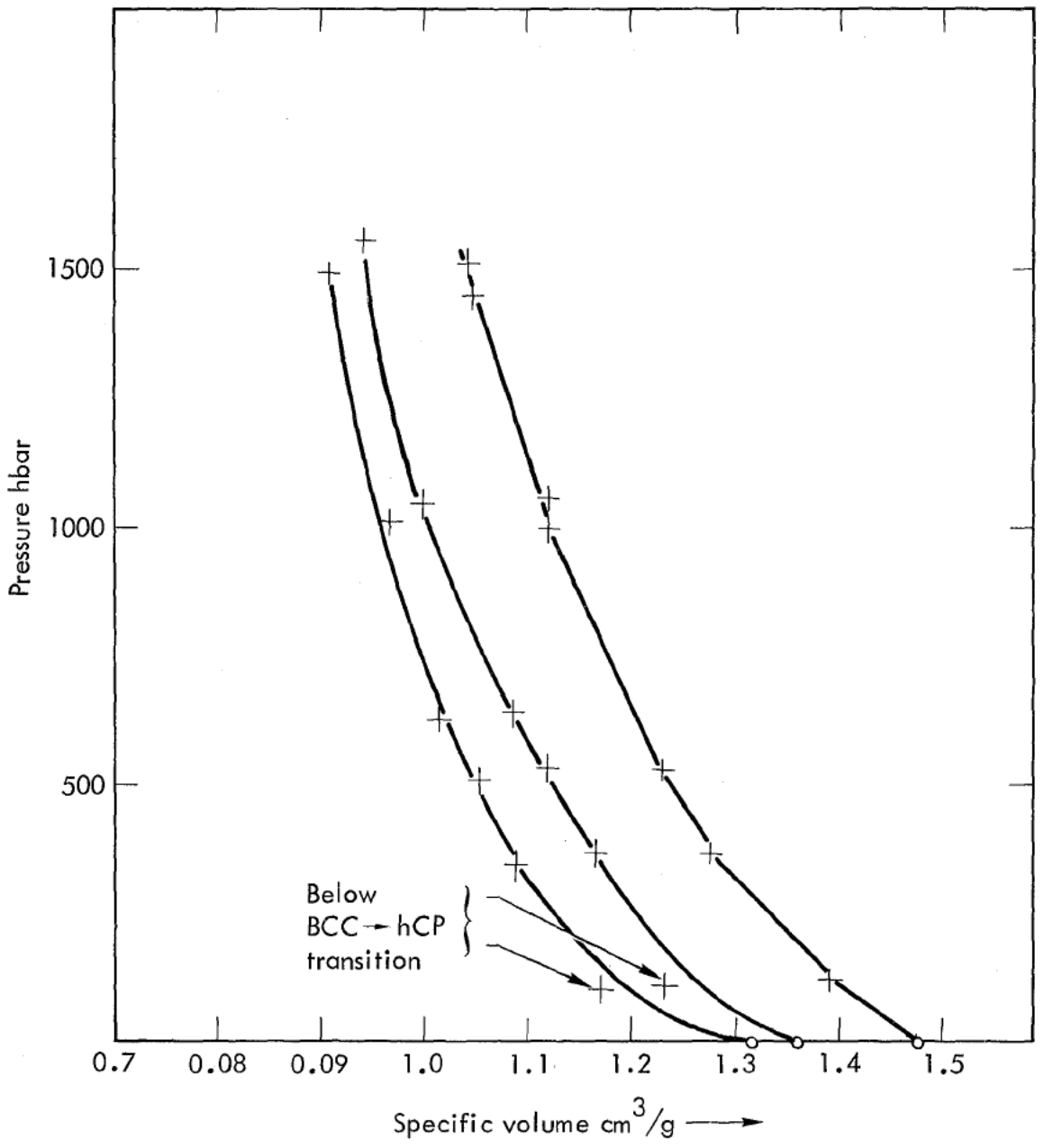

TABLE 7.1

EXPERIMENTAL HUGONOITS FOR FeSi ALLOYS

| | $X_{si}$ = 0.077 | av $\rho o$ = 7.606 ± 0.010 | | Vo = 0.0315cm$^3$/g | |
|---|---|---|---|---|---|
| Standard | $\rho$ gm/cm$^3$ | $U_s$ mm/ $\mu$ sec | $U_p$ mm/ $\mu$ sec | P Kbars | V/Vo |
| Al | 7.605 | 3.604 | 0.388 | 106 | .892 |
| Al | 7.601 | 5.180 | 0.869 | 342 | .832 |
| Al | 7.589 | 5.794 | 1.152 | 507 | .8013 |
| Brass | 7.614 | 6.020 | 1.362 | 624 | .7738 |
| Brass | 7.611 | 7.093 | 1.869 | 1009 | .7365 |
| Brass | 7.616 | 7.616 | 2.450 | 1488 | .6928 |
| | $X_{si}$ = 0.181 | av $\rho o$ = 7.3544 ± .0045 | | Vo = 0.1360 | |
| Al | 7.349 | 3.926 | .380 | 110 | .903 |
| Al | 7.348 | 5.933 | .840 | 366 | .8584 |
| Al | 7.358 | 6.389 | 1.125 | 529 | .8239 |
| Brass | 7.359 | 6.566 | 1.320 | 638 | .7989 |
| Brass | 7.354 | 7.341 | 1.941 | 1048 | .7356 |
| Brass | 7.353 | 8.298 | 2.550 | 1556 | .6927 |
| | $X_{si}$ = 0.342 | av $\rho o$ = 6.7701 ± .0027 | | Vo = 0.1477 | |
| Al | 6.784 | 5.567 | .322 | 122 | .9422 |
| Al | 6.784 | 6.3216 | .850 | 365 | .8655 |
| Brass | 6.784 | 6.836 | 1.145 | 531 | .8325 |
| Brass | 6.784* | 6.801 | 1.135 | 524 | .8331 |
| Brass | 6.784 | 7.822 | 1.883 | 999 | .7593 |
| Brass | 6.780* | 8.033 | 1.935 | 1054 | .7591 |
| Brass | 6.784 | 8.575 | 2.492 | 1450 | .7094 |
| Brass | 6.777* | 8.772 | 2.575 | 1508 | .7065 |

*1/8 inch thick samples

Kormer and Funtikov. Least squares fits were made to the data (see Table 7.2).

The temperature along the Hugoniot, 0°K isotherm (cold compression curve) and Grüneisen gamma calculations were performed by a computer code, GRAY (Royce, 1971). The calculations are based on the Dugdale-McDonald formulation of the Grüneisen EOS description of solids (Dugdale and McDonald, 1953; Grover, et al, 1969). The electronic specific heat was included in the formulation of the equation of state, i.e., the thermal exitation of electrons was taken into account. Results of these calculations are presented in Table 7.3.

For the most probable concentration, $X_{si} = 0.25$, an EOS was formulated on the basis of the measured Hugoniots of $X_{si} = 0.181$ and 0.342. The measured density of $\rho_o = 7.183$ gm/cm$^3$ was used and the $U_s$ vs $U_p$ fit ($U_s = 4.91 + 1.37\ U_p$) was obtained from data shown in Fig 7.1. In addition to the calculations necessary for the characterization of the conductivity measurements, the seismic velocity, density and pressure were calculated along a selected adiabat (isentrope). The results fall within the narrow range of allowable Monte Carlo solutions for the outer core (Press, 1970) and are presented in Fig 7.3 and Table 7.4.

## 7.2 DEMAGNETIZATION

A demagnetization pulse has been observed on every conductivity experiment. It is due to a transition to a non-magnetic state. The same effect has been observed in pure iron by Keeler and Mitchell (1969) and is attributed to the solid state transition

from a bcc to a hcp structure. The magnitude of this pulse has been observed to be on the order of 20 to 50 times as large as the measured voltage drop of the initial and final states of the conductivity experiments and of the opposite polarity. The shape and duration of the pulse has been derived theoretically (see

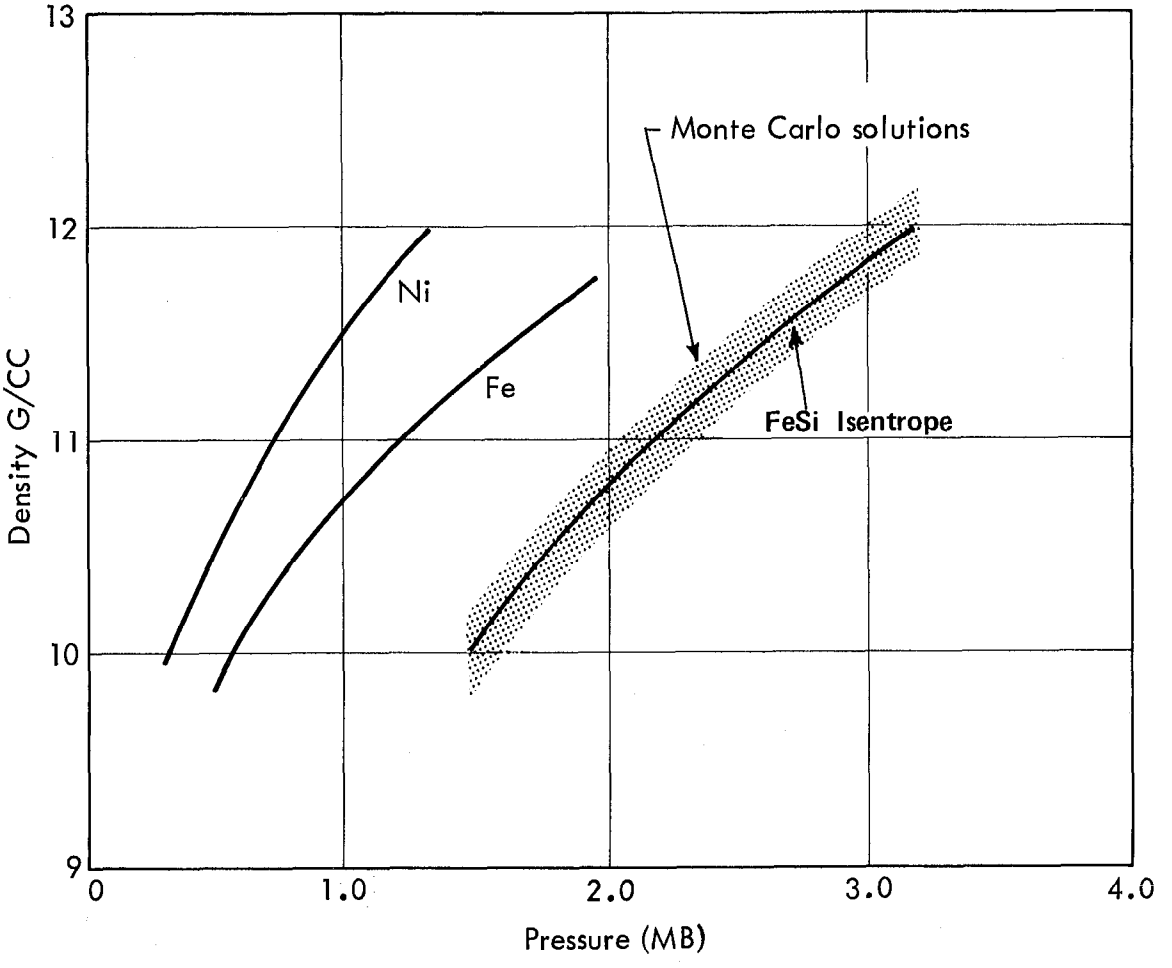


FIGURE 7.3 $X_{si}$ = 0.25 ISENTROPE AND THE EARTH'S CORE

Appendix C) and is in agreement with observation. The lower pressure experiments showed a pulse that appeared to be the superposition of

TABLE 7.2

LEAST SQUARES FIT TO $U_s$, $U_p$ DATA

Linear Fit: $U_s = C + S\,U_p$; Sigma is Standard Deviation

| $X_{si}$ | C | S | SIGMA |
|---|---|---|---|
| **This Work** | | | |
| 0.077 | 3.68 ± 0.12 | 1.77 ± 0.07 | 0.092 |
| 0.181 | 4.80 ± 0.07 | 1.36 ± 0.04 | 0.059 |
| 0.342 | 5.16 ± 0.06 | 1.40 ± 0.04 | 0.069 |
| **Balchan and Cowan Data*** | | | |
| 0.077 | 4.07 ± 0.12 | 1.56 ± 0.06 | 0.073 |
| 0.329 | 5.44 ± 0.13 | 1.24 ± 0.06 | 0.103 |
| **Kormer and Funtikov Data** | | | |
| 0.296 | 4.83 ± 0.32 | 1.37 ± 0.12 | 0.286 |

*See discussion on the composition of the samples for $X_{si}$ = 0.324 in Section 4.

two pulses. At 1000 Kbars and above, only one pulse (or nearly complete overlap) was observed. This is consistent, because the effect of the magnetic field is proportional to the magnitude of the field within the sample. The magnetic field has a null in the middle of the sample thickness. Therefore, for slower shock transit (and consequently phase transition) times, a double pulse will be seen. A similar effect would be seen at higher pressures if the sample thickness were made larger.

TABLE 7.3

COLD COMPRESSION CURVES (0°K ISOTHERMS)

| $X_{si} = 0.077$ | | | $X_{si} = 0.181$ | | |
|---|---|---|---|---|---|
| $\rho$ gm/cm$^3$ | P Kbars | $\gamma$ (V) | $\rho$ gm/cm$^3$ | P Kbars | $\gamma$ (V) |
| 11.07 | 1,148 | 2.083 | 10.60 | 1,325 | 1.353 |
| 10.82 | 1,001 | 2.090 | 10.40 | 1,203 | 1.365 |
| 10.52 | 889 | 2.095 | 10.04 | 1,004 | 1.385 |
| 10.45 | 805 | 2.097 | 9.862 | 907 | 1.396 |
| 10.23 | 699 | 2.097 | 9.658 | 804 | 1.406 |
| 10.02 | 605 | 2.097 | 9.435 | 697 | 1.417 |
| 9.758 | 499 | 2.097 | 9.222 | 602 | 1.427 |
| 9.484 | 399 | 2.104 | 8.994 | 503 | 1.439 |
| 9.175 | 299 | 2.136 | 8.729 | 398 | 1.458 |

| $X_{si} = 0.25$ | | | $X_{si} = 0.342$ | | |
|---|---|---|---|---|---|
| $\rho$ gm/cm$^3$ | P Kbars | $\gamma$ (V) | $\rho$ gm/cm$^3$ | P Kbars | $\gamma$ (V) |
| 10.19 | 1,259 | 1.381 | 9.599 | 1,344 | 1.435 |
| 9.932 | 1,105 | 1.396 | 9.390 | 1,196 | 1.449 |
| 9.750 | 999 | 1.407 | 9.246 | 1,100 | 1.459 |
| 9.574 | 901 | 1.417 | 9.078 | 992 | 1.469 |
| 9.377 | 797 | 1.422 | 8.917 | 893 | 1.479 |
| 9.188 | 703 | 1.437 | 8.761 | 802 | 1.488 |
| 8.982 | 604 | 1.447 | 8.586 | 704 | 1.497 |
| 8.736 | 495 | 1.460 | 8.394 | 603 | 1.507 |
| 8.503 | 399 | 1.479 | 8.189 | 502 | 1.519 |
| 8.240 | 298 | 1.513 | 7.972 | 402 | 1.537 |

The "unwanted" signals, from a diagnostic point of view, have caused experimental problems that have been brought under control. The interference of the demagnetization pulse of 50 to 80 nanosec duration and its reflections during the 0.4 microsecond useful "lifetime" of the final state is one of the dominant sources of error of electrical conductivity. The addition of 200 ~~micro~~nano second delay lines before signal cable termination solved this problem.

TABLE 7.4

ISENTROPE OF $X_{si}$ = 0.25 FOR OUTER CORE

| $\rho$ gm/cm$^3$ | P Kbars | T °K | $\phi$ km/sec |
|---|---|---|---|
| 10.03 | 1,391 | 2,915 | 8.042 |
| 10.56 | 1,755 | 3,093 | 8.518 |
| 10.88 | 1,997 | 3,200 | 8.801 |
| 11.18 | 2,241 | 3,301 | 9.063 |
| 11.51 | 2,514 | 3,405 | 9.336 |
| 11.76 | 2,740 | 3,488 | 9.548 |
| 12.03 | 2,988 | 3,573 | 9.766 |
| 12.26 | 3,213 | 3,646 | 9.953 |

MONTE CARLO MODELS (PRESS, 1970 AND 1972)

Top of Outer Core:

$\rho = 10.05 \pm 0.15$ gm/cm$^3$; $\phi = 7.96 \pm 0.20$ km/sec

Bottom of Outer Core:

$\rho = 12.25 \pm 0.15$ gm/cm$^3$; $\phi = 10.15 \pm 0.25$ km/sec

The demagnetization pulse is caused by the driving wave ($P_1$ in Figure 3.8) which transforms the ferromagnetic FeSi sample into a paramagnetic state. The change in magnetic susceptibility is dramatic: from a value on the order of 1000 to a final value of 1. The original magnetic field set up by the current pulser can no longer be supported. As the magnetic field collapses, it induces a back EMF which generates the eddy current. This is readily picked up by the voltage probes in the form of a sharp pulse. The risetime of the pulse is related to the phase transition time T (which is equal to the shock transit time within experimental error for the high pressure experiments). The eddy current decays in a characteristic time $\tau$ which is given by

$$\tau = \frac{\mu_0 \sigma_1 \ell^2}{4 \pi^2} \tag{7.1}$$

where $\mu_o$ is the magnetic susceptibility of the final state, $\sigma_1$, is the electrical conductivity of the shocked state and $\ell$ is the thickness of the sample. From Appendix C, the measured potential drop $v_1$ (t) across the voltage leads is given as

$$v_1 (t) = v_o \frac{R_1}{R_o} \left[ 1 - \frac{2 \mu_i}{\mu_o} e^{-t/\tau} \right] \tag{7.2}$$

where $R_o$ and $R_1$ are the initial and final resistance of the sample and where $\mu_i$ is the initial susceptibility. The agreement between the experimentally measured decay time and the calculated value given by eq 7.1 is within the experimental uncertainties (see Table 7.5). The high cost and effort of each shot precluded investigating the variation of decay as a function of sample thickness for a sufficient range of sample thicknesses. Previous works by Royce established an analogous relationship (pulse width quadratically proportional to the sample thickness) with the magnetic flux experiments (the results of these experiments are discussed in Sections 5.1 and 8.4).

## 7.3 ELECTRICAL CONDUCTIVITY

The conductivity of the shocked state is obtained from the voltage drop given by eq 7.2, the initial dimensions of the sample, the initial conductivity and the fact that the thickness of the sample has been compressed by a factor $V_F/V_0$ (where $V_F$ is the final volume of the off-Hugoniot state). The shocked state of the impedance standard used in the conductivity experiments is given in Table 7.6.

Oscilloscope traces of many of the conductivity experiments show a disturbance well ahead of the demagnetization pulse. This noise has been positively correlated to the breakout time of the shock front out of the aluminum baseplate. The conductivity samples with their sensitive conductivity measuring circuits served as antennas for this high frequency noise. In fact, in a number of cases, definite interference from shock pin pulses were also picked up. Neither of these two noise signals seriously interfered with the conductivity measurements.

The electrical conductivity of four FeSi concentrations, $X_{si}$ = 0.077, 0.181, 0.25 and 0.342, has been measured in the pressure range of 500 to 1400 Kbars and the accompanying temperature range of 600°K to 2500°K. Two types of calculations were performed to characterize the off-Hugoniot states reached during the conductivity experiments. A first order solution was obtained by graphic construction and a hand calculator with the simplifying assumption that the release adiabat between the FeSi and $Al_2O_3$ Hugoniots can be represented by a mirror image of the Hugoniot (Altshuler, et al, 1958). The results for the volume and temperature corrections, as calculated by the first order solution and by the computer code, GRAY, agreed to better than 0.6% over the entire range and are well within the experimental error (see Appendix A). The results for the electrical conductivity, pressure, volume and temperature are given in Table 7.7.

The conductivity of the lowest Si concentration followed the behavior of pure iron (see Fig 7.4). The conductivity of the other

TABLE 7.5

DEMAGNETIZATION DECAY TIME

| $X_{si}$ | P Kbar | τ Calc Nsec | τ Meas Nsec | |
|---|---|---|---|---|
| 0.077 | 502 | 39.8 ± 2.5 | 34 ± 10 | + |
| | 745 | 23.4 | * | |
| | 1013 | 20.9 | * | |
| | 1045 | 25.0 | * | |
| | 1422 | 14.0 ± 0.5 | 10 ± 5 | |
| 0.181 | 502 | 28.0 ± 2.6 | 20 ± 10 | + |
| | 745 | 22.5 | * | |
| | 1013 | 23.2 | * | |
| | 1340 | 17.2 ± 1.1 | 16 ± 3 | |
| 0.250 | 521 | 19.7 ± 1.1 | 26 ± 10 | + |
| | 733 | 16.9 ± 1.2 | 18 ± 8 | + |
| | 1019 | 15.1 ± 0.8 | 12 ± 3 | |
| | 1422 | 10.5 | * | |
| 0.342 | 521 | 5.4 ± 0.2 | 9 ± 5 | |
| | 733 | 11.1 ± 1.4 | 17 ± 8 | + |
| | 1038 | 14.1 | Not Instrumented | |
| | 1038 | 7.8 ± 0.3 | 9 ± 3 | |
| | 1045 | 7.8 | * | |
| | 1340 | 9.7 ± 0.5 | 9 ± 3 | |

*Demagnetization pulse off scale on oscilloscope

+Hard to read accurately

TABLE 7.6

HUGONIOT STATE OF IMPEDANCE STANDARD, CONDUCTIVITY EXPERIMENTS

| SHOT | STANDARD | $\Delta t$ $\mu$ sec | $U_s$ mm/ $\mu$ sec | $U_p$ mm/ $\mu$ sec* | P Kbar |
|---|---|---|---|---|---|
| 1 | $Al_2O_3$ | .6220 ± .0021 | 10.684 ± .035 | 2.534 | 1038 ± 17 |
| 2 | $Al_2O_3$ | .6040 ± .0084 | 10.702 ± .149 | 2.550 | 1045 ± 21 |
| 3 | $Al_2O_3$ | .6260 ± .0106 | 10.620 ± .050 | 2.491 | 1013 ± 20 |
| 4 | Al | .7434 ± .0082 | 8.587 ± .095 | 2.436 | 583 ± 19 |
| 5 | Al | .7467 ± .006 | 8.557 ± .076 | 2.413 | 574 ± 16 |
| 6 | Al | .8268 ± .0054 | 7.755 ± .051 | 1.814 | 392 ± 11 |
| 7 | Al | .8177 ± .0059 | 7.819 ± .057 | 1.861 | 406 ± 12 |
| 8 | $Al_2O_3$ | .5754 ± .0008 | 11.413 ± .019 | 3.067 | 1340 ± 27 |
| 9 | $Al_2O_3$ | .5572 ± .0030 | 11.598 ± .063 | 3.201 | 1422 ± 28 |
| 10 | Fe | 1.0791 ± .0012 | 5.891 ± .008 | 1.267 | 587 ± 15 |
| 11 | Fe | .8531 ± .0001 | 7.452 ± .009 | 2.185 | 1270 ± 25 |

*The error in $U_p$ was nominally 1.5%

TABLE 7.7

ELECTRICAL CONDUCTIVITY AT HIGH PRESSURES

| $\sigma$ X $10^{-3}$ mho/cm | $P_F$ Kbar | $V_F/V_o$* | $T_F$ °K |
|---|---|---|---|
| | $X_{si}$ = 0.077 | | |
| 18.8 ± 1.2 | 502 ± 12 | .7990 | 672 |
| 17.3 ± 1.3 | 745 ± 27 | .7603 | 1,094 |
| 15.21 ± .61 | 1013 ± 20 | .7319 | 1,684 |
| 16.59 ± .91 | 1045 ± 21 | .7290 | 1,770 |
| 11.75 ± .42 | 1422 ± 28 | .6989 | 2,740 |
| | $X_{si}$ = 0.181 | | |
| 9.61 ± .88 | 502 ± 12 | .8214 | 670 |
| 9.34 ± .78 | 745 ± 27 | .7800 | 1,072 |
| 9.70 ± .74 | 1013 ± 20 | .7435 | 1,624 |
| 8.75 ± .54 | 1340 ± 27 | .6916 | 2,483 |
| | $X_{si}$ = 0.25 | | |
| 8.64 ± .46 | 521 ± 15 | .8262 | 672 |
| 8.15 ± .57 | 733 ± 23 | .7872 | 1,010 |
| 8.63 ± .47 | 1019 ± 20 | .7471 | 1,572 |
| 8.70 ± .47 | 1422 ± 28 | .7062 | 2,518 |
| | $X_{si}$ = 0.342 | | |
| 5.74 ± .18 | 521 ± 15 | .8332 | 670 |
| 5.47 ± .69 | 733 ± 23 | .7956 | 1,003 |
| 5.54 ± .20 | 1038 ± 17 | .7549 | 1,597 |
| 6.25 ± .20 | 1038 ± 17 | .7549 | 1,597 |
| 6.13 ± .21 | 1045 ± 21 | .7540 | 1,613 |
| 6.65 ± .35 | 1340 ± 27 | .7058 | 2,339 |

*The error in $V_F/V_o$ is less than 2%.

TABLE 7.7

ELECTRICAL CONDUCTIVITY AT HIGH PRESSURES

| $\sigma$ X $10^{-3}$ mho/cm | $P_F$ Kbar | $V_F/V_o$* | $T_F$ °K |
|---|---|---|---|
| | $X_{si}$ = 0.077 | | |
| 18.8 ± 1.2 | 502 ± 12 | .7990 | 672 |
| 17.3 ± 1.3 | 745 ± 27 | .7603 | 1,094 |
| 15.21 ± .61 | 1013 ± 20 | .7319 | 1,684 |
| 16.59 ± .91 | 1045 ± 21 | .7290 | 1,770 |
| 11.75 ± .42 | 1422 ± 28 | .6989 | 2,740 |
| | $X_{si}$ = 0.181 | | |
| 9.61 ± .88 | 502 ± 12 | .8214 | 670 |
| 9.34 ± .78 | 745 ± 27 | .7800 | 1,072 |
| 9.70 ± .74 | 1013 ± 20 | .7435 | 1,624 |
| 8.75 ± .54 | 1340 ± 27 | .6916 | 2,483 |
| | $X_{si}$ = 0.25 | | |
| 8.64 ± .46 | 521 ± 15 | .8262 | 672 |
| 8.15 ± .57 | 733 ± 23 | .7872 | 1,010 |
| 8.63 ± .47 | 1019 ± 20 | .7471 | 1,572 |
| 8.70 ± .47 | 1422 ± 28 | .7062 | 2,518 |
| | $X_{si}$ = 0.342 | | |
| 5.74 ± .18 | 521 ± 15 | .8332 | 670 |
| 5.47 ± .69 | 733 ± 23 | .7956 | 1,003 |
| 5.54 ± .20 | 1038 ± 17 | .7549 | 1,597 |
| 6.25 ± .20 | 1038 ± 17 | .7549 | 1,597 |
| 6.13 ± .21 | 1045 ± 21 | .7540 | 1,613 |
| 6.65 ± .35 | 1340 ± 27 | .7058 | 2,339 |

*The error in $V_F/V_o$ is less than 2%.

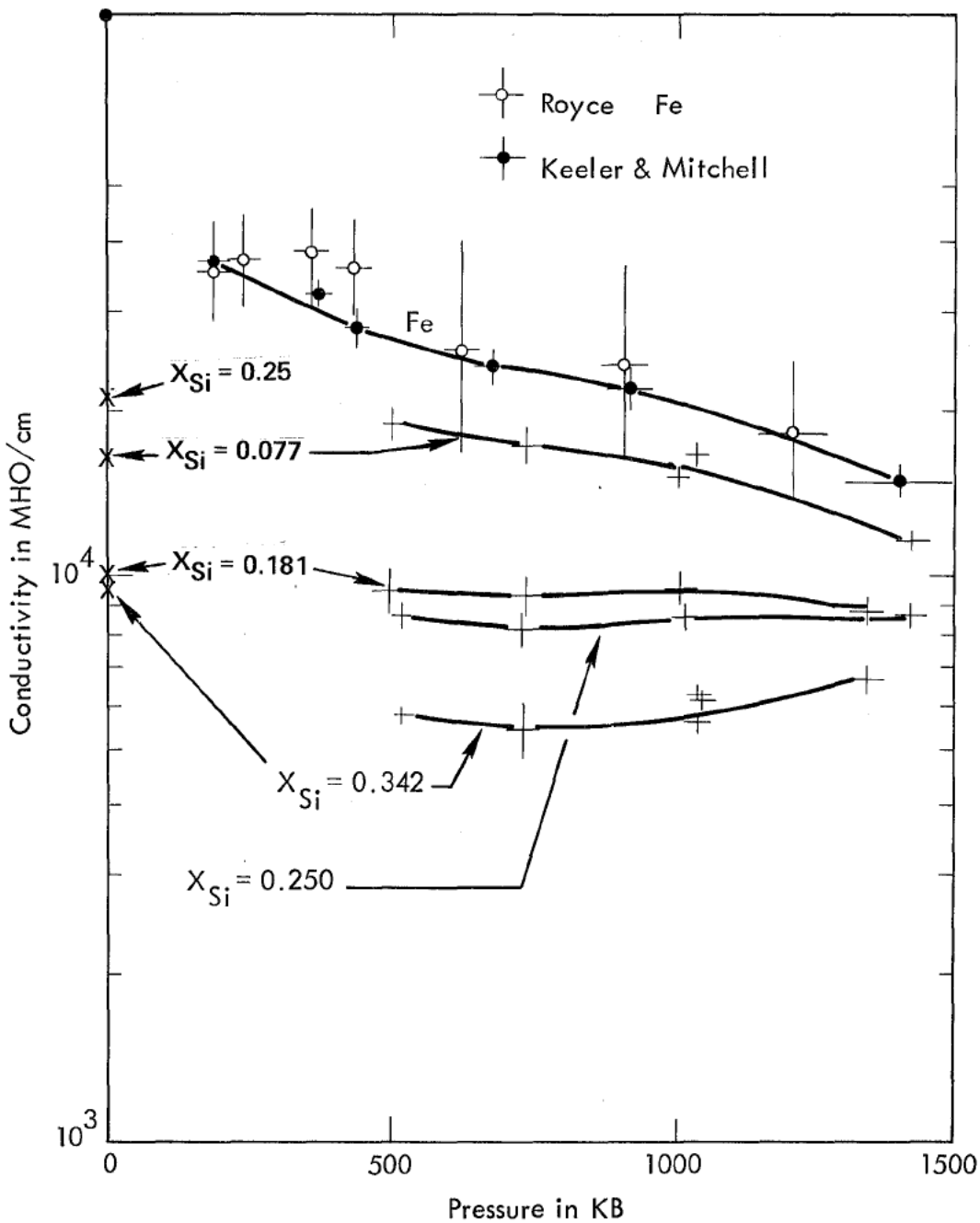


FIGURE 7.4 ELECTRICAL CONDUCTIVITY OF FeSi
AS A FUNCTION OF PRESSURE

three concentrations showed a surprisingly small dependence upon the (combined) pressures and temperatures investigated. The pressure and the temperature effects are compensating to a much larger degree than that observed in iron. For iron, the conductivity values derived from the magnetic measurements (Royce, 1968) are consierably less accurate than those obtained by direct measurements (Mitchell and Keeler, 1968; Keeler and Mitchell, 1969). This is easily explained by the fact that the conductivity is calculated from exponential eddy current decay oscilloscope traces where errors are inherently large.

A large difference existed in the initial conductivities of the four concentrations due to the combined effects of impurities, Si concentrations and grain sizes. The initial conductivity of the $X_{si} = 0.25$ samples was signficiantly higher than the others in spite of its large Si concentration and small grain size. This is attributed to the better control of impurities of other elements in the samples. The point to note is that, at even at the lowest shock pressure attained, the conductivities of the samples lined up in the order of the Si concentration. This confirms the supposition that the impurity and grain size effects become unimportant at pressures of 500 Kbars and above. Resistivity of the FeSi alloys as a function of pressure is shown in Figure 7.5.

At pressures below 1,000 Kbars, the expected $\frac{1}{T}$ behavior of conductivity is seen to hold. At the highest pressures reached, the behavior is not strictly followed (see Fig 7.6 and 7.7). This may be

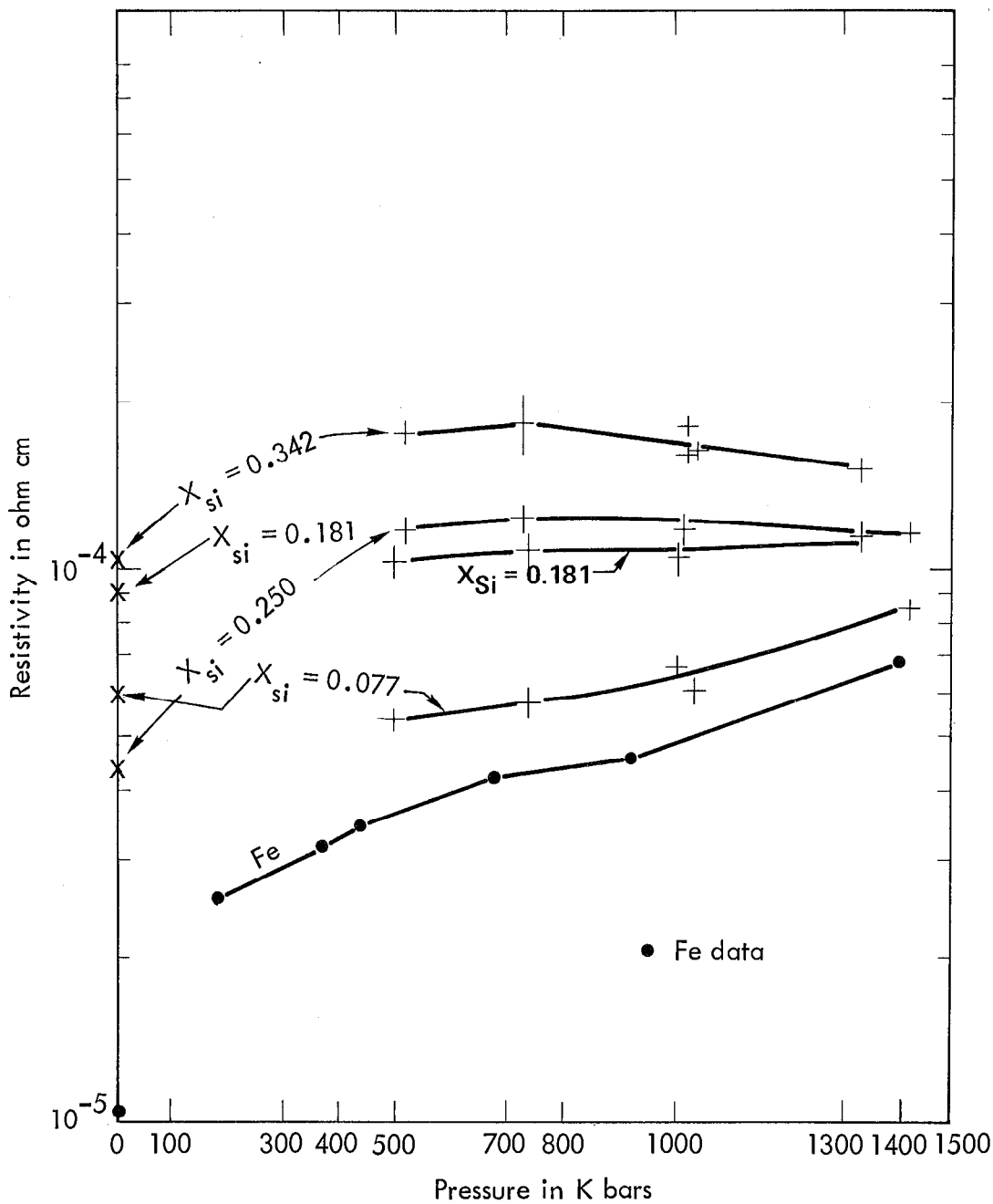


FIGURE 7.5 FeSi RESISTIVITY VS PRESSURE

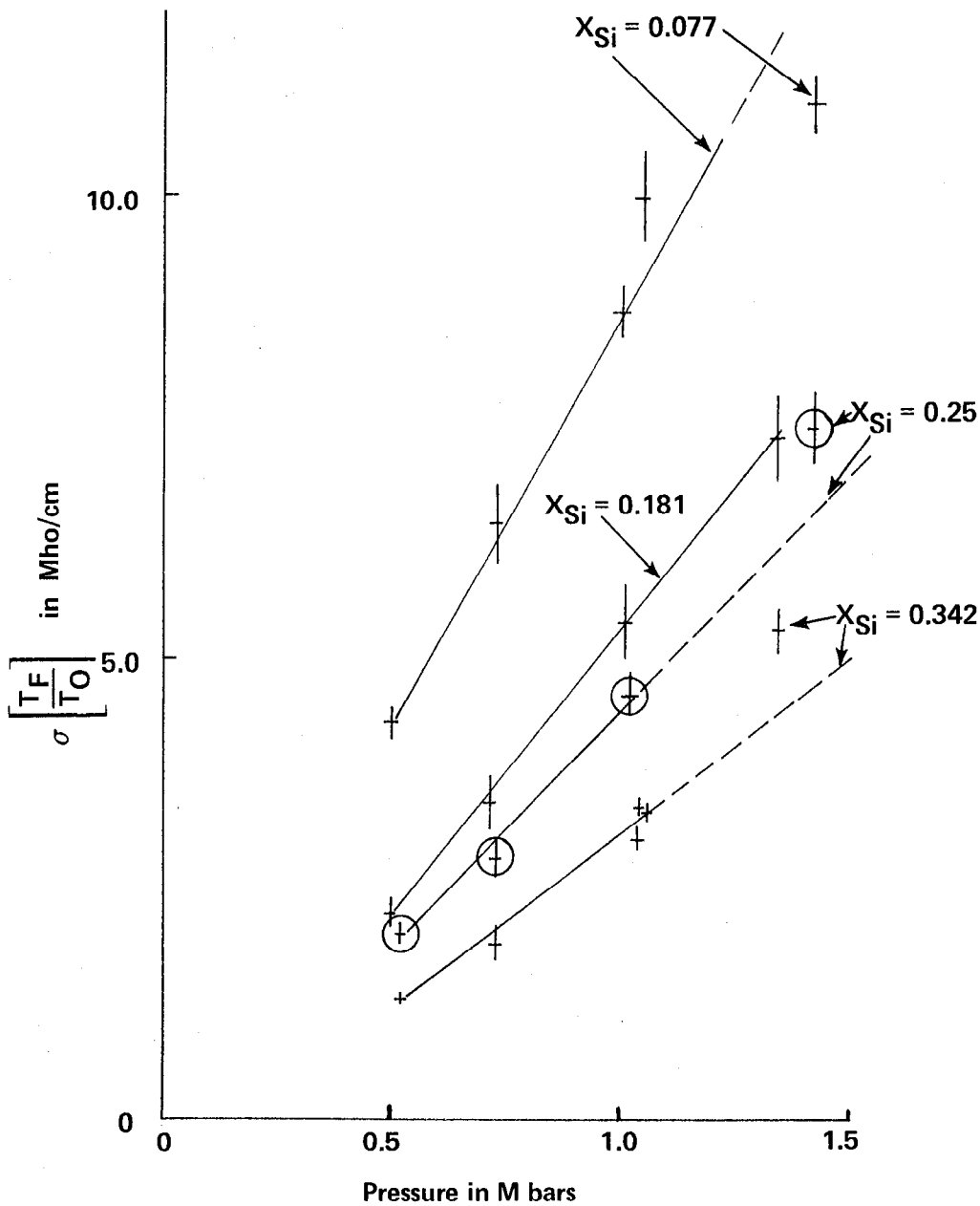


FIGURE 7.6 REDUCED CONDUCTIVITY VS PRESSURE

FIGURE 7.7 REDUCED CONDUCTIVITY VS REDUCED VOLUME

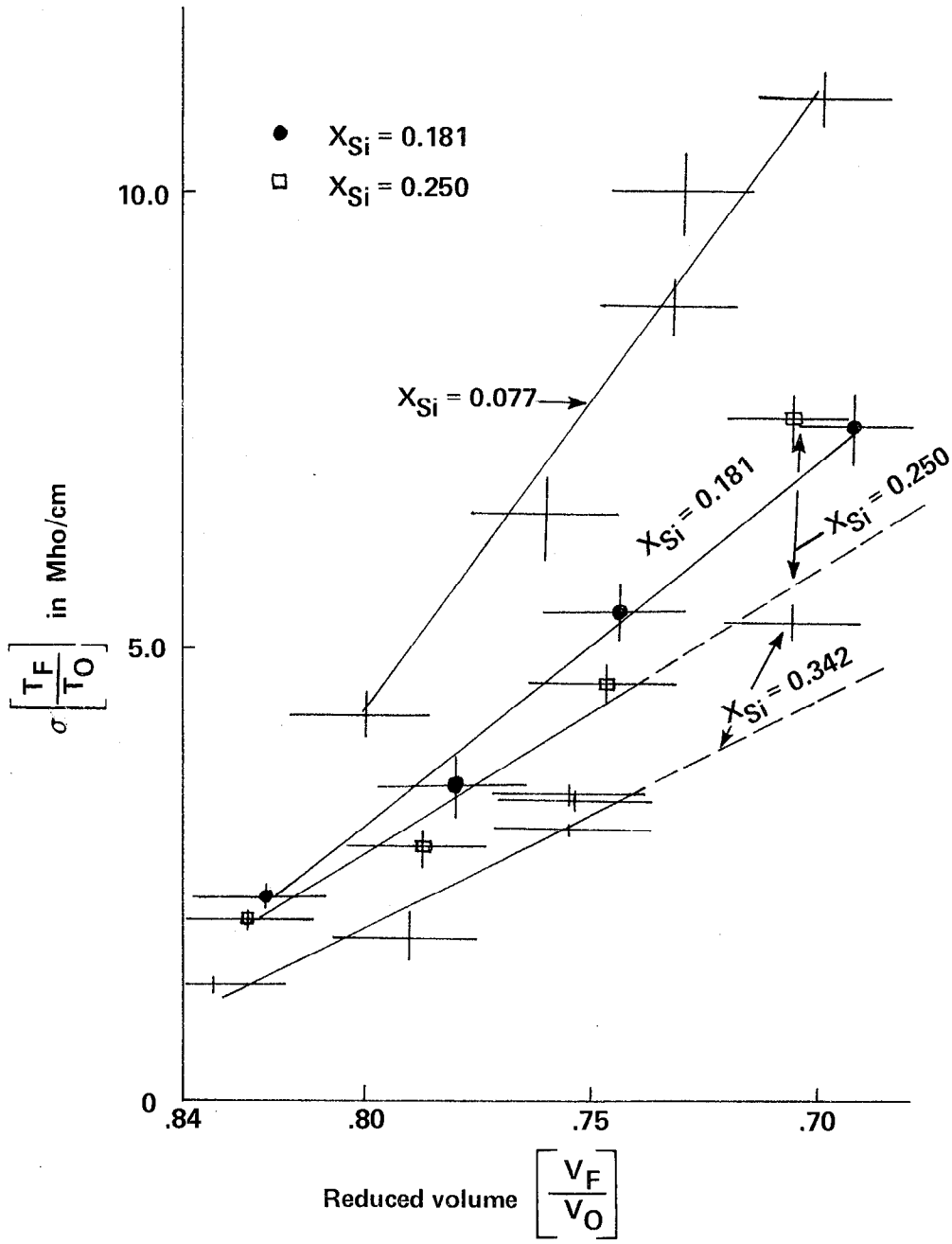

due to both the high temperatures reached and the close packing of the material wherein more electrons join the conduction band. Unfortunately, it is not possible to separate the effects of temperature and density (pressure).

Another explanation of the $\frac{1}{T}$ behavior of electrical conductivity at high pressures of $X_{si} = 0.25$ and $X_{si} = 0.342$ can be offered. Examination of Fig 7.6. reveals that straight lines can be fitted for the three highest pressures measured. This may be consistent with the $U_s$ vs $U_p$ behavior of $X_{si} = 0.342$ where a possible bend in the curve is seen. The lowest pressure points however do show complete demagnetization in contradiction with this possible explanation. The measurement at 521 Kbars had a particularly thin $X_{si} = 0.342$ sample and a good determination of the decay time (Table 7.5). On this basis, the alternative explanation is ruled out.

Another result is the convergence of the observed electrical conductivities of all four concentrations at high pressures as seen in Fig 7.4. The alloying effect of Si becomes less pronounced (in the spread of conductivities) as the pressure is increased. Correlation as a function of Si concentration is seen at the highest pressure to support the suggestion (explained in Section 5.1) that as the covalent bond between Fe and Si is broken, the conductivity is increased by the release of the bound Fe electron.

For completeness, all other high pressure electrical conductivity data of geophysical interest is shown in Fig 7.8 where pure iron and $X_{si} = 0.25$ data is shown for comparison. Iron nickel

FIGURE 7.8 ELECTRICAL CONDUCTIVITY DATA

OF GEOPHYSICAL INTEREST AS A FUNCTION OF PRESSURE

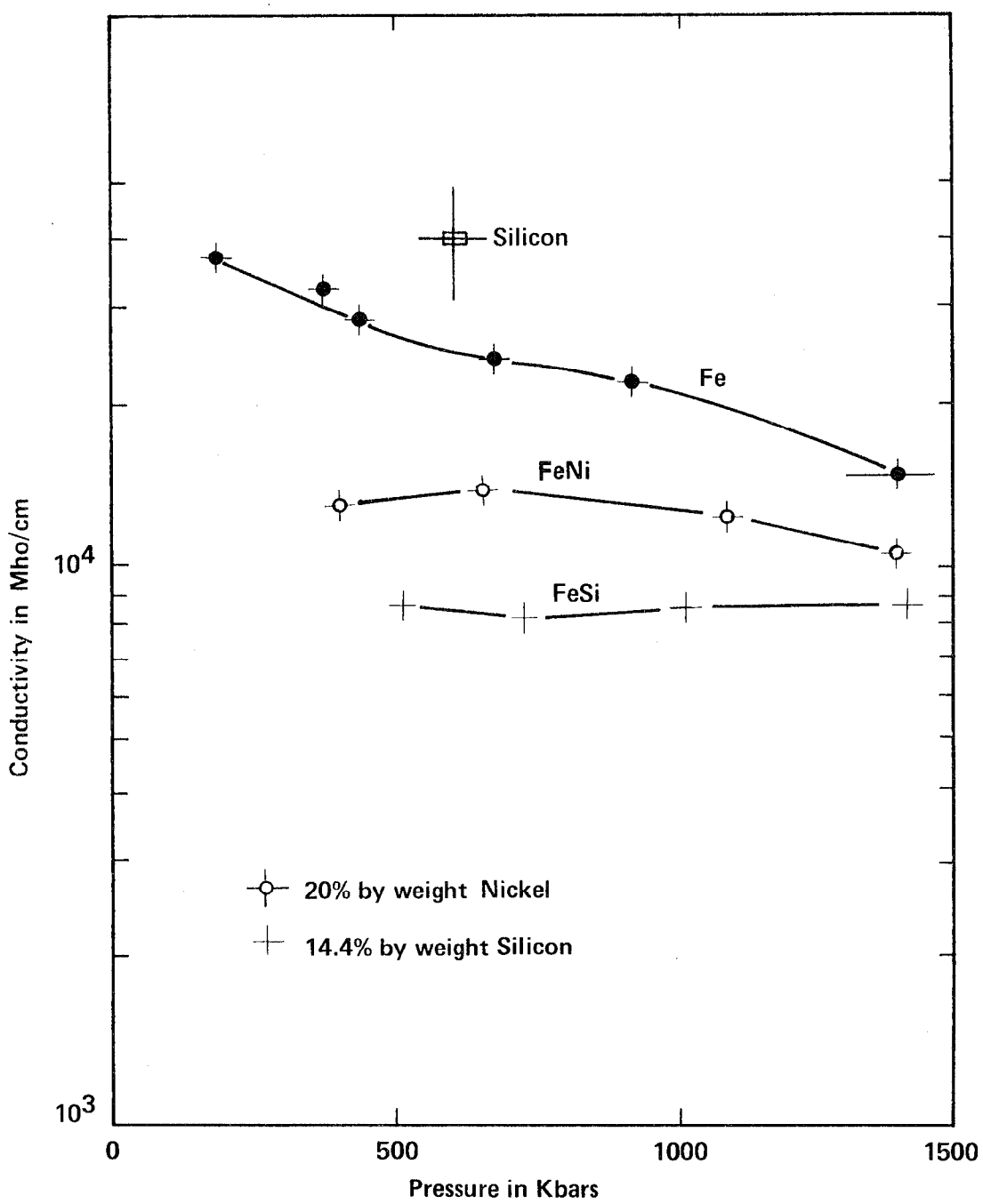

alloy data for Ni 20% by weight was obtained at LLL (Keeler, et al, 1971). One relevant data point was observed in a study of pure silicon shock induced solid state transformations (Mitchell and Matassov, 1970). The conductivity of silicon at 580 Kbars was measured to be $4 \times 10^4$ mho/cm $\pm$ 25% in the high pressure metallic phase, well above the Rayleigh line.

A significant source of error is a high frequency random noise ripple riding on top of the conductivity trace. This phenomenon was not observed on experiments with pure iron or iron-nickel (Mitchell, private communication). All efforts to electronically isolate and eliminate this noise ripple were not successful. The experimental accuracy of the measured conductivity varied from 3 to 13% and was directly attributable to the discussed sources of error (see Appendix A).

## 7.4 PHASE TRANSITION RATE

As we have seen in Section 3, the shocked stable state is reached in 10 to 20 nanosec within one solid phase. The question of the transition rate from the $\alpha$ to the hcp phase in FeSi alloys requires examination in order to establish that the final state is reached within 100 nanosec, the typical time to reach the final off Hugoniot state. Due to the same type of crystal structures and similar Hugoniots, the data on Fe (which is much more abundant) is used as well.

The first Hugoniot data to establish multiple wave profiles in Fe was taken by Minshall (1955). The method involved bare (unshielded)

pins and the samples in a vacuum (to avoid premature discharge of the pins by shocked air). The free surface movement as a function of time established an elastic precursor, a 130 Kbar (plastic) wave and a final wave in the high pressure phase. The very distinct wave velocities gave a transition time of less than 30 nanosec at 220 Kbars. Altshuler (1965) established that the metastable coexistence of the two phases exists between 130 and 330 Kbars. Above this pressure, the transformation is complete. This corresponds to the pressure defined by a Rayleigh line that is above the coexistence region of the two phases.

The experiments performed on seven FeSi alloys by Zukas, et al, (reviewed in Section 4) investigated the $\alpha$ to hcp phase transition.

The high pressure portion of the Hugoniot, above 320 Kbars (measured up to 480 Kbars), was in the single wave protion and the transition was complete for all of the Silicon concentrations. The Hugoniot measurements of the present work are in agreement. The electrical conductivity measurements were made well above this pressure.

The demagnetization and conductivity experiments also give direct indications of the phase transition rate. A method to measure shock induced demagnetization was developed at Lawrence Livermore Laboratory by Royce (1967, 1968). He used Fe magnetic samples that were biased to saturation by a magnetic field transverse to the shock velocity. Reduction in the magnetic flux was detected by pickup coils in another part of the magnetic circuit well behind the shock front.

He found complete demagnetization, within experimental error, of Fe at pressures between 300 and 1200 Kbars. The key to the transition rate lies in the fact that all of his measurements were made in the first 50 nanoseconds of shock arrival. Since the demagnetization was complete, one must conclude that the transition to the hcp state is complete within 50 nanoseconds. Work on Silectron (a commercial FeSi alloy of $X_{Si} = 0.058$) by Graham (1968) shows complete demagnetization within experimental error over the pressure from 240 to 420 Kbars. Below 240 Kbars, the demagnetization is incomplete. In fact the degree of demagnetization was proportional to pressure between 130 and 240 Kbars over a comparable measurement time.

Conductivity measurements of iron (Mitchell and Keeler, 1969; Keeler and Royce, 1970) show that the risetime of the demagnetization pulse is dependent on pressure in the two phase coexistence region. For instance, a rise time of 50 nanosec was measured at 175 Kbars. At high pressures the risetime becomes shorter and is typically 20 nanosec above 300 Kbars. The demagnetization risetimes found by the present work for the FeSi alloys are between 20 and 10 nanosec over the pressure range of 500 to 1400 Kbars.

Previous work on iron and FeSi alloys are in agreement that in the coexistence region of the $\alpha$ and hcp phase, the transition rate slows down as the shock pressure approaches the static transition pressure. It can be concluded, for the present conductivity measurements, that the phase transformation to the hcp phase is complete in a time that is short compared to the reverberation time required to reach the final state in which the conductivity is measured.

## 7.5 MELTING POINT

As indicated in the introduction, calculations of the melting point of pure iron at pressures equivalent to the Earth's core differ by a factor of two. Of the many theories proposed, two of them represent the most popular extreme beliefs.

The Lindemann melting law, proposed in 1910 and widely used today, is based on the classical treatment of lattice vibrations and melting is assumed when the amplitude of the vibrations is a fraction (approximately 1/2) of the lattice parameter. It is simply given as

$$T_m = C\ M\ \Theta^2\ V^{2/3} \qquad (7.3)$$

where M is the atomic weight, $\Theta$ is the Debye temperature, C is a constant which depends on the lattice geometry and V is the atomic volume.

The Kennedy equation was empirically derived by Kraut and Kennedy (1966) from melting points of a large number of metals up to pressures as high as 50 Kbars. It is

$$T_m = T_m^o\ (\ 1 + C'\Delta V/V\ ) \qquad (7.4)$$

where $T_m^o$ is the melting point at ambient pressure, C' is a constant peculiar to each metal and $\Delta V/V$ is the isothermal fractional decrease in volume.

The most recent experimental data (Liu and Bassett, 1975) on the melting point of iron extends the static data to 200 Kbars (all

previous data has been reported only up to 100 Kbars). When both theories are fitted to the experimental data and extrapolated to 3,300 Kbars (the inner-outer core boundary) their predictions differ by more than 2200°C. The hazardous extrapolation is shown in Figure 7.9.

The results of a Dugdale-McDonald formulation of the Grüineisen EOS derived from the iron Hugoniot have been plotted on the same graph (Grover, 1976 private communication). The effects on the specific heat by the free conduction electrons are clearly seen. It is interesting to note that, as of this date, no one has claimed to have determined the melting transition of iron using shock waves. It is not a trivial task because at the high pressures and temperatures, the observable bulk properties are seen to vary continuously. It is not only a question of reaching sufficiently high pressures. Russian workers have been reporting Hugoniot data on many metals for pressures ranging up to 5 to 10 Mbars since 1965.

The task of similarly extrapolating the melting temperatures of FeSi alloys, when there is no low pressure data, is left to those who make such extrapolation life's work. They should not forget to include a theory of the effect of alloying on the melting temperature.

## 7.6 SUGGESTED FUTURE WORK

The introduction of a two stage gas gun has extended the practical attainment of plane shock waves by a factor of two. It is now practical to suggest that further experiments of geophysical interest

be conducted. The measurements fall into two categories, namely the measurement of electrical conductivity and the determination of melting. It is suggested that investigation of iron and iron alloys (such as iron silicon and iron sulfur) be pursued at pressures ranging from the outer to the inner core.

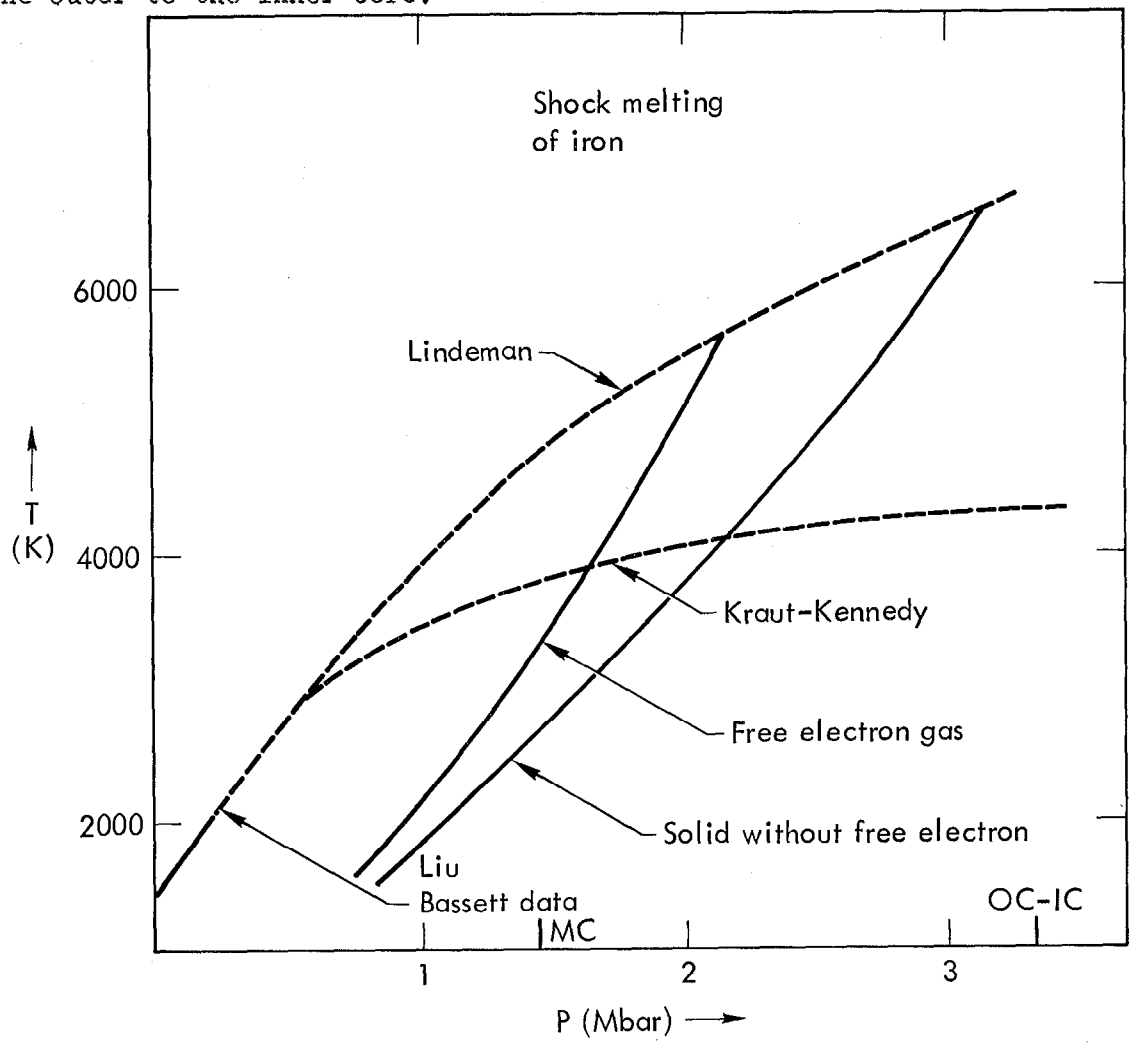


FIGURE 7.9 MELTING POINT EXTRAPOLATIONS OF

Fe AND TEMPERATURE CALCULATIONS

ALONG THE Fe HUGONIOT

## 8.0 APPLICABILITY TO THE EARTH'S CORE

Based upon the measured conductivity of FeSi alloys, speculative calculations can be made about the Earth's core. The electrical conductivity, just inside the outer liquid core, depends upon the melting point, Tm, of the core material. If we choose it to be mostly FeSi ($X_{Si}$ = 0.25), then we need only adjust the measured conductivity at 1,400 Kbars from 2,500°K to Tm. The actual value of Tm probably lies between two extremes, that calculated by the Kraut Kennedy empirical relationship (demonstrated up to 100 Kbars) and that calculated by the Lindeman theory. Assuming the conductivity to be inversely proportional to temperature, we get $\sigma m$ = 7.30 mho/cm for Tm = 3,000°K and $\sigma m$ = 4.87 mho/cm for Tm = 4,500°K. No change in the conductivity upon melting at high pressure is assumed. The assumption is supported by the experimental results at one atmosphere (Baum, et al, 1967). Brideman (1964) found the pressure dependence of electrical conductivity of liquid metals to be similar to that of solids. For a particular value of Tm, the total uncertainty (experimental error, remaining uncertainty in concentration, and additional alloying effects of minor impurities) is estimated to be less than 20%. These values fall well within the geophysical constraints discussed in Section 2.3. Table 8.1 summarizes the deduced values of electrical conductivity quoted in the literature.

The thermal conductivity, $\kappa$, of the FeSi core material is found by the Wiedemann-Franz law to be

$$\kappa = L \quad \sigma m \, Tm = L \, \sigma_{2,500} \, ( 2,500/ T_m ) \, Tm = 0.13 \text{ cal/sec deg cm}$$

TABLE 8.1

ELECTRICAL AND THERMAL CONDUCTIVITY OF

THE EARTH'S OUTER CORE

| $\sigma$ X $10^{-3}$ mho/cm | $\kappa$ cal/sec deg cm | Q X $10^{-19}$ erg/sec | Reference |
|---|---|---|---|
| 1.67 to 10 | 0.029 to 0.20* | 3.0 (upper limit) | Gardiner and Stacey, 1971 |
| 1.67 to 6.7<br>Uses 3.3 | 0.029 to 0.116*<br>Uses .058 | 3.9 (upper limit) | Stacey, 1972 |
| 5 to 10 | 0.10 to 0.20* | ---- | Jain and Evans, 1972 |
| Uses Jains and Evans | 0.13 | 2.7 (upper limit) | Frazer, 1973 |
| ---- | ---- | 1.3 to 3.0 | Verhoogen, 1961 |
| ---- | 0.10 | 8.4 | Verhoogen, 1973 |
| ---- | ---- | 2.0 | Murthy and Hall, 1972 |
| 7.30 at 3000°K<br>4.87 at 4500°K | 0.13 | ---- | This work |

*Calculated, based upon Wiedeman - Franz Law

where $L = 5.85 \times 10^{-9} \frac{\text{cal ohm}}{\text{sec deg}^2}$ is the Lorenz number (Kittel, 1966). This should be a reasonable assumption at high pressures, especially in view of experiments with liquid metals at one atmosphere, where the relationship has been shown to hold (Rice, 1970). Recently published values of thermal conductivity are also shown in Table 8.2. The important point to note is that, to first order, the electrical conductivity scales as 1/T at a given pressure. Therefore, the thermal conductivity varies only as second order in temperature. This means that the calculated value of thermal conductivity is very reliable.

The heat transfer calculations from the outer core depend on:

a. Thermal conductivities of the mantle and core

b. Temperature in the mantle

c. Nature of the mantle-core interface

d. Melting temperatures of the outer and inner core materials (and the pressure dependence of them)

e. Nature and extent of the assumed heat sources.

Temperatures in the mantle at the mantle-core interface have been deduced recently (Tozer, 1967; Wang, 1972; Cook, 1973) with reasonable agreement. A value of 3300° ± 800°K is representative, when heat transfer in the mantle includes conduction and radiation. The density gradient within the thin layer D" (Ref Section 2.1.1) just above the outer core may maintain a high and non-convecting conductive temperature gradient. The large difference in the thermal conductivity between the mantle (insulator or semiconductor) and the

TABLE 8.2

THERMAL CONDUCTION GRADIENTS IN THE

CORE FOR $\kappa$ = 0.13 CAL/SEC DEG CM

| $Q \times 10^{-19}$ erg/sec | Remarks | Ti - Tc °K | $-(\frac{\partial T}{\partial R})c$ °K/km | $-(\frac{\partial T}{\partial R})i$ °K/km |
|---|---|---|---|---|
| 8.4 | Verhoogen (1973) | 1216 | 0.94 | 0 |
| 3.9 | Stacey (1972) | 564 | 0.44 | 0 |
| 3.0 | Gardiner and Stacey (1971) | 434 | 0.34 | 0 |
| 2.7 | Frazer (1973) | 391 | 0.30 | 0 |
| 2.0 | Murthy and Hall (1972) | 289 | 0.22 | 0 |
| 0.8 | Verhoogen (1961) (Slow Crystallization) | 651 | 0.10 | 0.73 |

$r_c = 3.47 \times 10^8$ cm, $r_i = 1.22 \times 10^8$cm

core (metal) and the observed velocity gradient in the core (Ref. Section 2.1.1) near the mantle-core boundary further support the idea that a large thermal gradient exists between the mantle and the core. The gradient is estimated to be as large as 1200°K. Therefore, the temperature of the core near the mantle-core interface is anywhere between 3000° and 4500°K in good agreement with the uncertainty in the melting temperature of the core mix. The melting temperature of the inner core is also very uncertain (Ref Section 2.2.3 and 7.5). Thus, the general heat transfer problem has ill defined boundary conditions.

In spite of the above listed handicaps, the consequences of the three most plausible energy sources that may drive the geomagnetic dynamoes can still be examined. The crucial test of heat driven dynamoes is the comparison between the conduction gradient and the adiabatic gradient. If the conduction gradient inside the outer core is less than the adiabatic gradient, then steady state convection is not possible due to heat sources (convection is then a less efficient process of heat transfer than conduction). This situation is now examined in more detail.

The heat source proposed for the FeS model of the outer core is the radioactive decay of $K^{40}$ (Lewis, 1971; Murthy and Hall, 1970 and 1972). The FeS in the core (with potassium) is attributed by these authors to the lower required melting temperature of FeS in comparison with FeSi by arguing that the eutectic point shifts to $X_S = 0.23$ at high pressures the (melting temperature at 1 atmosphere and 15% by weight is 1250°C for FeSi and 1330°C for FeS.

The eutectics occur at $X_{si} = 0.30$ and 1180°C; $X_s = 0.44$ and 988°C. The FeSi eutectic may also shift to $X_{si} = 0.25$ by a similar argument) and not because potassium cannot be introduced into the melt of FeSi (Murthy and Hall, 1972). In either case, Murthy and Hall assume that 3/4 of the Earth's supply of potassium has been segregated into the core. The concentration of potassium of 375 ppm in the outer core and the relative abundance of $K^{40}$ of $1.2 \times 10^{-4}$ to that of stable K, lead to a present day heat generation rate (Q) of $2 \times 10^{19}$ erg/sec. This value is more than adequate on the basis that $5 \times 10^{16}$ to $2 \times 10^{17}$ erg/sec (Malkus, 1968; Verhoogen, 1973) is required to maintain the Earth's magnetic field (the efficiency of the heat engine is on the order of 2%. Verhoogen recently used a value of $Q = 8 \times 10^{19}$ erg/sec in contrast to his previous $Q = 1.3$ to $3.1 \times 10^{19}$ erg/sec. This corresponds to four times the assumed concentration of K used by Murthy and Hall, or three times the Earth's supply of K. Even with the unrealistically high Q, the conduction thermal gradient drops to zero at the inner core whereas the adiabatic gradient must remain finite (i.e., the adiabatic gradient is $(\partial T/\partial r)_S = \gamma g T / \phi^2$ and none of the variables are zero at the inner core boundary). This means that for any large but finite Q, the inner part of the outer core cannot participate in convection. How large the non-participating region is depends upon Q and the adiabatic gradient. Stacey (1972) observed that had he used a conductivity larger than $\sigma = 3.3$ mho/cm and $\kappa = 0.058$ with $Q = 3.9 \times 10^{19}$ erg/sec, the estimated conducted heat flux (without any allowance for convection) would have been

correspondingly larger. This would present a serious problem of disposing up to 30% of the total (observed) geothermal flux as well as necessitating a re-examination of the heat transport through the mantle (Clark, 1971).

Verhoogen (1973) bases his estimates of the adiabatic gradient on a parametric fit of seismic data and concludes that the adiabatic gradient at the outer core radius lies somewhere between 0.7, 0.86, 1.20, 1.45, 1.51 and 1.83°K/km. He notes that since there is no unique solution, solutions can be found compatible with convection (based upon his estimate that the thermal conduction gradient at the outer core is 1.2°K/km). Independent calculations by Stacey (1972) give 0.89°K/km and 0.033°K/km as the adiabatic thermal gradient at the outer and inner core. Additional adiabatic gradients are shown in Table 8.3.

The solution of the heat conduction equation for distributed heat sources in the outer core is given (Verhoogen, 1973) as

$$\frac{dT}{dr} = -1/3\left(\frac{\beta\bar{\rho}}{\kappa}\right) r + 1/3\left(\frac{\beta\bar{\rho}}{\kappa}\right)\frac{r_i^3}{r^2} \qquad (8.1)$$

and

$$T_i - T_c = 1/6\left(\frac{\beta\bar{\rho}}{\kappa}\right)(r_c^2 - r_i^2) - \frac{1}{3}\left(\frac{\beta\bar{\rho}}{\kappa}\right)r_i^2\left(1 - \frac{r_i}{r_c}\right) \qquad (8.2)$$

where $\beta$ is the average rate of heat generation per unit mass, $\bar{\rho}$ is the average density, r is a radius, $\kappa$ is the thermal conductivity, and the subscripts i and c refer to variables at inner and outer core radii. The parameter that has been least certain is $\kappa$ because

the thermal conductivity had to be consistent with the uncertain limits of electrical conductivity imposed by geophysical arguments (see Table 8.1). On the basis of these equations, the conductive thermal gradients at the outer core/mantle and outer/inner core interface and the temperature difference between the inner and outer core are given in Table 8.2 for a variety of heat production rates, Q, using $\kappa$ = .13 cal/sec deg cm.

A definite conclusion is reached that, with a conductive thermal gradient as large as 0.44°K/km and 0 at the core/mantle and inner/outer core, convection due to radiative heat sources is not possible. This conclusion is reached by using the thermal conductivity gradient calculation based upon the experimental values of electrical conductivity measured in this work.

The second heat driven dynamo mechanism relies upon the slow crystallization at the inner core boundary to release $Q = 8 \times 10^{18}$ erg/sec. Verhoogen (1961) also solved this heat conduction problem. Calculations using $\kappa$ = 0.13 cal/sec deg cm give a thermal conduction gradient of 0.10°K/km and 0.73°K/km at the outer core/mantle and inner/outer core (see Table 8.2). This implies that some convection may be possible near the inner core.

An elementary calculation of the adiabatic gradient is made starting with two temperature extremes of 2915°K and 4577°K at the outer core/mantle interface. A comparison with the thermal conduction gradient is made in Table 8.3. The corresponding fraction of the core volume that can participate in thermally induced convection is 12.4% for $T_c$ = 2915°K and 6.4% for $T_c$ = 4577°K. The

TABLE 8.3

COMPARISON OF ADIABATIC AND CONDUCTION GRADIENTS

| | ADIABATIC GRADIENTS | | CONDUCTION GRADIENT* |
|---|---|---|---|
| | Tc = 2915°K | Tc = 4577°K | |
| r km | $-(\frac{\partial T}{\partial r})_s$ °C/km | $-(\frac{\partial T}{\partial r})_s$ °C/km | $-(\frac{\partial T}{\partial r})$ °C/km |
| 3493 | .67 | 1.02 | .10 |
| 3171 | .58 | .88 | .12 |
| 2771 | .50 | .76 | .16 |
| 2371 | .43 | .65 | .22 |
| 1971 | .36 | .54 | .32 |
| 1660 | .30 | .45 | .44 |
| 1220 | .20 | .31 | .73 |
| | Ti = 3631°K | Ti = 5659°K | |

Tc = 2915°K adiabat intersects conduction gradient at 1,900 km radius

Tc = 4577°K adiabat intersects conduction gradient at 1,640 km radius

*Due to solidification of the inner core, $Q = 0.8 \times 10^{19}$ erg/sec,

$$-\frac{\partial T}{\partial r} = \frac{Q}{4\pi\kappa}\left(\frac{1}{r^2}\right), \quad \text{and}$$

$$Ti - Tc = \frac{Q}{4\pi\kappa}\left(\frac{1}{r_i} - \frac{1}{r_c}\right).$$

small size of the convection volume rules out the crystallation heat source as the prime mechanism for the generation of the earth's magnetic field.

The third mechanism, as proposed by Malkus (1968), relies upon the difference between the dynamic ellipticity of the whole earth and the core to cause turbulent flow in the outer core. The estimated total work done on the core by the mantle is $2.3 \times 10^{17}$ erg/sec. The precessional torques responsible for the flow are due to the non-conserved component of the angular momentum of the Earth in the plane of the ecliptic. Malkus has estimated that, at present, this component of the angular momentum is sufficient to maintain the geomagnetic field for many Earth lifetimes. It is interesting to note that the dynamo dissipation might have exceeded $3 \times 10^{19}$ erg/sec at an early time in the Earth's history when the moon was closer to the Earth. The important feature of this mechanism is that it can induce turbulent flow in a liquid and does not require an adiabatic gradient to be less than the thermal conduction gradient. The theoretical model of turbulent flow caused by precessional torques has been confirmed in a laboratory experiment by Malkus. Both small wavelike instabilities and large finite amplitude instabilities were observed.

The third mechanism is also more likely to be consistent with the observations that Mercury has a magnetic dynamo (Ness, et al, 1974) and the Moon is supposed to have had one as well (Runcorn, 1972). To conclude, the values of the measured electrical conductivity of FeSi alloys are fully compatible with geophysical requirements

of the precessionally driven dynamo and the estimates of thermal conductivity of the Earth. The sound velocity and density calculations, based upon Hugoniot data, are in full agreement with present day models of the outer core.

## 9.0 ACKNOWLEDGEMENTS

I am indebted to Lawrence Livermore Laboratory, the members of S-Division for their theoretical and experimental counsel, to the personnel of the Precision Machine Shop and Electronics Shop for helping me learn their skills, and to the personnel at Site 300 for their diagnostics aid and for blowing up my experiments. In particular, I would like to express my deep appreciation to R. N. Keeler for suggesting the work, providing the opportunity and support for the experiments, arranging for a leave of absence from my employer in order to reduce the data and for persistently encouraging me to finish this work. I am also deeply thankful to A. C. Mitchell who gave me essential experiment insights, guidance and technical suggestions. I would also like to thank R. Borg for providing the opportunity for me to grow the crucial conductivity samples and to perform the metallographic analysis, Q. Johnson for providing help in characterizing the initial state of my samples, and R. Grover for helping with the computer code GRAY, and allowing me to quote his unpublished theoretical calculations of the melting of iron. Special thanks are in order to M. Schneider for her secretarial help without which this work would not have been finished. My sincere gratitude to the U.S. Air Force and the Department of Applied Science, U.C. Davis-Livermore who joined

together to make this all possible. Apologies are in order to all the individuals who helped me and are too numerous to list. Last, but not least, I am grateful to my family for providing unfailing support, for putting up with a part-time husband and father, and never complaining about the burden.

## 10.0 SUMMARY OF RESULTS

The Hugoniots of FeSi alloys, $X_{si}$ = 0.077, 0.181, and 0.342, have been determined for pressures between 100 and 1500 Kbars. Linear fits of the $U_s$ vs $U_p$ data showed less scatter than those reported by Balchan and Cowan (1966) as well as Kormer and Funtikov (1965). The temperature along the Hugoniot and the 0°K isotherm (cold compression curve) were calculated with the help of a computer code to complete the equation of state of these alloys. The calculations were based on the Dugdale-MacDonald formulation of the Grüneisen description of solids and included the thermal exitation of electrons.

The seismic velocity, density and pressure of the most probable concentration, $X_{si}$ = 0.25, were calculated along an extrapolated adiabat from 1,400 Kbars to 3,200 Kbars. The results fall within the narrow range of acceptable Monte Carlo solutions for the outer core published by Press (1970 and 1972).

A demagnetization pulse was observed on every conductivity experiment. The magnitude of this pulse has been observed to be on the order of 50 times as large as the measured conductivity traces of the initial and final states. The shape and the relaxation of the pulse has been derived theoretically and is in agreement with observation.

The electrical conductivity of four FeSi concentrations, $X_{si}$ = 0.077, 0.181, 0.25, and 0.342, has been measured in the pressure range of 500 to 1400 Kbars and the accompanying temperature range of 600°K to 2500°K. The off-Hugoniot volume and temperature corrections, as calculated by a first order calculation and by the computer code GRAY, agreed to better than 0.6% over the entire pressure range. The conductivity of the lowest Si concentration followed the behavior of pure iron (see Fig 7.4). The conductivity of the other three concentrations showed a surprisingly small dependence upon the (combined) pressures and temperatures investigated. The pressure and temperature effects are seen to compensate each other to a much larger degree than that observed in iron.

The impurity and grain size effects become unimportant at pressures of 500 Kbars and higher. The alloying influence of Si becomes less pronounced (in the spread of conductivities) as the pressure is increased. The conductivities of the alloys are within a factor of three of pure iron ( $\sigma = 17.5 \times 10^3$ mho/cm) at 1400 Kbars. For $X_{si}$ = 0.077, 0.181, 0.25, and 0.342, the electrical conductivity was found to be 11.75, 8.75, 8.70, and $6.65 \times 10^3$ mho/cm at 1422, 1340, 1422 and 1340 Kbars and 2740, 2483, 2518, and 2339°K.

The value of the electrical conductivity of $X_{si}$ = 0.25 at liquid core temperature depends upon the particular model of the melting curve used. Allowing for a 1500°K spread in the uncertainty of the melting temperature, the electrical conductivity just inside

the outer core is estimated to be from 7.30 to 4.87 X $10^3$ mho/cm, well within the limits required by dynamo theories and previous estimates. For a particular value of the temperature, the total uncertainty in conductivity is estimated to be less than 20%. The associated thermal conductivity (for the same 1500°K uncertainty) is found to be 0.13 cal/cm sec deg, independent of the melting temperature. This value is in full agreement with the thermal conductivities quoted in the literature.

The heat transfer calculation from the outer core is dependent upon the assumed nature of the mantle-core interface, the thermal conductivity of the mantle, the assumed temperatures at the inner and outer core and the nature and extend of the assumed heat sources present. In spite of the uncertain boundary conditions, comparison is made of the three most probable energy sources for the geomagnetic dynamo. It is concluded that the thermal conductivity value is fully compatible with the dynamo which is driven by precessional torques and not compatible with the dynamo driven by convective heat. Thus the radioactive energy source is ruled out by the electrical conductivity measurements of FeSi alloys. The latent heat source (heat released by the slow solidification of the inner core) is ruled out because the convection (which occurs only near the inner core) is insufficient to drive a dynamo efficient enough to maintain the Earth's magnetic field.

## APPENDIX A: SAMPLE CALCULATIONS AND ERROR ANALYSIS

### A.1 FeSi HUGONIOT

The Hugoniot of the FeSi alloys was obtained using standard impedance matching techniques described in Chapter 3. The shock and free surface velocities were calculated from the measured distances of the sample thickness, flash gaps and shims and the transit times between flashes as recorded on film. The equations used were

$$U_s = \frac{T}{\frac{M}{W} - \frac{S_1}{U^1_{sal}} + \frac{g_1}{U_{fs\ bp}} - \frac{g_2}{U^1_{fs\ al}}} \tag{A.1}$$

and

$$U_{fs} = \frac{D + (S_1 - S_2) + (g_2 - g_3)}{\frac{M}{W} + \frac{(S_1 - S_2)}{U^1_{s\ al}} + \frac{(g_2 - g_3)}{U^1_{fs\ al}}} \tag{A.2}$$

where T is the sample thickness in mm, M is the distance between flashes in mm, W is the constant writing speed in mm/micro sec, $S_i$ is the thickness of the ith aluminum shim in mm, $g_i$ is the ith argon gap distance in mm, $U^1_{sal}$ and $U^1_{fsal}$ are the shock and free surface velocities of the aluminum shims, $U_{fsbp}$ is the free surface velocity of the baseplate, and D is the free surface gap distance

in mm. On each shot, both the baseplate and the impedance standard were chosen to be the same material (either brass or aluminum). First, $U_{fs}$ of the standard was calculated by successive iterations. The small correction terms involving the velocities in the aluminum shims were obtained by an initial estimate of $U_{fs}$ and impedance matching. Once convergence was obtained for $U_{fs}$, $U_s$ of the standard was found using the properly determined values of $U_{fsal}$, $U_{sal}$, and $U_{fsbp}$. The typical combined errors in $U_s$ were between 0.5% and 1% after correction fot tilt.

Tilt corrections were applied only if the shock arrival time on the base plate around the impedance samples and around the Hugoniot samples differed by more than 5 nsec. The corrections were somewhat subjective in order to compensate for the distortion in the planarity of the shock wave between the various locations. The corrections were basically a balancing of values around the Hugoniot sample. The deviations from planarity were always seen to be a function of radius away from the center of the experiment. It is for this reason that the location of the conductivity samples and the impedance standards for the conductivity measurements were always located at equal distances from the center of each experiment.

A graphical solution as discussed in Section 3 was used to find $U_p$ of the unknown using the release adiabat of the impedance standard. This was easily accomplished because the release adiabats were accurately reproduced on custom made french curves. The $U_p$ vs P and $U_s$ vs $U_p$ graphs used in all calculations were intentionally

oversize (2 1/2 feet by 5 feet) in order to reduce the errors due to the graphical method to be less than 0.5%. The resultant errors in $U_p$ were on the order of 1%. The pressure and relative volume were directly found using

$$P = \rho_o U_s U_p \tag{A.3}$$

and

$$\frac{V}{V_o} = ( 1 - U_p/U_p ) \tag{A.4}$$

The resultant errors in P and $V/V_o$ were on the order of 1.5% since $U_s$ and $U_p$ were independently determined.

## A.2 IMPEDANCE STANDARD ON CONDUCTIVITY EXPERIMENT

The shock velocity of the impedance standard is determined from the measured shock transit time and the thickness of the sample. The transit time was calculated for each pair of pins, one on the base plate and the other on the impedance sample. The three sets of transit times were then averaged. This eliminated any tilt across the sample. The shock velocity and its error are simply found by

$$U_s = \frac{d \pm \Delta d}{t \pm \Delta t} = \frac{d}{t} \pm \frac{d}{t}\left[\left(\frac{\Delta d}{d}\right)^2 + \left(\frac{\Delta t}{t}\right)^2\right]^{1/2} \tag{A.5}$$

where $d \pm \Delta d$ is the thickness of the sample and its uncertainty and $t \pm \Delta t$ is the shock transit time and its uncertainty. For example, on shot 1, the shock velocity of the $Al_2O_3$ shock impedance sample is

$$U_s = \left[\frac{6.6458 \pm .0017}{0.6221 \pm .0020}\right] = 1.0683 \pm 10.683 \left[6.54 \times 10^{-8} + 1.03 \times 10^{-5}\right]^{\frac{1}{2}}$$

$U_s = 10.683 \pm .034$ mm/ $\mu$ sec

Both $U_p$ and P were found graphically as discussed in Sections 3 and A.1. Comparison of the shock arrival time on the baseplate around the impedance standards and the conductivity samples confirmed that tilt was not significant because the samples were equidistantly located with respect to the center of the experiment.

Since $U_p$ was determined by a graphic solution with a known Hugoniot, its uncertainty was taken conservatively as a nominal 1.5% rather than the usual 1%. The uncertainty in the pressure is

$$\frac{\Delta P}{P} = \left[\left(\frac{\Delta \rho_0}{\rho_0}\right)^2 + \left(\frac{\Delta U_s}{U_s}\right)^2 + \left(\frac{\Delta U_p}{U_p}\right)^2\right]^{1/2} \tag{A.6}$$

because of the independent data sources. Continuing the calculation for Shot 1 gives

$$\frac{\Delta P}{P} = \left[\left(\frac{.0132}{3.8416}\right)^2 + \left(\frac{.034}{10.683}\right)^2 + (0.015)^2\right]^{1/2}$$

$$= \left[11.8 \times 10^{-6} + 10.1 \times 10^{-6} + 225 \times 10^{-6}\right]^{1/2}$$

$$= 1.6\%$$

## A.3 OFF-HUGONIOT STATE

The off-Hugoniot states reached in the conductivity experiments were calculated following the method described in Section 3.4. As seen on Figures 3.8 and 3.9 the final pressure $P_F$ equals $P_1$.

In order to find the final volume $V_F$, selected isentropes and the Hugoniot were followed through the reverberations to the final state with the help of the computer code GRAY. Similarly, a first order calculation using the graphical method and a hand calculator was performed. The results for $X_{si} = 0.25$ are shown in Table A.1. The agreement was better than the accuracy of the data! The uncertainty in the final volume is slightly larger than that found in Section A.1, because the uncertainty in $U_p$ was assumed to be 1.5%. The final volume uncertainty is less than 2%.

The final temperature could now be easily approximated by calculating it along an isentrope from the Hugoniot (point 2) to point 3 in Fig 3.9. Integrating eq (3.27), with the reasonable assumption that $\gamma$ (v) is approximately a constant in the vicinity of the calculation, gives

$$T_F = T_H \left( \frac{V_H}{V_F} \right)^{\overline{\gamma}} \tag{A.7}$$

where $\overline{\gamma}$ is the average $\gamma$ (v) taken over the interval $V_H$ to $V_F$. Since the temperature calculation is based upon a model of the solid, the uncertainty in the temperature is significantly more model dependent than any error analysis of the present method used.

TABLE A.1

TWO CALCULATIONS FOR OFF-HUGONIOT VOLUME

| Shot | Pressure Kbars | GRAY $V_F$ $cm^3/gm$ | FIRST ORDER $V_F$ $cm^3/gm$ | Difference |
|---|---|---|---|---|
| 5 | 733 ± 23 | .10988 | .1096 | .25% |
| 7 | 521 ± 15 | .11502 | .1150 | .02% |
| 9 | 1422 ± 28 | .09890 | .0983 | .61% |
| 11 | 1019 ± 20 | .10455 | .1040 | .52% |

## A.4 ELECTRICAL CONDUCTIVITY

The electrical conductivity of the shocked state $\sigma_1$, is found by changing equation 5.2 by the compression factor $(V_F/V_o)$, This gives

$$\sigma_1 = \frac{L}{R_1 \; X \; Z \left(\frac{V_F}{V_o}\right)} \tag{A.8}$$

The final resistance $R_1$ is found from equation 7.2 by measuring the displacement of the scope traces before the shock and after the demagnetization current has decayed. The calibration of each oscilloscope was checked for linearity over the range of voltages seen and deviations of less than 1% were ignored. The final resistance is simply

$$R_1 = R_o \left(\frac{v_1}{v_o}\right) = R_o \left(\frac{\ell_1}{\ell_o}\right) \tag{A.9}$$

where $\ell_1$ and $\ell_o$ are the scope trace displacements from the zero volt baseline established before the experiment.

The error in the conductivity can be expressed as

$$\frac{\Delta\sigma}{\sigma} = \left\{ \left(\frac{\Delta L}{L}\right)^2 + \left(\frac{\Delta R}{R}\right)^2 + \left(\frac{\Delta X}{X}\right)^2 + \left(\frac{\Delta Z}{Z}\right)^2 + \left(\frac{\Delta V_o}{V_o}\right)^2 + \left(\frac{\Delta V_F}{V_F}\right)^2 \right\}^{1/2} \tag{A.10}$$

The contribution of the last four terms, $\left(\frac{\Delta X}{X}\right)^2$, $\left(\frac{\Delta Z}{Z}\right)^2$, $\left(\frac{\Delta V_o}{V_o}\right)^2$, $\left(\frac{\Delta V_F}{V_F}\right)^2$, are small in comparison with the first two terms. The term $\frac{\Delta L}{L}$ could be as large as 6% (see Section 5.3). However, the assumption that the distance between the electrical terminals approaches the geometrical spacing between the inner holes of the cover plate is reasonable. As mentioned in Section 7.2, for pressures below 900 Kbars, the alumina elastic precursor was expected to partially reduce the voltage trace, thus showing that the error $\frac{\Delta L}{L}$ is reduced by fully filling the holes of the cover plate with indium. The noise picked up by the conductivity sample circuits precluded seeing the reduction of the voltage trace in all but a few cases. For all pressures, a similar filling of the holes as seen by the iron experiments (discussed in Section 5.3) is assumed. A nominal residual error of 2% is assumed. The question of the contact resistance between the voltage probes and the conductivity sample is not important because a four probe system was used.

The largest source of error in conductivity is due to the uncertainty in establishing the exact scope trace displacements.

The line thickness resolution, the demagnetization pulse and the high frequency noise ripple were three major contributors to the conductivity uncertainty which ranged from 3.2% to 12.6%. In cases where the noise ripple was substantial, signal averaging was made. This consequently gave larger errors. Only the records with the best resolution were used in determining the conductivity of each sample.

## APPENDIX B: FeSi PHASE DIAGRAM

The phase diagram of iron silicon alloys has been considered essentially complete by Hansen (1958). The review involved 65 references including nine since 1948. Subsequent reviews by Elliot (1965) and Shunk (1969), with references dataing from 1964, have not changed it significantly.

Recently, ten new experimental works were reviewed by Hultgren et al (1973) in addition to the older references. Important changes in the phase diagram have been made, especially in the order-disorder region of $X_{si} < 0.25$. Since we are interested in characterizing the initial states up to 21% by weight of Silicon, the latest version of the phase diagram is shown in Figure B.1 up to $X_{si} = 0.50$ because alloys prepared by freezing from a liquid will usually segregate. The resulting samples may be inhomogenious in composition and may contain one or more additional phases.

The liquidus and solidus curves start at 1890°K ($X_{si} = 0$) which is the melting point of Fe. As the concentration of Silicon increases, the liquidus and solidus curves drop in temperature and stay within 50°K of each other until they reach a peritectic

reaction at about 1548°K which spans from $X_{si} = 0.20$ to $X_{si} = 0.25$. Below the peritectic the two curves are within 15°K of each other up to $X_{si} = 0.30$ at which point a eutectic reaction takes place at

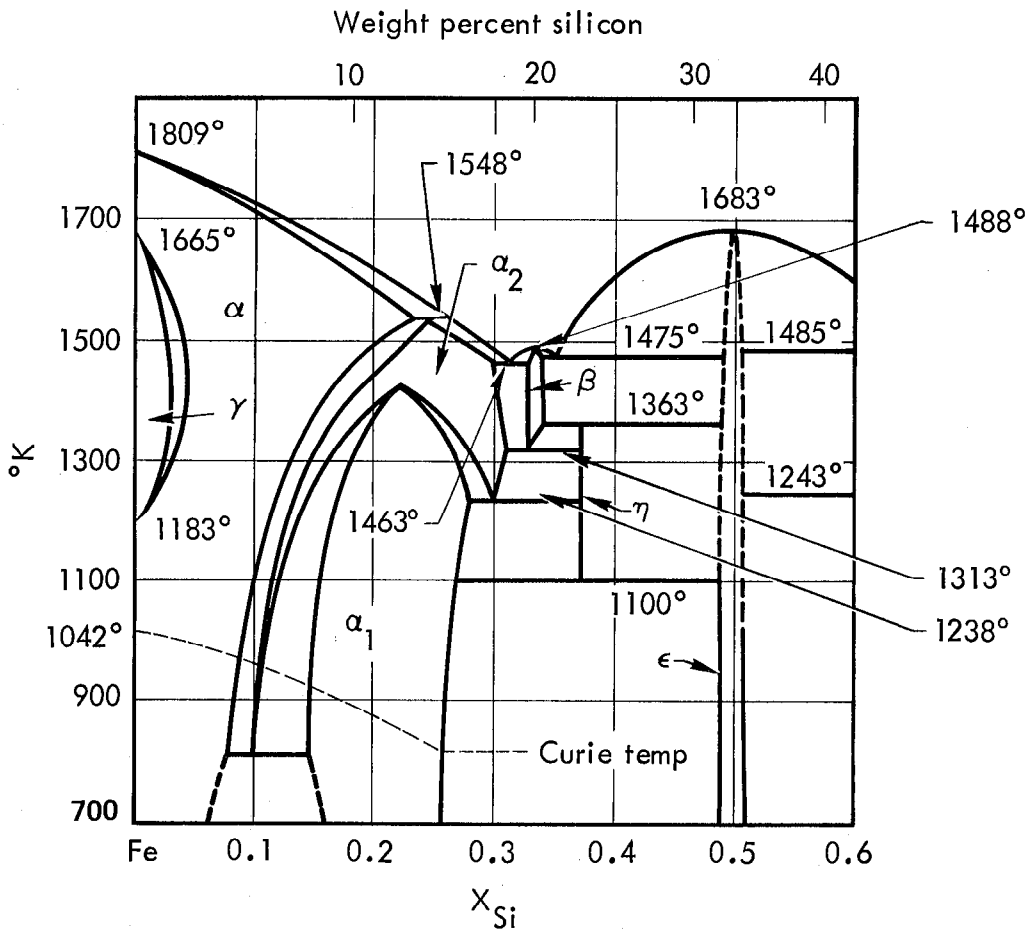


FIGURE B.1 PHASE DIAGRAM FOR $X_{si} \leq 0.5$

about 1463°K (1190°C) and extends up to $X_{si} \simeq 0.33$. The liquidus rises to 1488°K at $X_{si} = 0.333$, below which a very narrow high temperature solid phase field $\beta$ ($Fe_2Si$) exists down to 1313°K. Another eutectic occurs at 1475°K (1202°C) at $X_{si} \simeq 0.37$. Beyond this point the liquidus rises to 1683°K at $X_{si} = 0.50$, while the solidus remains horizontal at 1475°K.

Of the seven recognized solid phases between $X_{si} = 0$ and $X_{si} = 0.50$, three of them can be characterized as daltonides (stable over a very narrow range of compositions near a formula $Fe_xSi_y$ with x and y being small intergers. They are $\beta$ ($Fe_2Si$), $\eta$ ($Fe_5Si_3$), and $\epsilon$ (FeSi). Phase $\eta$ can be retained at room temperature by quenching. The other four are classified as berthollides which are stable over various ranges of composition. This property is typical of most intermetallic phases and may present difficulties in characterizing solid alloy samples. The $\gamma$ phase (which is analogous to the $\gamma$ - Fe phase) extends from 1183°K to 1665°K and from $X_{si} = 0$ to $X_{si} \simeq 0.025$ and the two phase region out to a maximum of $X_{si} \simeq 0.045$. Phase $\alpha$ is stable at room temperature from $X_{si} = 0$ to $X_{si} \simeq 0.06$ and, except for the $\gamma$ loop, extends up to the solidus curve and expands to $X_{si} = 0.20$ at 1548°K. $\alpha_2$ coexists on the left with the $\alpha$ phase down to 813°K at which point it undergoes an eutectoid decomposition. Below 1463°K, $\alpha_2$ extends to $X_{si} = 0.30+$ and has a two phase region with $\beta$ down to 1313°K. At 1313°K $\beta$ undergoes an eutectoid decomposition. Phase $\eta$ is a high temperature phase that exists between 1363°K and 1100°K and shares a two phase region with $\alpha_2$ between 1313°K and 1238°K. Phase $\alpha_1$ exists stably at room temperature between

$X_{si} \simeq 0.16$ and $X_{si} = 0.25$. It shares a two phase region with $\alpha$ below 813°K. Phase $\alpha_1$ coexists with $\epsilon$ up to 1100°K and $\eta$ between 1100°K and 1238°K. Phase $\alpha_1$ coexists with $\alpha_2$ at $X_{si} \simeq 0.10$ above 813°K, and also at $X_{si} \simeq 0.28$ at and above 1238°K. The two phase regions between $\alpha_1$ and $\alpha_2$ are narrow and disappear at $X_{si} \simeq 0.23$ and 1397°K above which $\alpha_1$ ceases to exist.

The crystalline structure of FeSi alloy phases at atmospheric pressure are summarized in Table B.1. Phase $\alpha$, $\alpha_1$ and $\alpha_2$ are ferromagnetic below the Curie temperatures shown in Figure B.1. In addition the (metastable) phase $\eta$ is ferromagnetic below 90°C (Hansen 1959). The phase diagram will be used to help evaluate the initial states of the FeSi alloys.

Extensive studies have recently been made of the $\alpha$, $\alpha_1$ and $\alpha_2$ phases (Warlimont, 1968; Inden, et al, 1972; Ettwig, et al, 1972; & Schlatte, et al, 1974). The order-disorder transitions have been shown to be of the second degree by specific heat, neutron diffractron, X-ray diffraction and electron microscope measurements. Differences of opinion still exist between the authors on the fine points of heterogeneous/homogeneous and long/short range order/disorder transformations. Fortunately, for our purposes of measuring bulk properties and electrical conductivity behind shock fronts, these differences of opinion do not affect the high pressure states.

An earlier misconception (Hansen, 1958; and Gupta, et al, 1964) that an alloy of composition $Fe_3Si$ ($X_{si} = 0.25$) exists as a separate phase still persists in more recent literature (Baum, et al, 1967;

TABLE B.1 CRYSTALLINE STRUCTURE OF FeSi PHASES FOR $X_{si} \leq 0.5$

| PHASE | STRUCTURE Å | ATOMS OF MOLECULES/ UNIT CELL | TYPE | ISOTYPIC WITH | REFERENCE |
|---|---|---|---|---|---|
| α FeSi | (Disordered) bcc<br>a = 2.866 to 2.8599 | 2 | A2 | W | Pearson, 1967 |
| γ FeSi | fcc<br>a = 3.6483 to 3.6538 | * | A1 | Cu | Pearson, 1967 |
| $\alpha_1$ FeSi | Ordered bcc<br>a = 2.8575 to 2.827 | 2 | $DO_3$ | $BiF_3$ | Pearson, 1967 |
| $\alpha_2$ FeSi | Ordered bcc<br>a = 5.6554 | 4 | B2 | $C_sCl$ | Meinhardt, et al, 1965 |
| β $Fe_2Si$ (High Temp) | bcc<br>a = * | 4 | A2 | W | Koster, et al, 1968 |
| η $Fe_5Si_3$ ( Metastable) | Ordered hcp<br>a = 6.7552<br>c = 4.7174 | 2 | $D8_8$ | $Mn_5Si_3$ | Pearson, 1967 |
| ε FeSi | Ordered Cubic<br>a = 4.500 ± .005 | * | B20 Prototype | * | Pearson, 1967 |

*Not reported

and Kalishevich, et al, 1969). It is not clear which of the two berthollides ( $\alpha_1$, or $\alpha_2$) is referred to as $Fe_3Si$.

## APPENDIX C: DEMAGNETIZATION PULSE

The theoretical derivation of the shape of the demagnetization pulse is given here. The assumptions are given explicitly. First, an infinite sheet of thickness $\ell$ is assumed. This is consistent with the conductivity sample dimensions $L \gg W \gg \ell$ as indicated in Section 4 where L is the length and W is the width.

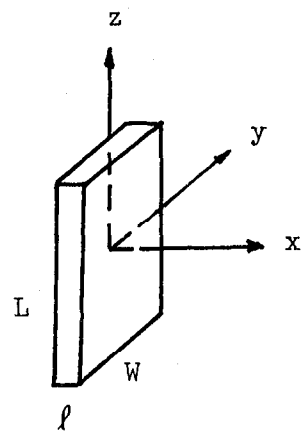


Second, the shock transit and phase transition times are assumed to be short (on the order of 10 ns) compared to the demagnetization time (measured on the order of 50 ns) consistent with Section 7. The whole sample is assumed to demagnetize at once in the first order approximation. This means that the magnetic permeability changes from a value on the order of $\mu_i \simeq 1000$ to $\mu_o = 1$ (the permeability of free space) at t = 0.

The initial magnetic field is due to a constant current $I_o$ through the sample. The initial magnetic field, B, inside the sample is given by

$$B\,(X', o) = 2\,B_o\,\left(\frac{X'}{\ell}\right) - B_o \qquad \text{at } t = 0$$

The magnetic field outside the sample is approximately $B \simeq 0$ because the boundary condition of the tangental component of the magnetic intensity H across the boundary is continuous. In other words using $H_t$ (inside) = $H_t$ (outside) leads to

$$\left.\frac{B\ \text{inside}}{\mu_i}\right|_t = \left.\frac{B\ \text{outside}}{\mu_o}\right|_t \Rightarrow \left.\underline{B\ \text{outside}}\right|_t \simeq 10^{-3}\ \left.\underline{B\ \text{inside}}\right|_t$$

The magnitude of the initial magnetic field looks like

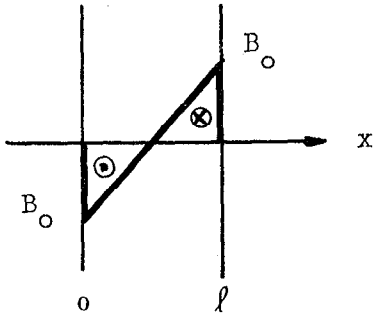


with the magnetic flux in the $\pm$ y direction due to a current $I_o$ in the z direction. For t greater than t = 0, the collapsing magnetic field sets up eddy currents which tend to keep the magnetic field up. The current distribution just after t = 0 looks like

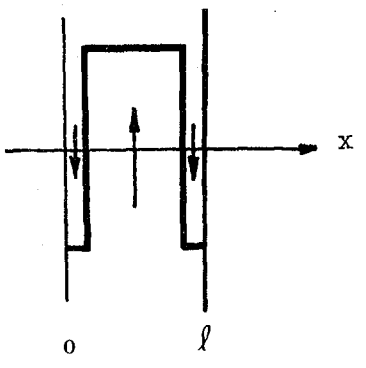

Maxwells' equation

$$\nabla^2 \vec{H} = \mu (\sigma \partial \vec{H}/\partial t + \epsilon \partial^2 \vec{H}/\partial t^2)$$

or

$$\nabla^2 \vec{B} = \mu (\sigma \partial \vec{B}/\partial t + \epsilon \partial^2 \vec{B}/\partial t^2)$$

is simplified because the second term in the parenthesis is negligible for a good conductor. The relaxation time of the medium is $t = \epsilon / \mu = 10^{-14}$ sec. The second term is due to the displacement current and is negligible for frequencies below the optical spectrum. We are left to solve a diffussion type equation. Similarly, we can drop the second term in another Maxwell's equation

$$\nabla \times \vec{H} = \sigma \vec{E} + \epsilon \partial \vec{E}/\partial t$$

The diffussion equation,

$$\nabla^2 \vec{B} = \mu \sigma \partial \vec{B}/\partial t = 1/\alpha (\partial \vec{B}/\partial t)$$

is solved by a separation of variables. The general soluation is of the form

$$B(x,t) = \sum_{a_x} e^{-\alpha a_x^2 t} \left( C'_x \operatorname{Cos}(a_x x) + C''_x \operatorname{Sin}(a_x x) \right)$$

The constants are evaluated by using the boundary conditions. Using $B(o,t) = 0$ leads to $C'_x = 0$. Using $B(\ell,t) = 0$ leads to $a_x = \frac{n\pi}{\ell}$ for $n = 1,3,5 \ldots$. We now have

$$B(x,t) = \sum_{n=1}^{\infty} C_n e^{-\frac{\alpha n^2 \pi^2 t}{\ell^2}} \operatorname{Sin}(n\pi x/\ell) \qquad \text{for } t > 0$$

where $C_n = C_x''$ .

In order to evaluate $C_n$, the magnetic field is expanded in a Fourier series at $t = 0$,

$$B(x,o) = \sum_{n=1}^{\infty} C_n \operatorname{Sin}(n\pi x/\ell)$$

The coefficients $C_n$ are given by

$$C_n = (2/\ell) \int_o^{\ell} B(x',o) \operatorname{Sin}(n\pi x'/\ell) dx'$$

$$C_n = (2B_o/\ell) \int_o^{\ell} (2x'/\ell - 1) \operatorname{Sin}(n\pi x'/\ell) dx'$$

The two integrals are of the form:

$$\int_o^{\ell} x \operatorname{Sin}(ax) dx = -(\ell/a) \operatorname{Cos}(a\ell)$$

and

$$\int_o^{\ell} \operatorname{Sin}(ax) dx = - 1/a (\operatorname{Cos}(a\ell) - 1)$$

where $\operatorname{Cos}(a\ell) = \operatorname{Cos}(n\pi\ell/\ell) = (-1)^n$

Therefore, the coefficients $C_n$ are given by

$$C_n = -2B_o/n\pi(1 + (-1)^n)$$

The magnetic field (inside the conductor) is given, for $t > 0$, by

$$B(x,t) = -\sum_{n=1}^{\infty} \frac{2B_o}{n\pi}(1 + (-1)^n)\,\mathrm{Sin}(n\pi x/\ell)\, e^{-\frac{\alpha n^2 \pi^2 t}{\ell^2}}$$

The field is only in the $\pm$ y direction (the field lines close at $y = \pm\infty$) and only the even terms in n contribute.

To find the potential drop across the voltage probes due to the demagnetization, we have to find the electric field at the surface of the sample. Expanding $\nabla \times \vec{H}$, (and using $\vec{B} = \mu\vec{H}$) gives

$$\frac{1}{\mu}\nabla \times \vec{B} = \begin{vmatrix} \hat{i} & \hat{j} & \hat{k} \\ \frac{\partial}{\partial x} & \frac{\partial}{\partial y} & \frac{\partial}{\partial z} \\ o & B_y & o \end{vmatrix} = \frac{\hat{k}}{\mu}\frac{\partial B_y(x,t)}{\partial x}$$

This gives the electric field E a component only in the z direction. Solving for E (x,t) gives

$$E(x,t) = 1/\mu\sigma \frac{\partial B(x,t)}{\partial x}$$

The potential difference $\mathcal{E}$ between the voltage probes a distance L' apart is

$$\mathcal{E} = L'\, E(\ell,t)$$

$$\mathcal{E} = -\frac{2B_o L'}{\mu\sigma\ell}\sum_{n=1}^{\infty}(1 + (-1)^n)(-1)^n\, e^{-\frac{\alpha n^2 \pi^2 t}{\ell^2}}$$

Converting the parameters to a more convenient form, using Amperes Law, gives

$$\oint_{\text{loop}} H \, d\ell = I_o = 2\xi H(\ell,o) = 2\xi B_o/\mu_i$$

or

$$B_o = \mu_i I_o/2\xi \qquad \text{for } t < 0$$

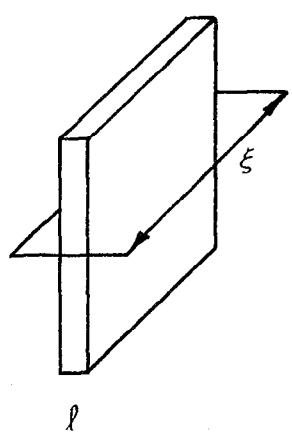


LOOP

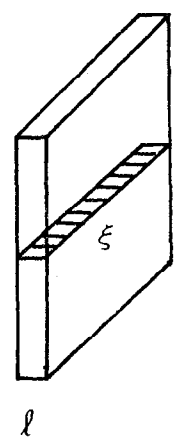


CROSS SECTIONAL AREA = $\ell\xi$

The resistance between the probes is $R_o = L'/\ell_0\xi\sigma_0$ before the shock and $R_1 = L'/\ell_1\xi\sigma_1$ after the shock, with $\ell_1 = \ell_o V_F/V_o$ . Simplifying terms:

$$\frac{2 B_o L'}{\mu_0 \sigma_1 \ell_1} = \frac{2\mu_i I_o L'}{\mu_0 \sigma_1 \ell_1 2\xi} = \frac{\mu_i I_o R_1}{\mu_0} \qquad \text{for } t > 0 .$$

The potential across the leads, before and after the shock, is

$$V_o = I_o R_o$$

$$V_1 = I_o R_1 + \mathcal{E}$$

Taking the ratio gives

$$\frac{V_1}{V_o} = \frac{R_1}{R_o}\left\{1 - \frac{\mu_i}{\mu_o}\sum_{n=1}^{\infty}(1 + (-1)^n)(-1)^n e^{-\frac{n^2\pi^2 t}{\mu_o \sigma_1 \ell^2}}\right\}$$

The first order solution at t = 0 diverges as

$$\sum_{n=1}^{N}(1 + (-1)^n) = N \qquad \text{as} \quad N \rightarrow \infty$$

For t > 0, the solution is

$$\frac{V_1}{V_o} = \frac{R_1}{R_o}\left\{1 - \frac{2\mu_i}{\mu_o}\left[e^{-\frac{t}{\tau}} + e^{-\frac{4t}{\tau}} + e^{-\frac{9t}{\tau}} + \ldots\right]\right\}$$

where

$$\tau = \frac{\ell^2 \mu_o \sigma_1}{4\pi^2}$$

As time increases, the demagnetization pulse shape is governed by the first exponential term.

A second order solution for the $\mu_i$ to $\mu_o$ transition (assumed to be non-instantaneous) eliminates the divergence at t = 0. Assume the transition is linear in time,

$$\mu_1(t) = \mu_i + (\mu_o - \mu_i)\, t/T \qquad \text{for } 0 < t < T$$

where T is the phase transition time of the sample. By separation of variables, the time dependent solution changes to

$$- a^2 \alpha \Upsilon(t) = d\Upsilon(t)/dt \qquad \text{where} \quad a = n\pi/\rho$$

Integrating over an interval $t > T$, gives

$$\int_0^t \frac{d\Upsilon(t)}{\Upsilon(t)} = - a^2 \int_0^t \alpha \, dt = - a^2 \left[ \int_0^T \alpha(t) dt + \alpha \int_T^t dt \right]$$

where $\alpha$ is independent of t for $t \geq T$ (and $\mu(t) = \mu_o$ for $t \geq T$). Performing the integrations gives

$$\int_0^T \alpha(t) dt = - 1/\sigma_1 ( T/(\mu_o - \mu_i)) \log ( \mu_i/\mu_o )$$

and

$$\alpha \int_T^t dt = ( t - T )/\sigma_1 \mu_o$$

The time depend solution for $t > T$ gives

$$\int_0^t \frac{d\Upsilon(t)}{\Upsilon(t)} = \log \Upsilon(t) = - a^2 \left[ \frac{T}{\sigma_1(\mu_o - \mu_i)} \log\left(\frac{\mu_i}{\mu_o}\right) + \frac{t - T}{\sigma_1 \mu_o} \right]$$

or

$$\Upsilon(t) = \left(\frac{\mu_o}{\mu_i}\right)^{- \frac{a^2 T}{\sigma_1(\mu_o - \mu_i)}} e^{- \frac{a^2 (t - T)}{\sigma_1 \mu_o}}$$

where $\tau = \dfrac{\ell^2 \mu_0 \sigma_1}{4 \pi^2}$

This is the solution used in Section 7.

Demagnetization pulse

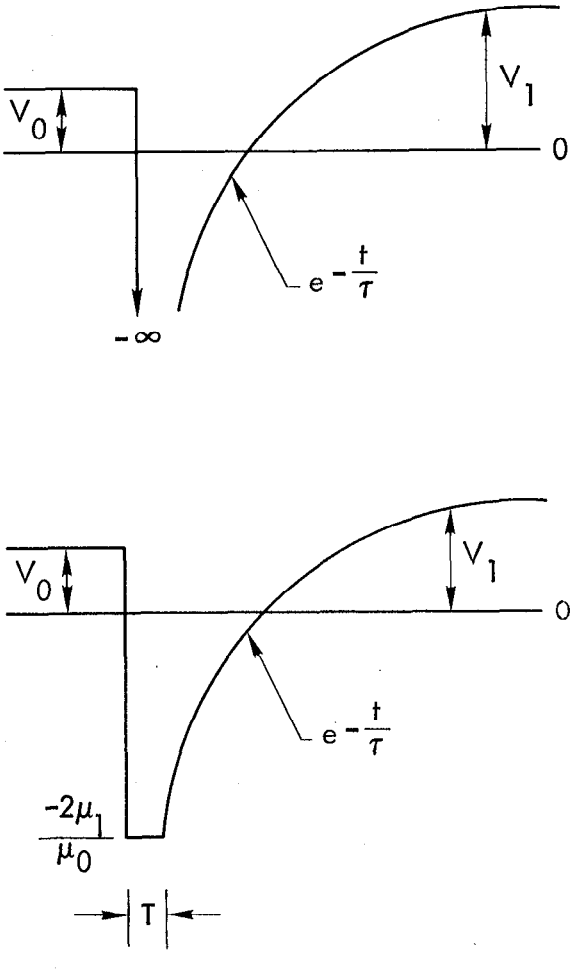


FIGURE C.1 FIRST AND SECOND ORDER

SOLUTIONS FOR THE DEMAGNETIZATION PULSE

## REFERENCES


Adams, R. D., Bull, Seism. Soc. Am. 62, 1063 (1972).

Ahrens, T. J., W. H. Gust, E. B. Royce, J. Applied Phys. 39, 4610 (1968).

Alberts, H. L., P. T. Wedepohl, Physics 53, 571 (1971).

Alder, B. J., J. Geophys. Res. 71, 4973 (1966).

Al'tshuler, L. V., K. K. Krupnikov, B. N. Ledenev, V. I. Zhuchikhin, M. I. Brazhnik, Soviet Phys. JETP 34, 606 (1958).

Al'tshuler, L. V., S. B. Kormer, A. A. Bakanova, R. F. Tunin, Zh. Exp. i Teoret. Fiz 38, 791 (1960).

Al'tshuler, L. V., Soviet Phys. Ups. 8, 52 (1965).

Al'tshuler, L. V., Phys. Earth Planet. Interiors 5, 295 (1972).

American Institute of Physics Handbook, 3rd Ed., D. E. Gray, ed. McGraw-Hill Book Co., N.Y. (1972).

Arajs, S., R. V. Colvin, Phys. Stat. Sol. 6, 797 (1964).

Balchan, A. S., C. R. Cowan, J. Geophys. Res. 71, 3577 (1966).

Balchan, A. S., H. G. Drickamer, Rev. Sci. Instrum. 32, 308 (1961).

Baum, B. A., P. V. Gel'd, G. V. Tyagunov, Fix. Metal. Metalloved. 24, 181 (1967).

Birch, F., J. Geophys. Res. 69, 4377 (1964).

Birch, F., Geophys. J. R. Ast. Soc. 29, 373 (1972).

Bolt, B. A., Phys. Earth Planet. Interiors 5, 301 (1972).

Bolt, B. A., Scientific American 228, No. 3, 24 (1973).

Bridgeman, P. W., Proc. Am. Acad. Arts. Sci. 81, 165 (1952).

Bridgeman, P. W., Collected Experimental Papers, Vol. 7, Harvard V. Press, Cambridge, Mass (1964).

Buchbinder, G. G., Phys. Earth Planet. Interiors 5, 123 (1972).

Buchbinder, G. G., Earth Planetary Sci. Letters 14, 161 (1972).

Buchbinder, G. G., G. Poupinet, Bull. Seism. Soc. Am. 63, 2047 (1973).

Bullard, E. C., Phil. Trans. Roy. Soc. A263, 481 (1968).

Bullard, E. C., Nature of the Solid Earth, Chapter 10,E. C. Robertson, ed., McGraw Hill, N.Y. (1972).

Bullen, K. E., An Introduction to the Theory of Seismology, Cambridge U. Press, Cambridge (1963).

Bullen, K. E., R. A. W. Haddon, Phys. Earth Planet, Interiors 1, 1 (1967).

Bullen, K. E., Applied Mathematics 60, 752 (1968).

Bullen, K. E., Phys. Earth Planet. Interiors 3, 36 (1970).

Bullen, K. E., Phys. Earth Planet. Interiors 6, 131 (1972).

Bullen, K. E., R. A. W. Haddon, Geophys. J. R. Astr. Soc. 34, 31 (1973).

Bundy, F. P., J. Appl. Phys. 36, 616 (1965).

Chart, T. G., High Temperatures-High Pressures 2, 461 (1970).

Clark, S. P., Structure of the Earth, Chapter 8, Prentice Hall, Inc., N.J. (1971).

Clendenen, R. L., H. G. Drickamer, J. Chm. Phys. 44, 4385 (1966).

Colman, P. J., Phys. Earth Planet. Interiors 6, 170 (1072).

Cook, A. H., Space Sci. Rev. 2, 355 (1963).

Cook, A. H., Physics of the Earth and Planets, John Wiley and Sons, N.Y. (1973).

Courant, R., K. D. Friedricks, Supersonic Flow and Shock Waves, p. 121, New York (1947).

Dreirach, O.,R. Evans, H. J. Gunterhod, H. U. Kunzi, J. Phys. F: Metal. Phys. 2, 709 (1972).

Duff, R. E., F. S. Minshall, Phys. Rev. 108, 1207 (1957).

Dugdale, J. S., D. MacDonald, Phys. Rev. 89, 832 (1953).

Dziewonski, A. M., F. Gilbert, Geophys. J. R. Astr. Soc. 27, 393 (1972).

Elliott, R. P., Constitution of Binary Alloys, First Supplement, McGraw Hill, N.Y. (1965).

Ettwig, H. H., W. Pepperhoff, Z. Metallkde 63, 453 (1972).

Evans, R., A. Jain, Phys. Earth Planet. Interiors 6, 141 (1972).

Frazer, M. C., Geophys. J. R. Astr. Soc. 34, 193 (1973).

Fuller, P. J., J. H. Price, Nature 193, 262 (1962).

Gardiner, R. B., F. D. Stacey, Phys. Earth Planet. Interiors 4, 406 (1971).

Gilbert, J. T., G. E. Backus, Bull. Seismol. Soc. Am. 58, 103 (1968).

Gilbert, F., Mathematical Problems in Geophysical Sciences, Vol 14, P. 107, W. H. Reid ed, American Mathematical Society, Providence, R.I. (1971).

Giles, P. M., M. H. Longenbach, International Metallographic Society Proceedings, P. 111, I.M.S. Inc. Los Alamos, N.M. (1969).

Graham, R. A., J. Appl. Phys. 39, 437 (1968).

Grover, R., R. N. Keeler, F. J. Rogers, G. C. Kennedy, J. Phys. Chem. Solids 30, 2091 (1969).

Grover, R., J. Phys. Chem Solids 31, 2347 (1970).

Grover, R., J. of Chem. Phys. 55, 3435 (1971).

Grover, R., Private Communication (1976).

Gupta, K. P., C. H. Cheng, P. A. Beck, J. Phys. Chem. Solids 25, 1147 (1964).

Gust, W. H., "High Explosive Shock Wave Generating Systems," Lawrence Livermore Laboratory, unpublished (1966).

Hales, A. L., J. L. Roberts, Bull. Seism. Soc. Am. 60, 1427 (1970).

Hales, A. J., J. L. Roberts, Bull. Seism. Soc. Am. 61, 1051 (1971).

Hansen, M., K. Anderko, Constitution of Binary Alloys, p. 711, McGraw Hill, N.Y. (1958).

Herrin, E., Bull. Seism. Soc. Am. 58, 1193 (1968).

Hide, R., Nature 222, 1055 (1969).

Higgins, G., G. C. Kennedy, J. Geophys. Res. 76, 1870 (1971).

Huang, Y. K., J. of Chem. Phys. 45, 1979 (1966).

Hultgren, R. P., D. Desai, D. T. Hawkins, M. Gleiser, K. K. Kelley, Selected Values of the Thermodynamic Properties of Binary Alloys, P. 871, John Wiley and Sons, N.Y. (1973).

Ibrahim, A. K., Phys. Earth Planet. Interiors 7, 187 (1973).

Inden, G., W. Pitsch, Z. Metallkde 63, 253 (1972).

Jackson, J. D. Classical Electrodynamics, p. 313, John Wiley and Sons, N.Y. (1965).

Jain, A., R. Evans, Nature 235, 165 (1972).

Jamieson, J. C., A. W. Lawson, J. Appl. Phys. 33, 766 (1962).

Johnson, Q., A. Mitchell, R. N. Keeler, L. Evans, Phys. Rev. Letters 25, 1099 (1970).

Johnston, M. J. S., R. G. J. Stearns, Phys. Earth Planet. Interiors 7, 217 (1973).

Joss, G., Theoretical Physics, 3rd ed. Hofner, N.Y. (1958).

Kalishevich, G. I., G. A. Matveev, L. P. Andreeva, K. P. Rodinov, P. V. Gel'd, Russ. J. of Phys. Chem. 43, 1459 (1969).

Keeler, R. N., Behavior of Dense Media Under High Dynamic Pressures, P. 397, Gordon and Breach, N.Y. (1968).

Keeler, R. N., A. C. Mitchell, Solid State Comm. 7, 271 (1969).

Keeler, R. N., E. B. Royce, "Six Lectures on Shock-Wave Physics," Lawrence Livermore Laboratory Report, UCRL-71846 (1970).

Keeler, R. N., E. B. Royce, Proc. 48th International School of Phys. Enrico Fermi," Varenna, Italy, Academic Press, N.Y. (1971).

Kittel, C., Introduction to Solid State Physics, 3rd Ed., p 222, John Wiley and Sons, N.Y. (1966).

Knopoff, L., G. J. F. MacDonald, Geophys. J. 3, 68 (1960).

Kormer, S. B., A. J. Funtikov, Izv. Earth Phys. Ser. 5, 1 (1965).

Koster, W., T. Godecke, Z. Metallkde 59, 602 (1968).

Kraut, E. A., G. C. Kennedy, Phys. Rev. 151, 668 (1966).

Lai, D. Y. R., R. J. Borg, "Diffusion of Silicon in α-Fe and α-FeSi Alloys" Lawrence Livermore Laboratory Report, UCRL-50517 (1968).

Lai, D. Y. F., R. J. Borg, "Diffusion of Iron in α-FeSi Alloys" Lawrence Livermore Laboratory Report, UCRL-50516 (1968).

Leppaluoto, D. A., Phys. Earth Planet. Interiors 6, 175 (1972).

Lewis, J. S., Earth Planet. Sci. Letters 11, 130 (1971).

Liu, L., W. A. Basset, J. of Geophys. Res. 80, 3777 (1975).

Malkus, W. V. R. Science 160, 259 (1968).

Malkus, W. V. R., Mathematical Problems in the Geophysical Sciences, Vol. 14, p. 207, W. H. Reid, ed. American Mathematical Society, Providence, R.I. (1971).

McLachlan, D., Jr., E. G. Ehlers, J. Geophs. Res. 76, 2780 (1971).

McQueen, R. G. Metalurgy at High Pressures and High Temperatures, Vol. 22, Chap 3, K. A. Gschneider, Jr., M. T. Hepworth and N. A. D. Parlee, eds, Metalurgical Society Conferences, N.Y. (1964).

McQueen, R. G., J. N. Fritz, S. P. Marsh, J. Geophys. Res. 69, 2947 (1964).

McQueen, R. G., S. P. Marsh, J. Geophys. Res 71, 1751 (1966).

McQueen, R. G., S. P. Marsh, "GMX-6 Hugoniot Data Summary" Los Alamos Scientific Laboratory, unpublished (1969).

Meinhardt, D., O. Krisement, Arch. Eisenhuttenw. 36, 293 (1965).

Millet, L. E., D. L. Decker, Phys. Letters 29A, 7 (1969).

Minshall, F., S., J. Appl. Phys. 26, 463 (1955).

Mitchell, A. C., R. N. Keeler, Bull. Am. Phys. Soc. 12, 1128 (1967).

Mitchell, A. C., R. N. Keeler, Rev. Sci. Instr. 39, 513 (1968).

Mitchell, A. C., G. Matassov, "High Pressure Electrical Conductivity of Shocked Silicon" Lawrence Livermore Laboratory, internal memorandum, unpublished (1970).

Mitchell, A. C., Private Communication (1975).

Murthy, V. R., H. T. Hall, Phys. Earth Planet, Inter. 2, 276 (1970).

Murthy, V. R., H. T. Hall, Phys. Earth Planet. Inter. 6, 123 (1972).

Ness, N. F., K. W. Behannon, R. P. Lepping, Y. C. Whang, K. H. Schlatten, Science 185, 151 (1974).

Ness, N. F., K. W. Behannon, R. P. Leeping, Y. C. Whang, Nature 255, 204 (1975).

Pearson, W. B., A Handbook of Lattice Spacings and Structure of Metals and Alloys, Vol. 4, p. 936, Pergamon Press Inc., N.Y. (1967).

Pipkorn, D. N., C. K. Edge, P. Debrunner, G. DePasqualli, H. G. Drickamer, H. Frauenfelder, Phys. Rev. 135, A1604 (1964).

Press, F., Phys. Earth Planet, Interiors 3, 3, (1970).

Press, F., Nature of the Solid Earth, Chap 7, E. C. Robertson ed., McGraw Hill, N.Y. (1972).

Reynolds, C. L. Jr., K. A. Faughnan, R. E. Barker, Jr., J. Chem. Phys. 59, 2943 (1973).

Rice, M. I., R. G. McQueen, J. M. Walsh, Solid State Physics, Vol. 6, p. 1, F. Seitz and D. Turnbull eds. Academic Press, N.Y. (1958).

Rice, M. I., Phys. Rev. 2, B4800 (1970).

Ringwoord, A. E., Geochim. Cosmochim. Acta 30, 41 (1966).

Roberts, P. H., Mathematical Problems in Geophysical Sciences, Vol. 14, p. 129, W. H. Reid ed, American Mathematics Society, Providence, R.I. (1971).

Roberts, P. H., A. M. Soward, Annu. Rev. Fluid Mech. 4, 117 (1972).

Royce, E. B., "Shock Induced Demagnetization of Nickel Ferrite, YIG and Iron," Lawrence Livermore Laboratory Report, UCRL-70240 (1967).

Royce, E. B., Proc. IUTAM Symposium on Behavior of Dense Media Under High Dynamic Pressures, p. 419, N.Y. (1968).

Royce, E. B., "GRAY, a Three-Phase Equation of State for Metals," Lawrence Livermore Laboratory Report, UCRL-51121 (1971).

Runcorn, S. K., Phys. Earth Planet. Interiors 6, 100 (1972).

Schlatte, G., G. Inden, W. Pitsch, Z. Metallkde 65, 94 (1974).

Shunk, F. A., Constitution of Binary Alloys, 2nd Suppl., p. 347, McGraw Hill, N.Y. (1969).

Stacey, F. D., Earth Planet. Sci. Letters 3, 204 (1967).

Stacey, F. D. Geophysical Surveys 1, 99 (1972).

Strong, H. M., R. E. Tuft, R. E. Hanneman, Metalurgical Transactions 4, 2657 (1973).

Takahaski, T., W. A. Bassett, Science 145, 483 (1964).

Tanner, L., S. A. Kulin, Acta Met 9, 1038 (1961).

Tolland, H. G., Phys. Earth Planet Interiors 8, 282 (1974).

Tozer, D. C., Earth's Mantle, Academic Press, London (1967).

Tozer, D. C., Phys. Earth Planet. Interiors 6, 182 (1972).

Truell, R., C. Elbaum, B. B. Chick, Ultrasonic Methods in Solid State Physics, Academic Press, N.Y. (1969).

Vaidya, S. N., G. C. Kennedy, J. Phys. Chem. Solids 31, 2329 (1970).

Van Thiel, M., B. J. Alder, J. Chem. Phys. 44, 1056 (1966).

Van Thiel, M., A. Kusubov, A. C. Mitchell, "Compendium of Shock Wave Data," Vol. 1, Lawrence Livermore Laboratory Report, UCRL-50108 (1967), and updated version, in printing (1976).

Verhoogen, J., Geophys. J. R. Astr. Soc. 4, 276 (1961).

Verhoogen, J., Phys. Earth Planet. Interiors 7, 47 (1973).

Walsh, J. M., R. M. Christian, Phys. Rev. 97, 1545 (1955).

Wang, C. Y., Geophys. J. R. Astro. Soc. 27, 29 (1972).

Warlimont, H., Z. Metallkde 59, 595 (1968).

Wong, J. Y., R. K. Linde, P. S. DeCarli, Nature 219, 713 (1968).

Young, D. A., "Phase Diagrams of the Elements," Lawrence Livermore Laboratory Report, UCRL-51902 (1975).

Zinov'ev, V. E., Sh. Abel'skii, Sh. Sandakova, L. N. Petrova, P. V. Gel'd, Soviet Phys. JETP 36, 6,1174 (1973).

Zukas, E. G., C. M. Fowler, F. S. Minshall, J. O'Rourke, Trans. Metallurical Society of AIME 227, 746 (1963).

*Technical Information Department*
LAWRENCE LIVERMORE LABORATORY
University of California | Livermore, California · 94550

176 480

VAULT REFERENCE COPY

RECEIVED
LAWRENCE LIVERMORE LABORATORY

SEP 06, 1977

TECHNICAL INFORMATION DEPARTMENT